Quarton qubits with stacked Josephson junctions

Zur Erlangung des akademischen Grades eines

Doktors der Naturwissenschaften (Dr. rer. nat.)

von der KIT-Fakultät für Physik des

Karlsruher Instituts für Technologie (KIT)

genehmigte

Dissertation

von

M.Sc. Alex S. Kreuzer

Tag der mündlichen Prüfung:	06.02.2026
Referent:	Prof. Dr. Alexey V. Ustinov
Korreferent:	Prof. Dr. Alexander Shnirman

Contents

1 Introduction

Compact, low-loss inductive elements with high characteristic impedance are central building blocks of superconducting quantum circuits. Their inductive energy sets the scales governing coherence and device performance in qubits [1–4], high-impedance resonators [5–11], and tunable couplers [12–14]. A large inductive impedance—ideally exceeding the vacuum impedance $Z_0 = \sqrt{\mu_0/\epsilon_0} \approx 377\,\Omega$—enhances anharmonicity, strengthens capacitive interactions in circuit QED, and suppresses current fluctuations [2, 5, 15]. In flux-type qubits and couplers, it also sets the sensitivity to flux-noise and the magnitude of persistent currents, directly influencing dephasing and relaxation [3, 16, 17].

A variety of technological platforms have been developed to realize large inductances in a compact footprint. Prominent examples include disordered superconductors with enhanced kinetic inductance, such as NbN, TiN, and granular aluminum [7, 18–24], nanowire-based geometric superinductors [15, 25], or chains of Josephson junctions [2, 5]. While each approach has enabled important advances, they face intrinsic limitations: disordered films suffer from dielectric loss associated, e.g., with surface oxides or magnetic spins [7, 19, 24, 26]; geometric superinductors are compact but exhibit fabrication variability and elevated loss tangents [25]; and planar Josephson junction arrays require large on-chip footprints and host extensive metal–substrate and metal–vacuum interfaces containing two-level systems (TLS) that limit coherence [27, 28]. Their large island areas cause parasitic stray capacitances that lower the impedance, introduce plasmonic modes within the operational frequency band, thereby constraining the inductance [5, 29].

These considerations motivate the study of vertically *stacked* Josephson junction arrays. In this work, we develop and characterize $\mathrm{Al/AlO}_x\mathrm{/Al}$ junction stacks as high-impedance inductors and employ them in superconducting quantum circuits. By incorporating many junctions into a compact stack, the footprint of the array is strongly reduced while parasitic capacitances to ground are simultaneously suppressed. Adjacent stacks are connected via suspended superconducting bridges, ensuring that no additional dielectric material is introduced near the inductor (see Fig. 1.1). The geometry of a stack leverages near-unity electrode utilization: almost the entire metallic surface forms tunnel junctions, while only narrow sidewalls

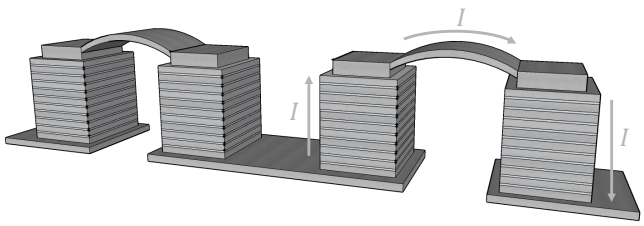

Figure 1.1: Schematics of an array of stacked junctions. Pairs of stacks are connected with suspended superconducting bridges on top of two stacks and by wiring at the bottom. The stacks and the arches are not to scale.

remain exposed to lossy environmental interfaces. This reduction in interface participation can significantly reduce TLS-induced dissipation [6, 7, 19, 30, 31], a key limitation for coherence in superconducting circuits. Moreover, the smaller amount of exposed electrode surface leads to substantially lower parasitic stray capacitances, thereby enabling higher impedance and pushing spurious array modes to higher frequencies [32, 33].

In the first part of this work, we model and simulate the parasitic stray capacitances in stacks and calculate their oscillation modes. We measure current–voltage curves of fabricated junction stacks and use these measurements to develop a multilayer fabrication method that enables compact stacks with uniform junction characteristics.

In the second part of this work, we integrate stacked junction arrays into superconducting flux qubits to evaluate their performance in a realistic quantum-circuit environment. Among flux-type qubits, devices operating in the *quarton* regime have recently emerged as a compelling architecture [4, 34–37]. In this regime, the inductive energy of the array is approximately equal to the Josephson energy of the small-junction, resulting in a shallow, nearly quartic potential around the minimum. The quarton regime intrinsically suppresses first-order sensitivity to low-frequency flux noise around the flux sweet spot—typically the dominant dephasing mechanism in flux-type qubits [38–40]—while simultaneously maintaining a large, positive anharmonicity of roughly one third of the transition frequency [4, 34, 41]. This combination enables fast and selective microwave control without sacrificing robustness to low-frequency fluctuations [14, 34, 36].

We design and fabricate quarton qubits with stacked junction inductors, study their spectra and time-domain properties, including how the coherence depends on the geometry of the stacked junction arrays. To disentangle material-intrinsic decoherence mechanisms from dephasing induced by external flux noise, we employ a persistent-current bias scheme that provides a low-noise and stable flux bias

for quarton qubits. This approach allows us to study flux-noise-related coherence limits under well-controlled bias conditions. We benchmark the trapping mechanism and characterize the long-term stability of the persistent current. Finally, we investigate the coherence properties of a quarton qubit flux biased with a persistent current.

In a complementary spectroscopy study of quarton devices with different stacked-junction array sizes, we identify two-level systems in the tunnel barriers as the dominant intrinsic decoherence mechanism. A systematic TLS-spectroscopy study further links the density and coupling strength of these defects to the geometry of the junction stacks.

The remainder of this thesis is organized as follows. *Chapter 2* reviews the fundamentals of superconductivity and Josephson junctions. *Chapter 3* introduces flux-type qubits—particularly in the quarton regime—and the relevant noise mechanisms. *Chapter 4* summarizes the cryogenic setup and measurement instrumentation. *Chapter 5* presents stacked Josephson junction arrays, their design, fabrication, and electrical characterization. *Chapter 6* investigates quarton qubits using stacked junctions, focusing on the qubit spectra and coherence properties. It includes separate sections on decoherence induced by external flux noise and on decoherence associated with TLS in the junction barriers.

2 Superconductivity and the Josephson Junction

This chapter introduces the theoretical foundations of superconducting circuits, summarizing the key principles of superconductivity and the Josephson effect.

2.1 Introduction to Superconductivity

Superconductivity represents one of the most remarkable manifestations of quantum mechanics on a macroscopic scale. Below a characteristic critical temperature T_c, certain materials exhibit zero DC resistance and expel magnetic fields from their interior, a phenomenon known as the Meissner–Ochsenfeld effect [42]. These properties arise from the formation of a collective condensate of paired electrons—Cooper pairs—which occupy a single macroscopic quantum state. The description of this state and its electromagnetic properties can be approached on several theoretical levels, ranging from the phenomenological London and Ginzburg–Landau (GL) theories to the microscopic Bardeen–Cooper–Schrieffer (BCS) model. This section summarizes the key equations and concepts that are required for understanding Josephson junctions and their role in superconducting quantum circuits.

2.1.1 The London equations

Following the discovery of superconductivity by Kamerlingh Onnes in 1911 [43], a central challenge was to explain its perfect conductivity and perfect diamagnetism. The first quantitative description was given in 1935 by the London brothers [44]. The temporal evolution of the supercurrent density $\vec{j_s}$ in an electric field $\vec{E}$ follows from the equation of motion

$$\frac{\partial \vec{j_s}}{\partial t} = \frac{n_s q^2}{m^*} \vec{E}, \tag{2.1}$$

where n_s denotes the density of superconducting charge carriers (Cooper pairs) with charge $q = 2e$ and effective mass m^*. Equation (2.1) implies an acceleration of the superconducting charge carriers in response to an applied field, resulting in a current that persists indefinitely once the field is removed.

Combining Eq. (2.1) with Maxwell's equations and considering steady-state conditions leads to the second London equation,

$$\nabla \times \vec{j_s} = -\frac{n_s q^2}{m^*} \vec{B}, \tag{2.2}$$

where $\vec{B}$ is the magnetic flux density inside the superconductor. Taking the curl of both sides and applying $\nabla \cdot \vec{B} = 0$ gives

$$\nabla^2 \vec{B} = \frac{\vec{B}}{\lambda_L^2}, \tag{2.3}$$

which predicts that magnetic fields decay exponentially within the superconductor:

$$B(z) = B_0 e^{-z/\lambda_L}. \tag{2.4}$$

The characteristic decay length λ_L is the *London penetration depth*,

$$\lambda_L = \sqrt{\frac{m^*}{\mu_0 n_s q^2}}, \tag{2.5}$$

typically about 50 nm for aluminum [45, 46]. This exponential screening of magnetic fields provides a phenomenological description of the Meissner effect and distinguishes a superconductor from a perfect conductor, which would merely trap magnetic flux.

Experiments further revealed that the penetration depth is not constant but exhibits a characteristic temperature dependence. Empirically, this behavior can be described by

$$\lambda(T) \approx \lambda(0) \left[1 - \left(\frac{T}{T_c}\right)^4\right]^{-1/2}, \tag{2.6}$$

which lies beyond the scope of the purely phenomenological London equations [47]. In addition, the observation of an isotope effect, $T_c \propto M^{-1/2}$ with the atomic mass M, demonstrated that lattice vibrations play a central role in the superconducting pairing mechanism [47]. This finding provided a key experimental motivation for the microscopic Bardeen–Cooper–Schrieffer (BCS) theory of superconductivity.

While the BCS theory captures the microscopic origin of superconductivity, many electromagnetic properties of superconductors can be described by effective macroscopic theories. In particular, the Ginzburg–Landau framework provides a phenomenological description in terms of a complex order parameter and is especially useful near the critical temperature. It is therefore introduced in the following section as a bridge between microscopic theory and circuit-level modeling.

2.1.2 Ginzburg–Landau theory

In 1950, Ginzburg and Landau (GL) formulated a phenomenological theory of superconductivity based on the concept of a macroscopic order parameter [48]. The superconducting state is described by a complex wave function

$$\Psi(\vec{r}) = \sqrt{n_\mathrm{s}(\vec{r})}\, e^{i\phi(\vec{r})}, \tag{2.7}$$

whose squared modulus corresponds to the local density of superconducting carriers $n_\mathrm{s}(\vec{r})$ and whose phase $\phi(\vec{r})$ defines the long-range coherence of the condensate (later identified microscopically as Cooper pairs in the BCS theory).

The total free energy density f_s quantifies the energy of the superconducting condensate including spatial variations and electromagnetic coupling. It can be written as [47]

$$f_\mathrm{s} = f_\mathrm{n} + \alpha|\Psi|^2 + \frac{\beta}{2}|\Psi|^4 + \frac{1}{2m^*}\left|\left(-i\hbar\nabla - q\vec{A}\right)\Psi\right|^2 + \frac{|\vec{B}|^2}{2\mu_0}, \tag{2.8}$$

where α and β are phenomenological coefficients, m^* is the effective Cooper-pair mass, and f_n is the free energy density of the normal state.

Minimizing Eq. (2.8) with respect to Ψ^* and $\vec{A}$ yields the coupled GL equations:

$$\alpha\Psi + \beta|\Psi|^2\Psi + \frac{1}{2m^*}\left(-i\hbar\nabla - q\vec{A}\right)^2\Psi = 0, \tag{2.9}$$

$$\vec{j}_s = -\frac{iq\hbar}{2m^*}(\Psi^*\nabla\Psi - \Psi\nabla\Psi^*) - \frac{q^2}{m^*}|\Psi|^2\,\vec{A}. \tag{2.10}$$

From these equations follow two characteristic length scales: the *coherence length*

$$\xi_\mathrm{GL} = \sqrt{\frac{\hbar^2}{2m^*|\alpha|}}, \tag{2.11}$$

which determines the distance over which the order parameter can vary significantly, and the *penetration depth*

$$\lambda_{\mathrm{GL}} = \sqrt{\frac{m^*\beta}{\mu_0 q^2 |\alpha|}}, \tag{2.12}$$

which describes the exponential decay of magnetic fields inside the material. In the weak-field limit near T_c, λ_{GL} approaches the London penetration depth λ_L extrapolated to the same temperature. The ratio $\kappa = \lambda_{\mathrm{GL}}/\xi_{\mathrm{GL}}$ defines the Ginzburg–Landau parameter distinguishing type-I ($\kappa < 1/\sqrt{2}$) and type-II ($\kappa > 1/\sqrt{2}$) superconductors.

Close to the critical temperature, α varies linearly as $\alpha(T) = \alpha'(T - T_\mathrm{c})$ with $\alpha' > 0$, while β remains constant. Minimization of Eq. (2.8) with respect to $|\Psi|$ yields the equilibrium condition $|\Psi_0|^2 = -\alpha/\beta$. Substituting this into the free energy gives the condensation energy density

$$f_\mathrm{n} - f_\mathrm{s} = \frac{B_c^2}{2\mu_0} = \frac{\alpha^2}{2\beta}, \tag{2.13}$$

where B_c is the *thermodynamic critical field*, i.e., the magnetic field strength at which the free energies of the superconducting and normal states are equal.

The GL formalism provides a quantitative description of spatial variations, vortex formation, and the transition between superconducting and normal regions. Its macroscopic phase ϕ directly leads to the phenomenon of flux quantization discussed next.

2.1.3 Flux quantization

One consequence of macroscopic phase coherence is the quantization of magnetic flux in a superconducting loop. For the condensate wave function $\Psi(\vec{r}) = \sqrt{n_\mathrm{s}} e^{i\phi(\vec{r})}$, single-valuedness requires that the phase change around a closed contour L within the superconductor is an integer multiple of 2π:

$$\oint_L \nabla\phi \cdot d\vec{l} = 2\pi n, \tag{2.14}$$

where n is an integer winding number.

The canonical momentum in a magnetic field is

$$\vec{p} = m^*\vec{v}_s + q\,\vec{A}, \tag{2.15}$$

with $\vec{v}_s$ the superfluid velocity. Using the gauge-invariant relation $\hbar\nabla\phi = m^*\vec{v}_s + q\vec{A}$ and inserting it into Eq. (2.14) gives

$$\oint_L \left(m^*\vec{v}_s + q\,\vec{A}\right)\cdot d\vec{l} = nh. \tag{2.16}$$

If the integration path is chosen far from the surface, where $\vec{v}_s \to 0$, only the vector potential contributes. Applying Stokes' theorem yields the quantization of the magnetic flux through the enclosed area S:

$$\Phi = \oint_L \vec{A}\cdot d\vec{l} = n\frac{h}{2e} = n\Phi_0, \tag{2.17}$$

with the flux quantum

$$\Phi_0 = \frac{h}{2e} \approx 2.07 \times 10^{-15}\,\text{Wb}. \tag{2.18}$$

Flux quantization is a direct result of the single-valued macroscopic phase and constitutes the foundation of superconducting interference devices, flux qubits, and related circuits underlying the phase–flux relationship.

2.2 The Josephson effect

A particularly remarkable manifestation of quantum mechanics in superconductors is the Josephson effect, which links the macroscopic phase coherence of the condensate to a measurable current and voltage across a thin insulating barrier. It represents the fundamental quantum mechanical coupling between two macroscopic wavefunctions and forms the basis of all superconducting quantum devices investigated in this thesis.

In 1962, Brian D. Josephson predicted that superconducting charge carriers can coherently tunnel between two superconductors separated by a thin insulating barrier, forming a weak link. [49]. This coupling between two condensates allows for charge transport governed purely by the quantum phase difference, without dissipation. The prediction, soon verified experimentally [50, 51], established that a supercurrent can flow without any applied voltage as a consequence of the phase difference $\varphi = \phi_1 - \phi_2$ between the superconducting order parameters on both sides of the junction. The two superconductors are described by macroscopic wavefunctions $\Psi_1 = \sqrt{n_{s,1}}e^{i\phi_1}$ and $\Psi_2 = \sqrt{n_{s,2}}e^{i\phi_2}$, and weak coupling through the insulating barrier allows for coherent tunnelling described by the *Josephson equations*

$$I_s = I_c \sin\varphi, \tag{2.19}$$

$$\frac{d\varphi}{dt} = \frac{q}{\hbar}V \qquad (q = 2e). \tag{2.20}$$

Equation (2.19) expresses the *DC Josephson effect*: a phase difference drives a dissipationless supercurrent even at zero voltage, while Eq. (2.20) describes the *AC Josephson effect*: a finite voltage induces a time-dependent phase and an oscillating current with frequency $f_J = (2e/h)V$. These equations reveal that the superconducting phase difference behaves as a macroscopic quantum variable whose dynamics determine measurable electrical observables.

Historically and conceptually, the Josephson effect forms the foundation for the work honored by the *2025 Nobel Prize in Physics*, awarded to Clarke, Devoret, and Martinis for demonstrating macroscopic quantum tunnelling and energy quantization in superconducting circuits [52]. Their experiments confirmed that φ behaves as a macroscopic quantum coordinate capable of tunnelling between adjacent minima of $U(\varphi)$, establishing Josephson junctions as analogues of quantum particles in periodic potentials [53–55].

2.2.1 The Josephson potential and nonlinearity

The potential energy of a Josephson junction follows directly by integration of the current–phase relation, Eq. (2.19), by integrating the current–phase relation with respect to the phase φ (using $\Phi = (\Phi_0/2\pi)\varphi$):

$$U(\varphi) = \int_0^{\varphi} I_s(\varphi') \frac{\Phi_0}{2\pi} d\varphi' = \frac{\Phi_0 I_c}{2\pi}(1 - \cos\varphi) = -E_J \cos\varphi + \text{const.}, \tag{2.21}$$

which defines the Josephson energy

$$E_J = \frac{\hbar I_c}{2e}. \tag{2.22}$$

The Josephson potential is intrinsically nonlinear due to the sinusoidal current–phase relation. As a result, the energy stored in the junction depends nonlinearly on the phase difference across it. The critical current I_c, set by microscopic properties such as the junction geometry and barrier transparency, determines the overall scale of both the Josephson potential and the associated inductive response.

The nonlinear energy–phase relation of a Josephson junction results in a phase-dependent differential inductance, commonly described by the *Josephson inductance*,

$$L_J(\varphi) = \left(\frac{\partial I_s}{\partial \Phi}\right)^{-1} = \left(\frac{2\pi}{\Phi_0}\frac{\partial I_s}{\partial \varphi}\right)^{-1} = \frac{\Phi_0}{2\pi I_c \cos\varphi}\,, \tag{2.23}$$

which reduces at $\varphi \approx 0$ to the linear inductance $L_J^0 = \Phi_0/(2\pi I_c)$.

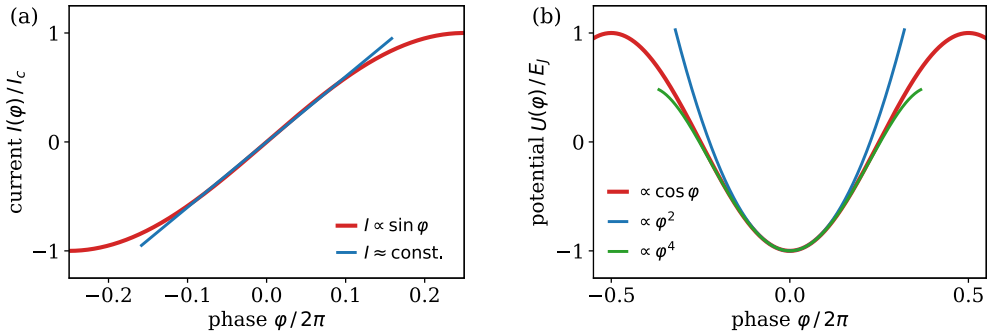

Figure 2.1: Current–phase relation and potential of a Josephson tunnel junction. (a) Sinusoidal current–phase relation of a Josephson junction (red) and a linear approximation at small phase drops across the junction (blue). (b) Josephson potential $U(\varphi)$ (red) and its harmonic approximation (blue), valid for small φ. Higher-order terms, such as the quartic contribution (green), introduce nonlinearity essential for qubits and parametric devices.

Expanding the Josephson potential for small phase differences ($\varphi \ll 1$),

$$U(\varphi) \approx -E_\mathrm{J} + \frac{E_\mathrm{J}}{2}\varphi^2 - \frac{E_\mathrm{J}}{24}\varphi^4, \tag{2.24}$$

reveals a harmonic term corresponding to a linear inductor and higher-order corrections that introduce anharmonicity [56]. This intrinsic nonlinearity is essential for qubit operation and parametric amplification, as it enables energy-level anharmonicity and a nonlinear circuit response [57, 58].

2.2.2 Josephson inductance and kinetic inductance

Large inductances play a central role in superconducting quantum circuits, in particular for realizing high-impedance elements and suppressing charge fluctuations, as required for flux-type qubits, high-impedance resonators, and parametric devices [2, 3, 5]. In practice, such inductances can arise from two closely related physical mechanisms: the inertial response of superconducting charge carriers in continuous superconductors, known as *kinetic inductance*, and the phase dynamics across Josephson tunnel junctions, described by the *Josephson inductance*. This section highlights the physical origin of both contributions and clarifies their close conceptual connection, which underlies the concept of a superinductance.

In a conventional superconducting wire, an applied electric field accelerates the superconducting charge carriers. Due to their finite effective mass, this acceleration is not instantaneous but leads to an inertial response, giving rise to an inductive

contribution even in the absence of magnetic field energy. This effect is referred to as kinetic inductance [56].

On a phenomenological level, the kinetic inductance of a uniform superconducting conductor of length l and cross-sectional area A can be written as [47]

$$L_\mathrm{k} = \frac{m^*}{n_\mathrm{s} q^2} \frac{l}{A}, \tag{2.25}$$

where m^* and n_s denote the effective mass and density of superconducting charge carriers. The kinetic inductance thus increases for reduced carrier density and small cross sections, making it particularly relevant in thin and disordered superconducting films, where structural disorder, granularity, or reduced dimensionality suppress the superfluid density n_s and strongly enhance the kinetic inductance.

For thin superconducting films of thickness d and width w, the cross-sectional area is given by $A = wd$. In this geometry, it is convenient to express the kinetic inductance in Eq. (2.25) in terms of the inductance per square,

$$L_\mathrm{k}^\square = \mu_0 \frac{\lambda_\mathrm{L}^2}{d}, \tag{2.26}$$

which depends only on the film thickness d and the London penetration depth λ_L.

For bulk aluminum with $\lambda_\mathrm{L} \approx 50\,\mathrm{nm}$ and a film thickness of $d = 100\,\mathrm{nm}$, this corresponds to a sheet kinetic inductance of $L_\mathrm{k}^\square \approx 30\,\mathrm{pH}$ [59]. In contrast, in strongly disordered superconductors such as granular aluminum, niobium nitride, or titanium nitride, the sheet kinetic inductance can reach values of several nanohenries [18–20, 60]. These large values have enabled the realization of high-impedance resonators and superinductors based on continuous materials [5, 7].

While materials with a large kinetic inductance provide one route toward compact superinductors, their properties are intrinsically linked to material disorder and often accompanied by increased losses and parameter variability [7, 19, 24, 26]. As a result, circuit parameters are largely set by microscopic material properties and offer only limited tunability at the circuit-design level [5, 7].

An alternative and conceptually closely related approach to realizing large inductances is provided by Josephson tunnel junctions. As discussed in Sec. 2.2.1, the nonlinear energy–phase relation of a Josephson junction gives rise to a phase-dependent Josephson inductance. This inductive response originates from coherent charge transport across the insulating barrier and can be regarded as a discrete analogue of kinetic inductance [47].

In contrast to bulk or thin-film superconductors, the Josephson inductance is a circuit-level property set by the junction critical current. The critical current is

determined by the junction geometry and by fabrication parameters governing the formation of the tunnel barrier (see Sec. 2.2.4), enabling precise control at the circuit-design level. By connecting many junctions in series, a large effective inductance can be realized, with its value determined by the number of junctions and the Josephson inductance of each junction. This principle forms the foundation of the stacked junction inductors employed in this work (see Sec. 5.1).

Both kinetic inductance in superconducting materials and Josephson inductance in tunnel junctions thus originate from the inertial response of the superconducting condensate, providing two complementary routes to realizing large inductances in superconducting circuits.

2.2.3 Quasiparticles and the superconducting energy gap

The concepts introduced in this section form the basis for interpreting microscopic effects in the cryogenic current–voltage characteristics of Josephson junctions discussed throughout this thesis. In particular, the superconducting energy gap and quasiparticle excitations contribute to the characteristic voltage scale, subgap leakage, and dissipation mechanisms observed in transport measurements of stacked junction arrays.

The microscopic origin of superconductivity was explained by Bardeen, Cooper, and Schrieffer (BCS) [61]. For the purposes of this thesis, only the concepts directly relevant to Josephson transport and junction dynamics are summarized here, namely the superconducting energy gap Δ and the fermionic quasiparticle excitations that govern tunnelling and dissipation in junctions.

Electrons near the Fermi surface experience an effective phonon-mediated attraction within the Debye window $\hbar\omega_{\mathrm{D}}$, leading to the formation of bound Cooper pairs. Within BCS theory, the binding energy of a Cooper pair is given by the superconducting energy gap Δ, which in the weak-coupling limit is

$$\Delta_0 = 1.76\, k_{\mathrm{B}} T_{\mathrm{c}}, \tag{2.27}$$

where Δ_0 denotes the energy gap at zero temperature. This relation accurately describes superconductors such as aluminum and niobium and agrees with tunnelling spectroscopy measurements of the gap [47, 62]. When a Cooper pair is broken by an excitation with energy at least Δ, two unbound fermionic excitations are created, which are referred to as quasiparticles.

The superconducting energy gap is temperature dependent. At zero temperature, the equilibrium quasiparticle density vanishes, while the energy gap assumes its

maximum value Δ_0. With increasing temperature, thermally excited quasiparticles are generated and the gap $\Delta(T)$ decreases continuously, eventually closing at the critical temperature T_c. This temperature dependence is well described by the empirical interpolation

$$\frac{\Delta(T)}{\Delta_0} \approx \tanh\left[1.74\sqrt{\frac{T_c}{T}-1}\right], \tag{2.28}$$

which captures the behaviour predicted within BCS theory [47, 63]. The temperature dependence of the energy gap directly influences measurable transport quantities such as the critical current and the onset of quasiparticle conduction in the I–V characteristics of Josephson junctions (see the A.–B. relation in Eq. (2.32)).

In the superconducting state, the energy spectrum of fermionic excitations is modified compared to the normal state. Instead of a constant density of available electronic states, the quasiparticle density of states becomes energy dependent and exhibits a gap of width 2Δ around the Fermi level. Within BCS theory, the quasiparticle density of states is given by

$$N_s(E) = \begin{cases} 0, & |E| < \Delta, \\ N_0 \dfrac{|E|}{\sqrt{E^2-\Delta^2}}, & |E| > \Delta, \end{cases} \tag{2.29}$$

where E denotes the quasiparticle energy measured relative to the Fermi energy, $N_s(E)$ is the density of quasiparticle states in the superconducting state, and N_0 is the normal-state density of states at the Fermi level.

The divergence of $N_s(E)$ at $|E| = \Delta$ reflects the accumulation of available quasiparticle states at the gap edges. These singularities, commonly referred to as coherence peaks, are a direct consequence of Cooper pairing and constitute a hallmark of the superconducting state. In superconducting–insulator–superconducting (SIS) junctions, they give rise to a sharp increase of the tunnelling current once the applied bias voltage exceeds the gap voltage. This behaviour forms the basis of tunnelling spectroscopy, in which the differential conductance directly probes the quasiparticle density of states [50, 51, 62].

While the density of states describes the energy distribution of available quasiparticle states, the actual number of quasiparticles is determined by their thermal population. At temperatures much smaller than the critical temperature T_c, as relevant for all measurements in this thesis, the equilibrium quasiparticle density

$$n_{qp}(T) \propto N_0\sqrt{2\pi k_B T\,\Delta(T)}\,\exp\left[-\frac{\Delta(T)}{k_B T}\right] \tag{2.30}$$

is exponentially suppressed, reflecting the energy cost required to excite quasiparticles across the superconducting energy gap. In the ideal low-temperature limit, this suppression implies vanishing quasiparticle-induced dissipation.

In real devices, however, nonequilibrium quasiparticles may persist even at millikelvin temperatures and can contribute to finite subgap currents, in addition to other circuit- and geometry-related effects, through inelastic or multiparticle tunnelling and Andreev-like processes [47, 64, 65]. Such effects become directly visible in high-resolution transport measurements and provide valuable information for assessing junction quality and dissipation in superconducting circuits.

The existence of the superconducting energy gap manifests macroscopically in the characteristic voltage scale of Josephson junctions,

$$V_{\mathrm{gap}} = \frac{2\Delta(T)}{e}, \tag{2.31}$$

which marks the onset of strong quasiparticle tunnelling in the measured I–V characteristics.

Quasiparticles generated above the gap recombine into Cooper pairs by emitting phonons with energy 2Δ, a process characterized by the recombination time τ_{qp}, which depends on temperature and material parameters [66]. Under DC bias or strong microwave drive, nonequilibrium quasiparticle populations can persist, leading to excess dissipation, local heating, or features such as the backbending of the quasiparticle branch discussed later in Sec. 2.2.5 [67–69]. Understanding quasiparticle generation and relaxation is therefore helpful for interpreting transport measurements and discussing dissipation mechanisms in stacked Josephson junction circuits.

2.2.4 The critical current

The critical current I_{c} represents one of the most fundamental quantities of a Josephson junction, defining the maximum supercurrent that can pass through the weak link without developing a voltage across it. It provides a direct link between the microscopic properties of the superconducting electrodes, the tunnel barrier, and the macroscopic circuit behavior. In the context of Josephson inductors, I_{c} determines the nonlinear inductance in Eq. (2.23), which at small phase excursions $\varphi \ll 1$ simplifies to $L_{\mathrm{J}} \approx \Phi_0/(2\pi I_{\mathrm{c}})$. Controlling I_{c} therefore provides a direct means to set the inductance in superconducting circuits, such as in qubits, SQUIDs, and other non-dissipative superconducting devices.

At the microscopic level, the critical current arises from the coherent tunneling of Cooper pairs through the insulating barrier separating two superconductors. In the tunneling limit of a low-transparency barrier, Ambegaokar and Baratoff derived the relation [70]:

$$I_c R_n = \frac{\pi \Delta(T)}{2e} \tanh\left(\frac{\Delta(T)}{2k_B T}\right) \xrightarrow[T\to 0]{} \frac{\pi \Delta_0}{2e} \simeq 2.34 \times 10^{-4}\,\mathrm{V\,K^{-1}}\,\frac{T_c}{R_n}, \tag{2.32}$$

where $\Delta(T)$ is the superconducting energy gap and $\Delta_0 = 1.76\,k_B T_c$ its zero-temperature value from BCS theory. For aluminum with $T_c = 1.20\,\mathrm{K}$ and $\Delta_0 \simeq 180\,\mu\mathrm{eV}$ [62, 71], one obtains

$$I_c R_n \approx \frac{\pi \Delta_0}{2e} \approx 0.28\,\mathrm{mV}, \tag{2.33}$$

in agreement with typical experimental data for $\mathrm{Al/AlO}_x\mathrm{/Al}$ tunnel junctions [51, 72]. Equation (2.32) thus provides a direct relation between the superconducting energy gap and measurable macroscopic transport parameters.

For junctions with uniform tunnel barriers, the critical current scales linearly with the junction area A according to [56]

$$I_c = J_c\, A_J, \tag{2.34}$$

where J_c denotes the critical current density. The strong sensitivity of J_c to the tunnel barrier thickness t_b results from the exponential dependence of the transmission probability on barrier width and height. Within a semiclassical Wentzel–Kramers–Brillouin (WKB) picture of electron tunneling through a rectangular barrier of height Φ_b, one obtains [72, 73]:

$$J_c \propto \exp\left[-\frac{2t_b}{\hbar}\sqrt{2m_e \Phi_b}\right], \tag{2.35}$$

where m_e is the electron mass. This expression illustrates that even sub-ångström variations in t_b or Φ_b can cause orders-of-magnitude changes in J_c.

Experimentally, the barrier thickness is controlled through the oxidation of the aluminum layer, characterized by the oxygen exposure $\mathcal{E} = p_{O_2}\, t_{ox}$, where p_{O_2} is the partial pressure and t_{ox} the oxidation time. Empirically, the dependence of J_c on $\mathcal{E}$ follows a power law [74, 75]:

$$J_c \propto \mathcal{E}^{-\alpha}, \tag{2.36}$$

with the exponent α depending on the oxygen exposure. At low J_c (below $\sim 0.1\,\mathrm{mA/\mu m^2}$), $\alpha \approx 0.4$–0.6 is typically observed, while in the high-J_c regime α can

increase up to ~ 1.6. All junctions discussed in this thesis operate in the low-J_c regime, and $\alpha = 0.4$ is used in the relevant calculations.

In $Al/AlO_x/Al$ junctions, deviations from the ideal exponential dependence of J_c on barrier thickness can arise from microscopic non-uniformities of the oxide, such as inhomogeneous oxidation or interface roughness, which affect both the normal-state resistance R_n and the subgap leakage current [51]. As a result, small variations in barrier thickness can lead to significant device-to-device variations in I_c and thus in the Josephson inductance, particularly for sub-micron junctions. In this work, this strong sensitivity is not merely a limitation but is explicitly exploited in the fabrication of stacked junction arrays, where controlled variations of the oxidation conditions are used to compensate geometric non-uniformities within a stack. This approach is discussed in detail in Sec. 5.5.2.

2.2.5 Dynamics of the Josephson junction (RCSJ model)

The dynamics of a current-biased Josephson junction are well described by the *resistively and capacitively shunted junction* (RCSJ) model [76, 77]. It represents the junction as three parallel branches: the lossless Josephson element, a normal resistance R_n accounting for quasiparticle tunneling, and a capacitance C_J describing charge accumulation across the barrier (see inset of Fig. 2.2 (a)). This model captures both the static and dynamic behavior of the junction and provides the theoretical basis for understanding its current–voltage (I–V) characteristics.

The total current through the junction is

$$I = I_c \sin\varphi + \frac{V}{R_n} + C_J \frac{dV}{dt} \overset{\text{Eq. (2.20)}}{=} I_c \sin\varphi + \frac{\Phi_0}{2\pi R_n}\dot{\varphi} + \frac{C_J \Phi_0}{2\pi}\ddot{\varphi}, \tag{2.37}$$

where V denotes the voltage across the junction. This nonlinear differential equation describes the time evolution of the phase difference φ. Depending on the relative strength of dissipation and inertia, the phase dynamics give rise to qualitatively different regimes of junction behavior, which are conveniently classified within the RCSJ framework.

It is convenient to normalize all quantities by the critical current I_c and introduce the reduced bias $i_b = I/I_c$, the characteristic frequency $\omega_c = 2\pi I_c R_n/\Phi_0$, and the Stewart–McCumber parameter

$$\beta_c = \frac{2\pi I_c R_n^2 C_J}{\Phi_0}. \tag{2.38}$$

Equation (2.37) then becomes

$$\ddot{\varphi} + \frac{1}{\sqrt{\beta_c}}\dot{\varphi} + \sin\varphi = i_b. \tag{2.39}$$

Here, time is normalized to the inverse plasma frequency ω_p^{-1}, such that the damping term is given by the inverse quality factor $1/Q = 1/\sqrt{\beta_c}$. Equation (2.39) is mathematically equivalent to the equation of motion of a particle of mass $m_\varphi = C_J(\Phi_0/2\pi)^2$ moving in a potential

$$U(\varphi) = -E_J(\cos\varphi + i_b\varphi)\,, \tag{2.40}$$

subject to viscous damping with damping coefficient $\eta = (\Phi_0/2\pi)^2/R_n$. The potential (2.40) has the shape of a *tilted washboard* shown in Fig. 2.2 (a), periodic in φ and tilted by the bias current. The resulting phase dynamics strongly depends on the applied bias current, which controls both the tilt of the potential and the height of the barriers separating adjacent minima.

For small bias currents $i_b \ll 1$, the minima of $U(\varphi)$ form a series of potential wells of depth

$$\Delta U(i_b) = 2E_J\left[\sqrt{1-i_b^2} - i_b \arccos(i_b)\right], \tag{2.41}$$

which decreases with increasing i_b and vanishes at $i_b = 1$. Small oscillations of the phase particle around a potential minimum occur at the *plasma frequency*

$$\omega_p(i_b) = \sqrt{\frac{2\pi I_c}{\Phi_0 C_J}}\,(1-i_b^2)^{1/4} \xrightarrow{i_b\to 0} \omega_p \equiv \sqrt{\frac{2\pi I_c}{\Phi_0 C_J}} \overset{\text{Eq. (2.23)}}{=} \frac{1}{\sqrt{L_J C_J}}, \tag{2.42}$$

which corresponds to the small-signal resonance frequency. [72]. Equivalently, it can be expressed in terms of the Josephson energy E_J (Eq. (2.22)) and the charging energy E_C of a single junction capacitor, defined as

$$E_C = \frac{e^2}{2C_J}, \tag{2.43}$$

which quantifies the electrostatic energy cost associated with adding a Cooper pair to the junction capacitance. In terms of E_J and E_C, the plasma frequency reads

$$\omega_p = \frac{1}{\hbar}\sqrt{8E_J E_C}. \tag{2.44}$$

This expression emphasizes that the plasma oscillation originates from the interplay between the Josephson potential energy and the capacitive charging energy. The

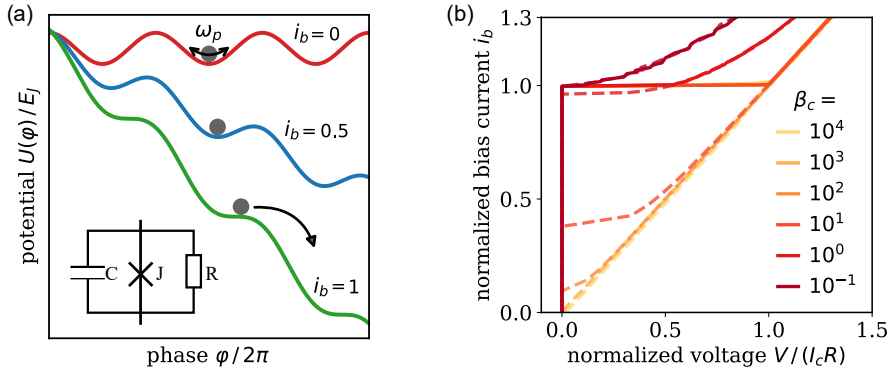

Figure 2.2: Resistively and capacitively shunted junction (RCSJ) model. (a) Tilted washboard potential $U(\varphi)$ of a current-biased Josephson junction for different bias currents i_b. For $i_\mathrm{b} < 1$, the phase particle is trapped and oscillates at the plasma frequency ω_p. At $i_\mathrm{b} = 1$, the barrier vanishes; for $i_\mathrm{b} > 1$ the particle runs down the potential, yielding a finite time-averaged voltage. (b) Simulated current–voltage characteristics for different Stewart–McCumber parameters β_c. Overdamped junctions ($\beta_\mathrm{c} \ll 1$) are non-hysteretic, while underdamped junctions ($\beta_\mathrm{c} \gg 1$) show pronounced switching and retrapping.

competition between E_J and E_C determines the nature of the junction dynamics and the validity of a phase-based description. Based on these characteristic energy and frequency scales, distinct dynamical regimes of the Josephson junction can be identified, depending on the damping strength and the applied bias.

The RCSJ model applies in the regime $E_\mathrm{C} \ll E_\mathrm{J}$, where the phase φ is a good quantum variable and the dynamics correspond to oscillations in a nearly harmonic potential. In the opposite limit $E_\mathrm{C} \gg E_\mathrm{J}$, charge quantization dominates and the junction enters the Coulomb blockade regime (Sec. 2.2.6).

When i_b exceeds 1, the phase starts to run freely through successive minima. Averaging $\dot{\varphi}$ over time and using $V = (\Phi_0/2\pi)\dot{\varphi}$ yields the finite-voltage branch of the I–V curve. The resulting current–voltage characteristic thus naturally contains a zero-voltage branch ($i_\mathrm{b} < 1$) and a finite-voltage branch ($i_\mathrm{b} > 1$).

The damping determines whether transitions between these branches are reversible, as illustrated in Fig. 2.2 (b). Using the definitions of ω_c and ω_p, the Stewart–McCumber parameter (2.38) can also be written as

$$\beta_\mathrm{c} = \left(\frac{\omega_\mathrm{c}}{\omega_\mathrm{p}}\right)^2, \tag{2.45}$$

and the corresponding quality factor as

$$Q = \omega_\mathrm{p} R_\mathrm{n} C_\mathrm{J} = \omega_\mathrm{p} \tau_{RC} = \sqrt{\beta_\mathrm{c}}. \tag{2.46}$$

Physically, Q quantifies the ratio of *reactive energy stored per cycle* to *energy dissipated per cycle* in the junction; large Q (equivalently large β_c) indicates underdamped dynamics with pronounced inertia of the phase and clear hysteresis, while small Q corresponds to overdamped, non-hysteretic I–V curves [47, 72]. Typical operating regimes are: (i) *overdamped* ($Q < 1$, $\beta_c \ll 1$) for non-hysteretic logic/mixer devices (e.g., RSFQ and SIS mixers) [78, 79]; (ii) *moderately to strongly underdamped* ($Q \sim 3$–30, $\beta_c \sim 10$–10^3) for switching and macroscopic quantum tunneling experiments [80, 81]. In coherent superconducting qubits (transmon, flux, phase), individual $\mathrm{Al/AlO}_x\mathrm{/Al}$ junctions are typically embedded in high-Q microwave circuits with a shunt capacitance; their intrinsic junction dynamics are underdamped ($\beta_c \gg 1$), yet the device operates in the linear, small-signal regime where coherence is set by external losses rather than DC hysteresis [82–84].

The qualitative shape of the current–voltage characteristics is governed by the damping of the phase dynamics, quantified by the Stewart–McCumber parameter β_c. For $\beta_c \ll 1$ ($Q < 1$), the junction is overdamped and exhibits a single-valued, non-hysteretic I–V curve. For $\beta_c \gg 1$ ($Q > 1$), it is underdamped and hysteretic: the phase remains trapped until the bias reaches a *switching current* $I_{sw} \approx I_c$ and retraps at a lower *retrapping current*

$$I_r \approx \frac{4I_c}{\pi\sqrt{\beta_c}}, \tag{2.47}$$

as obtained from energy-balance arguments [72]. Beyond this deterministic picture, thermal and quantum fluctuations introduce stochastic escape processes that modify the observed switching behavior.

At finite temperature, such fluctuations can excite the phase over the barrier (2.41) before reaching $i_b = 1$. The escape rate follows Kramers' model for activated escape [85]:

$$\Gamma_{TA}(i_b, T) = \frac{\omega_p(i_b)}{2\pi Q}\,\exp\left[-\frac{\Delta U(i_b)}{k_B T}\right]. \tag{2.48}$$

The measured switching current I_{sw} therefore becomes smaller than I_c and exhibits a statistical spread related to Γ_{TA}.

At sufficiently low temperatures, the phase escapes not by thermal activation but by tunneling through the barrier. This *macroscopic quantum tunneling* (MQT) regime has been observed in $\mathrm{Al/AlO}_x\mathrm{/Al}$ junctions below approximately $T \lesssim 200\,\mathrm{mK}$ [54, 68, 81]. In this regime, the escape rate is given by

$$\Gamma_{MQT} = a_q\,\omega_p(i_b)\exp\left[-\frac{36\,\Delta U(i_b)}{5\hbar\omega_p(i_b)}\right], \tag{2.49}$$

where $a_q \approx (864\pi\,\Delta U/\hbar\omega_p)^{1/2}$ accounts for quantum fluctuations [47, 86]. The crossover between thermally activated and quantum tunneling escape occurs when $k_B T \simeq \hbar\omega_p/2\pi$.

When escape and retrapping occur repeatedly on experimentally relevant timescales, for example due to increased damping or environmental noise, the junction enters a distinct dynamical regime characterized by diffusive phase motion. This regime, known as *phase diffusion*, produces a finite time-averaged voltage even below I_c and results in a rounded transition region in the I–V curve. The average voltage in the diffusive regime can be approximated by [80]

$$\langle V\rangle = R_n I_c \,\frac{i_b}{Q}\,\frac{\sinh(\pi i_b/Q)}{\cosh(\pi i_b/Q)-\cos(\pi/Q)}. \tag{2.50}$$

As temperature or noise level rises, the switching current becomes increasingly suppressed, signaling the crossover from underdamped to overdamped phase dynamics [80, 87].

In addition to phase dynamics near the critical current, the high- and intermediate-bias regions of the I–V characteristic are governed by quasiparticle transport. Below the gap voltage $eV < 2\Delta$, the finite subgap conductance defines the *subgap resistance* $R_{sg}(V,T)$, which captures inelastic and multiparticle tunneling as well as leakage through barrier inhomogeneities. The ratio R_{sg}/R_n is widely used as an empirical barrier quality metric: large values indicate low subgap leakage and a homogeneous, pinhole-free oxide. High-quality $Al/AlO_x/Al$ junctions reach $R_{sg}/R_n \gtrsim 50$ (sometimes $\gtrsim 100$, depending on bias definition) at low T; significantly smaller ratios suggest inhomogeneous oxidation or extra conduction paths [47].

In the quasiparticle branch, deviations from a constant gap voltage often appear as a slight downturn or "backbending" just above V_{gap}. This behavior arises from nonequilibrium heating and quasiparticle relaxation in the electrodes [67, 88]. The effective local gap $\Delta_{eff}(I)$ decreases with current due to self-heating,

$$\Delta_{eff}(I) \approx \Delta_0\left[1-\left(\frac{P(I)}{P_{th}}\right)^{1/2}\right], \tag{2.51}$$

where $P(I) = IV$ is the dissipated power and P_{th} denotes an effective thermal power scale set by electron–phonon coupling and heat evacuation from the junction electrodes. For $Al/AlO_x/Al$ junctions with areas of order $A \sim 1\,\mu m^2$ at millikelvin temperatures, P_{th} is on the order of a few to several tens of nanowatts, depending on electrode volume and thermalization [68, 88]. In well-thermalized $Al/AlO_x/Al$ junctions with small $P(I)$, this effect is strongly reduced [68, 88].

In the quasiparticle-dominated high-bias regime ($eV \gg 2\Delta$) the I–V characteristic approaches an ohmic line with slope R_n. Including the charging energy $E_\mathrm{C} = e^2/(2C_\mathrm{J})$ of the junction capacitance gives the linear asymptote

$$V(I) \xrightarrow[eV \gg 2\Delta]{} I\,R_\mathrm{n} + \frac{E_\mathrm{C}}{e}, \tag{2.52}$$

which reflects the average work per *electron* to charge the junction during tunneling (for purely pairwise transfer it would be $2E_\mathrm{C}/e$). Equation (2.52) holds provided (i) the quasiparticle branch is ohmic, (ii) environmental impedances do not add extra nonlinearity, and (iii) multiparticle/Andreev contributions are negligible; see the orthodox theory and reviews in [47, 89, 90]. In this work, Eq. (2.52) is applied only in the high-bias quasiparticle regime well above the gap, which in the measured I–V characteristics corresponds to bias currents well above the critical currents of the junctions in the array, where the response is clearly linear. Under these conditions, the equation provides a good approximation for the stacked $\mathrm{Al/AlO}_x\mathrm{/Al}$ junctions studied here.

2.2.6 Josephson junctions in the charge–dominated regime

In the limit of ultrasmall Josephson junctions or narrow superconducting wires, the phase of the order parameter ceases to behave as a purely classical variable and can undergo quantum fluctuations. Such events, known as *quantum phase slips* (QPS), correspond to tunnelling of the superconducting phase by 2π, accompanied by a temporary suppression of the supercurrent [91–93]. They are the dual process to Cooper-pair tunnelling and become relevant when the Josephson energy $E_\mathrm{J} = \hbar I_\mathrm{c}/2e$ (Eq. (2.22)) is comparable to or smaller than the charging energy $E_\mathrm{C} = e^2/2C_\mathrm{J}$ (Eq. (2.43)) of the junction.

For large junctions ($E_\mathrm{J} \gg E_\mathrm{C}$), the phase is well localized and quantum fluctuations are negligible, corresponding to the classical regime. When $E_\mathrm{J}/E_\mathrm{C} \lesssim 1$, however, the phase becomes delocalized, QPS processes occur, and the charge degree of freedom acquires importance. These effects can lead to suppression of the supercurrent, Coulomb blockade of Cooper-pair tunnelling, and an effective flux noise contribution sometimes referred to as *Aharonov–Casher noise* [2, 94, 95].

The semiclassical tunnelling amplitude for a single phase slip is [72, 92]

$$\Gamma_\mathrm{QPS} \propto \omega_\mathrm{p} \sqrt{\frac{S_0}{2\pi\hbar}}\, e^{-S_0/\hbar}, \qquad S_0 \approx 8\sqrt{\frac{2E_\mathrm{J}}{E_\mathrm{C}}}, \tag{2.53}$$

where $\omega_\mathrm{p} = \sqrt{8E_\mathrm{J}E_\mathrm{C}}/\hbar$ is the plasma frequency (Eq. (2.44)). Thus, QPS are exponentially suppressed in the phase-dominated regime ($E_\mathrm{J}/E_\mathrm{C} \gg 1$) but grow rapidly as junctions become smaller and the capacitance decreases.

For aluminum tunnel junctions in stacks with parameters relevant to this work — critical currents $I_\mathrm{c} \approx 100$–$1000\,\mathrm{nA}$, $A_\mathrm{J} \approx 1$–$10\,\mu\mathrm{m}^2$ and capacitance densities $C/A_\mathrm{J} \approx 50\,\mathrm{fF}/\mu\mathrm{m}^2$ for $\mathrm{Al/AlO}_x\mathrm{/Al}$ barriers [47] — one obtains ratios

$$\frac{E_\mathrm{J}}{E_\mathrm{C}} = \frac{(\hbar/2e)I_\mathrm{c}}{e^2/(2C_\mathrm{J})} \approx 10^2\text{–}10^4,$$

placing all junctions studied here in the $E_\mathrm{J} \gg E_\mathrm{C}$ regime where QPS are exponentially suppressed. Only for ultrasmall areas ($A_\mathrm{J} \lesssim 0.01\ \mu\mathrm{m}^2$) or strongly oxidized barriers ($J_\mathrm{c} \lesssim 10\,\mathrm{A/cm}^2$) could $E_\mathrm{J}/E_\mathrm{C}$ approach unity, where phase fluctuations or Coulomb blockade effects become relevant [93, 95–97].

3 Flux qubits and their environment

Building on the superconducting circuit elements introduced in the previous chapter, this chapter establishes the theoretical framework required to describe and analyze superconducting flux qubits and begins with a brief overview of superconducting quantum bits. It introduces the circuit-level description of flux-type qubits operated in the quarton regime and outlines how their interaction with the electromagnetic environment and dominant noise sources enters the interpretation of experimental spectroscopy and time-domain measurements. The concepts developed here provide the basis for the experimental investigations presented in the subsequent chapters.

3.1 Superconducting quantum bits

Qubits, short for quantum bits, are quantum systems that can be regarded as artificial atoms with a discrete energy spectrum, where two well-separated energy levels encode quantum information [84, 98]. Superconducting qubits realize such artificial atoms in micrometer-scale electrical circuits fabricated from superconducting thin films and Josephson tunnel junctions. Their energy levels are determined by the circuit capacitances and inductances—similar to a microwave resonator—but with one crucial difference: the Josephson junction provides a nonlinear inductive element (Sec. 2.2.1). This intrinsic nonlinearity renders the circuit spectrum anharmonic and thereby enables selective control of the lowest transition without simultaneously exciting higher energy levels.

A linear LC resonator has equally spaced energy levels and therefore does not provide a spectrally isolated two-level subsystem [40]. To operate a circuit as a qubit, the energy spacing between the lowest transition and higher transitions must differ (Fig. 3.1 (a)). The transition frequency between the ground state $|0\rangle$ and the first excited state $|1\rangle$,

$$\omega_{01} \equiv \frac{E_1 - E_0}{\hbar}, \tag{3.1}$$

defines the qubit transition frequency–or short *qubit frequency*–and sets the characteristic energy scale for coherent control (Sec. 3.2.2). We quantify the deviation from a harmonic spectrum by the *anharmonicity*

$$\mathcal{A} \equiv \frac{(E_2 - E_1) - (E_1 - E_0)}{\hbar} = \omega_{12} - \omega_{01}, \tag{3.2}$$

where $\omega_{ij} = (E_j - E_i)/\hbar$ denote transition frequencies. A nonzero anharmonicity $\mathcal{A}$ is essential for qubit control because it allows resonant driving of the $|0\rangle \to |1\rangle$ transition at ω_{01} without inadvertently populating the next excited level $|2\rangle$ (or higher levels).

As reviewed in Sec. 2.2.1, the Josephson junction has an intrinsically nonlinear energy–phase relation,

$$U(\varphi) = -E_\mathrm{J} \cos\varphi + \text{const.}, \tag{3.3}$$

with the Josephson energy E_J set by the junction critical current (Eq. (2.22)). Figure 2.1 illustrates that for small phase excursions the Josephson potential is approximately harmonic, while higher-order terms—such as the quartic correction in Eq. (2.24)—provide the nonlinearity required for an anharmonic level structure. In superconducting qubits, this nonlinearity is combined with circuit capacitances that provide a kinetic (charging) energy scale [40]. For a junction capacitance C_J, the associated charging energy is defined as $E_\mathrm{C} = e^2/(2C_\mathrm{J})$ (Eq. (2.43)), and the interplay between E_J and E_C sets the characteristic frequency scales of Josephson circuits (see, e.g., the plasma frequency in Eq. (2.44)). More generally, in extended circuits E_C denotes an effective charging energy determined by all capacitances participating in the relevant circuit mode.

One widely used superconducting qubit implementation is a Josephson junction shunted by a large capacitor (Fig. 3.1 (b)), commonly referred to as the *transmon* qubit [82]. The shunt capacitor suppresses charge dispersion and stabilizes the device against offset-charge fluctuations, while the Josephson junction provides the nonlinearity that makes the spectrum anharmonic. Typical transmon devices operate at qubit frequencies of a few gigahertz, with an anharmonicity of a few hundred megahertz, sufficient for selective single-qubit control [40, 82].

Beyond fixed-frequency qubits, many superconducting circuit designs deliberately introduce additional degrees of freedom in order to shape the potential landscape and to tune device properties during operation *in situ*. Such tunability addresses practical challenges in multi-qubit quantum processors, including frequency crowding, controlled qubit–qubit interactions, and the implementation of fast and selective gate operations in large-scale architectures [84, 98]. A prominent

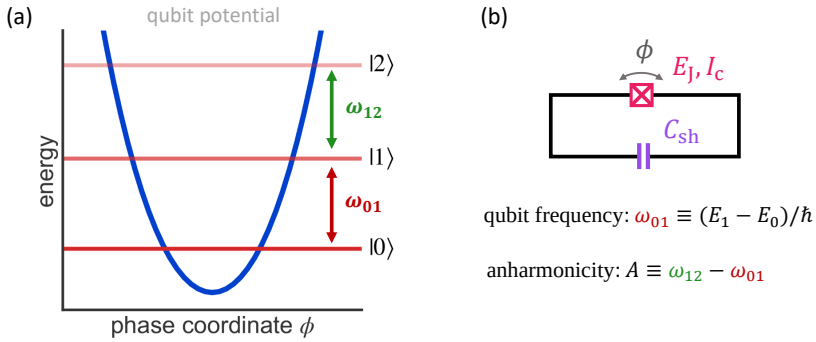

Figure 3.1: Anharmonic spectrum of a superconducting qubit: transmon example. (a) Schematic potential energy landscape of a superconducting qubit as a function of the superconducting phase coordinate ϕ. The discrete energy levels $|0\rangle$, $|1\rangle$, and $|2\rangle$ arise from quantization in the anharmonic potential. The qubit transition frequency is defined as $\omega_{01} = (E_1 - E_0)/\hbar$, while the separation between the $|0\rangle \to |1\rangle$ and $|1\rangle \to |2\rangle$ transitions defines the anharmonicity $\mathcal{A} = \omega_{12} - \omega_{01}$. The anharmonicity ensures that the lowest transition can be selectively addressed without populating higher excited states. (b) Example of a superconducting qubit circuit implemented as a Josephson junction shunted by a capacitor (fixed-frequency transmon qubit). In this circuit, the Josephson energy E_J, set by the junction critical current, and the effective charging energy E_C, determined by the circuit capacitance, set the shape of the potential in (a) and thereby determine both the qubit transition frequency ω_{01} and the anharmonicity $\mathcal{A}$.

example is the replacement of a single junction by a superconducting loop containing two junctions (a SQUID), which makes the circuit's effective Josephson energy tunable via an externally applied magnetic flux, enabled by flux quantization in superconducting loops (Sec. 2.1.3) [40]. More generally, adding superconducting loops and inductive elements such as junction arrays enables circuit potentials with multiple minima, symmetry points, and tailored curvatures.

Different circuit architectures emphasize different trade-offs between anharmonicity, coherence, circuit footprint, and tunability. For example, the fluxonium circuit was proposed to combine a large inductance with strong anharmonicity and reduced sensitivity to charge noise, enabling long coherence times at the expense of an increased sensitivity to magnetic flux [2]. Similar considerations motivate a broad range of superconducting qubit designs that are actively explored in the context of scalable quantum processors [4, 84, 98].

In flux-type circuits, the relevant bias parameter is the magnetic flux threading a superconducting loop. Changes of the effective flux bias therefore translate into

changes of the transition frequency (and other qubit properties such as anharmonicity),

$$\delta\omega_{01}(t) \;\approx\; \left(\frac{\partial\omega_{01}}{\partial\Phi}\right)\delta\Phi(t) + \dots. \tag{3.4}$$

Unintended fluctuations of the flux bias—for example due to magnetic noise in the qubit environment—lead to temporal fluctuations of qubit parameters and cause dephasing of the qubit state, motivating the detailed discussion of flux noise in Sec. 3.3.2.

The quarton devices investigated in this thesis are *flux-type qubits* whose potential landscape and transition frequency depend on an externally applied flux bias and are typically operated near a well-defined symmetry point, commonly at half a flux quantum, $\Phi = \Phi_0/2 \equiv h/4e$. A circuit-level description and the corresponding flux-dependent potentials are introduced later in Sec. 3.4. Before turning to this specific implementation, the next section summarizes the dynamics of qubits, which apply across superconducting qubit modalities and directly underpin the spectroscopy and pulse experiments used throughout this thesis.

3.2 Theoretical basics of qubits

Having introduced superconducting qubits as anharmonic artificial atoms realized in Josephson circuits (Sec. 3.1), we now summarize the universal dynamics of qubits that are largely independent of the physical implementation. Specifically, we review the Bloch-sphere representation, driven Rabi oscillations, and coherence properties characterized by the relaxation and dephasing times T_1, T_2, and T_2^*. These concepts provide the basis for continuous-wave spectroscopy and time-domain measurements used throughout this work.

3.2.1 Qubit states and the Bloch-sphere representation

The qubit is the quantum analogue of a classical bit, but it can exist in a coherent superposition of two basis states, usually denoted by $|0\rangle$ and $|1\rangle$ within the Dirac bra–ket formalism [99, 100]. These states correspond to the eigenstates of the Pauli operator σ_z (acting on the qubit subspace) with eigenvalues ± 1. A general pure qubit state can be written as

$$|\psi\rangle = \alpha\,|0\rangle + \beta\,|1\rangle\,, \qquad |\alpha|^2 + |\beta|^2 = 1, \tag{3.5}$$

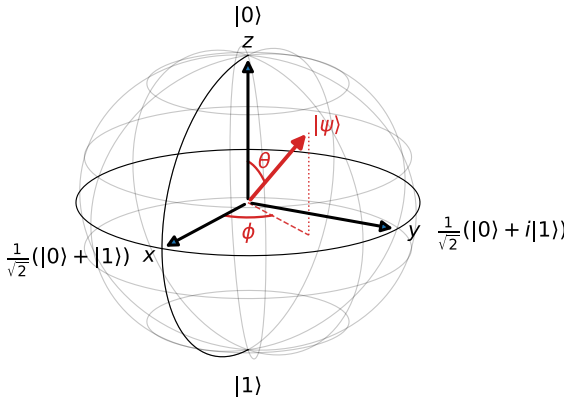

Figure 3.2: Bloch-sphere representation of a qubit state $|\psi\rangle$, characterized by the polar angle θ and the azimuthal angle ϕ. The sphere provides a geometric visualization of arbitrary pure states and single-qubit rotations.

where α and β are complex probability amplitudes. Since the global phase of $|\psi\rangle$ is not observable, the state can be parameterized by two real angles θ and ϕ as

$$|\psi\rangle = \cos\frac{\theta}{2}\,|0\rangle + e^{i\phi}\sin\frac{\theta}{2}\,|1\rangle\,. \tag{3.6}$$

This parameterization maps any pure qubit state onto a point on the surface of the Bloch sphere (Fig. 3.2), where θ and ϕ define the polar and azimuthal angles of the Bloch vector

$$\vec{r} = (\sin\theta\cos\phi,\ \sin\theta\sin\phi,\ \cos\theta). \tag{3.7}$$

In the absence of external driving fields, the qubit dynamics are governed by the Hamiltonian

$$H_0 = \frac{\hbar\omega_{01}}{2}\sigma_z, \tag{3.8}$$

where ω_{01} denotes the qubit transition frequency as defined in Eq. (3.1). This Hamiltonian causes the Bloch vector to precess around the z-axis at the frequency ω_{01} [84, 101, 102].

The Bloch-sphere representation also provides a convenient description of mixed states within the density-matrix formalism,

$$\rho = \frac{1}{2}\left(\mathbb{I} + \vec{r}\cdot\vec{\sigma}\right), \tag{3.9}$$

with $|\vec{r}| \leq 1$. Pure states lie on the surface of the sphere, while mixed states are represented by points inside.

Rotations of the Bloch vector correspond to unitary operations of the form

$$U(\hat{n}, \Theta) = \exp\left[-\frac{i}{2}\Theta(\hat{n} \cdot \vec{\sigma})\right], \tag{3.10}$$

describing a rotation by an angle Θ about the axis $\hat{n}$. In experiments with superconducting qubits, such rotations are realized by applying resonant microwave pulses that couple to transverse components of the qubit degree of freedom.

3.2.2 Qubit control and driven dynamics

Applying a near-resonant classical drive induces coherent transitions between the qubit states $|0\rangle$ and $|1\rangle$ and results in nutations of the Bloch vector about a transverse axis [84, 101–103]. A standard semiclassical description of a driven two-level system is given by the Hamiltonian

$$H = \frac{\hbar\omega_{01}}{2}\sigma_z + \hbar\Omega_\mathrm{d}\cos(\omega_\mathrm{d}t + \phi)\,\sigma_x, \tag{3.11}$$

where Ω_d denotes the drive amplitude, ω_d the drive frequency, and ϕ its phase. Here we chose a basis in which the drive couples transversely to the qubit degree of freedom. Transforming into a frame rotating at ω_d and applying the rotating-wave approximation yields [101, 102]

$$H_\mathrm{RWA} = \frac{\hbar\Delta}{2}\sigma_z + \frac{\hbar\Omega_\mathrm{R}}{2}\sigma_x, \qquad \Delta = \omega_{01} - \omega_\mathrm{d}, \tag{3.12}$$

where Ω_R is the on-resonance Rabi frequency determined by the transverse drive amplitude. Within this effective description, the Bloch vector undergoes a rotation about an axis in the x–z plane with angular velocity

$$\Omega = \sqrt{\Omega_\mathrm{R}^2 + \Delta^2}, \tag{3.13}$$

and a tilt angle θ relative to the z axis defined by $\cos\theta = \frac{\Delta}{\Omega}$.

Assuming the qubit is initially prepared in the ground state $|0\rangle$, the probability to find it in the excited state $|1\rangle$ after a drive pulse of duration t is

$$P_1(t) = \frac{\Omega_\mathrm{R}^2}{\Omega^2}\sin^2\left(\frac{\Omega t}{2}\right), \tag{3.14}$$

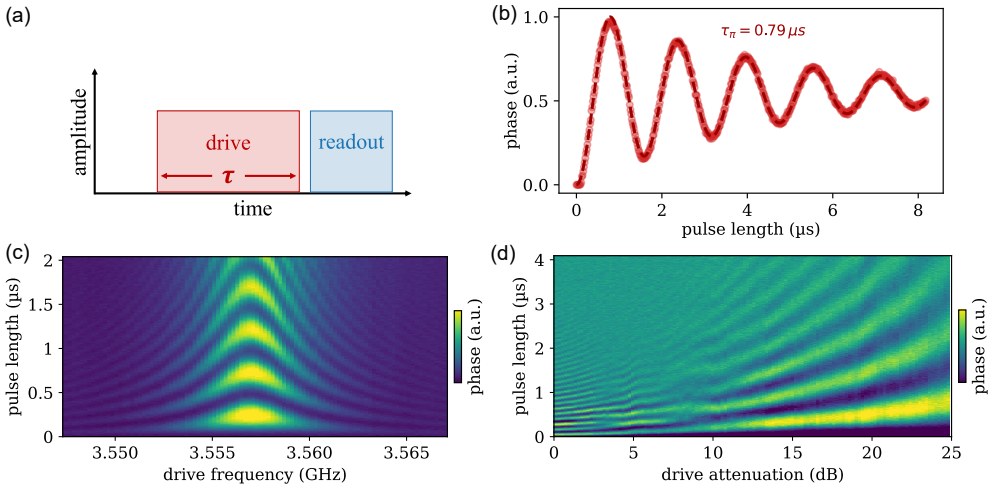

Figure 3.3: Representative Rabi experiments illustrating driven qubit dynamics. (a) Schematic pulse sequence (not to scale) consisting of a resonant drive pulse of variable duration τ, followed by a qubit readout pulse; both are implemented using microwave excitations. (b) Measured Rabi oscillations showing the excited-state population (arb. units) versus pulse duration; the π-pulse length τ_π is obtained from a damped-sinusoidal fit. (c) Chevron pattern measured by sweeping the drive frequency and pulse duration, identifying the resonant condition $\Delta = 0$ along the symmetry axis and yielding the Rabi frequency from the oscillation period. (d) Rabi oscillations versus drive power, demonstrating the dependence of the Rabi frequency on the applied microwave amplitude. All data shown are experimental measurements obtained on superconducting quarton qubits with stacked-junction array inductors.

which defines the characteristic *Rabi oscillations*. On resonance ($\Delta = 0$), the qubit undergoes full population inversion at a π pulse, $\Omega_R t = \pi$. For finite detuning, the oscillations occur at a higher angular frequency Ω and with reduced amplitude.

Figure 3.3 illustrates representative experimental manifestations of driven qubit dynamics. The pulse sequence in Fig. 3.3 (a) applies a drive pulse of variable duration, followed by a qubit readout pulse, both implemented using microwave excitations. The resulting oscillatory population dynamics are shown in Fig. 3.3 (b), from which the π-pulse duration τ_π can be determined. Figure 3.3 (c) displays the characteristic chevron pattern obtained by sweeping both drive frequency and pulse duration; its symmetry axis identifies the resonant condition $\Delta = 0$, while the oscillation period provides access to the Rabi frequency. The dependence of the Rabi oscillations on the applied drive power is shown in Fig. 3.3 (d).

Rabi oscillations constitute a central tool for qubit control, as they enable the calibration of the qubit transition frequency ω_{01}, the resonant drive frequency addressing the $|0\rangle \leftrightarrow |1\rangle$ transition, and the pulse duration τ_π required to implement

a π rotation, thereby defining the basic building blocks for controlled single-qubit operations [40, 84, 98].

Beyond pulsed control, *qubit spectroscopy* probes the frequency-domain response of the driven transition using a continuous-wave (CW) microwave tone [40, 84, 98]. In practice, the anharmonicity introduced in Sec. 3.1 ensures that a weak spectroscopy tone near ω_{01} predominantly addresses the $|0\rangle \leftrightarrow |1\rangle$ transition.

In this approach, the qubit is driven continuously near the expected transition frequency, $\omega_\mathrm{d} \approx \omega_{01}$, and the steady-state readout response is recorded as a function of drive frequency; in the weak-drive limit this yields a resonance feature (peak or dip, depending on the detection quadrature) centered at the qubit transition frequency ω_{01}.

Maintaining low drive power avoids strong power broadening and nonlinear response, such that the resonance position can be determined accurately [101, 102].

In superconducting circuits, spectroscopy is commonly implemented as a two-tone measurement: a first tone drives the qubit transition near ω_{01}, while a second microwave tone interrogates a coupled harmonic oscillator, typically a microwave readout resonator (see Sec. 3.5.3), whose response depends on the qubit state [40, 84, 98, 104]. When the qubit is excited by the spectroscopy tone, the readout signal changes, allowing one to detect at which drive frequency the qubit transition is resonantly driven. In the so-called dispersive regime, the qubit-state dependence of the resonator response is often described in terms of a *dispersive shift*, i.e., a qubit-state-dependent shift of the resonator frequency. The microscopic origin and quantitative description of this effect are discussed in Sec. 3.4.5.

A typical spectroscopy trace is obtained by recording the readout response versus the spectroscopy-drive frequency ω_d. From the resulting resonance feature the qubit transition frequency ω_{01} can be directly obtained. For many superconducting qubit designs, the transition frequency is not fixed but can be tuned by external control parameters (Sec. 3.1). In flux-type qubits, for example, ω_{01} depends on the magnetic flux threading the qubit circuit loop, which can be controlled by an applied magnetic field. By repeating the measurement while sweeping a tuning parameter—for instance the applied magnetic flux in a flux qubit—one obtains a spectroscopic map $\omega_{01}(\Phi)$, i.e., the qubit spectrum as a function of flux [40, 98]. This measurement principle is illustrated in Fig. 3.6 (right panel), where the readout signal is shown versus drive frequency and a resonance feature marks the qubit transition. As the qubit frequency is tuned, the resonance position shifts accordingly, tracing out the qubit spectrum (colormap in the center).

The concepts introduced in this section provide the framework for interpreting driven qubit dynamics in both the time domain (Rabi and related pulse experiments) and the frequency domain (continuous-wave spectroscopy), which are used throughout this thesis to characterize superconducting flux qubits operated in the quarton regime.

3.2.3 Qubit coherence and characteristic timescales

In real devices, coherent oscillations such as those in Fig. 3.3 (b) decay rather than persisting indefinitely, reflecting the coupling of the qubit to environmental degrees of freedom that lead to energy relaxation and loss of phase coherence [84, 98]. Microscopically, relaxation arises from energy exchange with the environment, whereas dephasing originates from fluctuations of the transition frequency $\omega_{01}(t)$.

Energy relaxation is quantified by the time constant T_1, which describes the decay of an initially excited qubit toward its ground state. From a quantum-optical perspective, this process corresponds to energy emission at the transition frequency ω_{01} into available bath modes and is governed by the density of environmental modes (weighted by their coupling strength) at that frequency. In the weak-coupling limit, Fermi's golden rule yields

$$\Gamma_1 = \frac{2\pi}{\hbar^2} \, |\langle 0|H_{\text{int}}|1\rangle|^2 \, \rho_{\text{env}}(\omega_{01}) = \frac{1}{T_1}, \tag{3.15}$$

where H_{int} describes the qubit–environment interaction and $\rho_{\text{env}}(\omega)$ is the density of environmental modes weighted by their coupling strength [84, 101, 102]. This emphasizes that not only electromagnetic modes but any other systems, e.g. other quantum two-level systems, with resonances near ω_{01} can act as a structured bath and thereby affect T_1—a perspective that will reappear in the discussion of loss channels to intrinsic two-level systems in materials of superconducting circuits in later chapters.

Experimentally, T_1 is measured with the pulse sequence schematically shown in Fig. 3.4 (a): a π pulse prepares the qubit in $|1\rangle$, followed by a free evolution of duration t after which the excited-state population is read out. The decay is well described by

$$P_1(t) = P_1(0) \, e^{-t/T_1}. \tag{3.16}$$

On the Bloch sphere, this corresponds to relaxation of the Bloch vector toward the north pole.

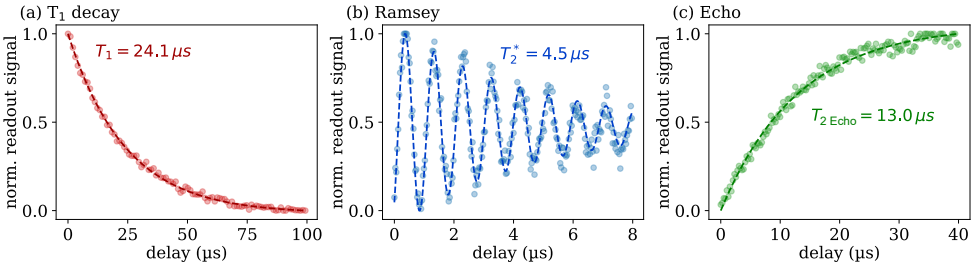

Figure 3.4: Time-domain coherence experiments. Representative averaged measurements of (a) energy relaxation (T_1), (b) Ramsey interference (T_2^*), and (c) Hahn echo ($T_{2\,\mathrm{Echo}}$) experiments with a quarton qubit with a stacked-junction array inductor. The normalized readout signal is shown together with fit functions used to extract the respective coherence times. These traces correspond to the statistical data summarized in Fig. 6.6 (c) and discussed in Sec. 6.4.

Dephasing without energy exchange, so-called pure dephasing with characteristic time T_φ, results from random fluctuations of $\omega_{01}(t)$ and causes decay of phase coherence for superposition states in the equatorial plane. The total decoherence time T_2 satisfies

$$\frac{1}{T_2} = \frac{1}{2T_1} + \frac{1}{T_\varphi}, \tag{3.17}$$

implying the bound $T_2 \leq 2T_1$ reached when pure dephasing is negligible [105]. In practice, superconducting qubits often do not reach this limit because frequency fluctuations introduce additional dephasing. This is particularly relevant for flux-type qubits, where $\omega_{01}(\Phi)$ is intentionally tuned by the applied flux and depends on the circuit potential landscape discussed later in Sec. 3.4 [38, 39, 106, 107].

While T_2 and T_φ provide a useful theoretical decomposition of decoherence, they are not directly accessible in a single experiment in superconducting qubits. Rather, they are inferred from a combination of relaxation and coherence measurements under specific noise models. Experimentally measured coherence times therefore depend on the applied pulse sequence and the noise spectrum probed. In particular, Ramsey and Hahn-echo experiments yield the characteristic times T_2^* and $T_{2\,\mathrm{Echo}}$, respectively, which reflect different sensitivities to low-frequency and quasi-static noise components.

Ramsey interferometry (Fig. 3.4 (b)) probes phase coherence in the time domain. Two $\pi/2$ pulses, separated by a free-evolution time τ, create and later project a superposition state. The drive pulses are typically applied with a small detuning $\Delta = \omega_{01} - \omega_\mathrm{d}$, such that during the free evolution the relative phase accumulates

at approximately Δ (in the rotating frame), producing interference fringes. A commonly used fit model is

$$s_{\mathrm{Ramsey}}(\tau) = A\cos(\Delta\tau + \phi_0)\, e^{-\tau/T_2^*}, \tag{3.18}$$

where A is a contrast factor and ϕ_0 is a phase offset set by pulse phases and timing. The decay time T_2^* is sensitive to quasi-static frequency fluctuations and inhomogeneous broadening [105].

Hahn-echo measurements (Fig. 3.4 (c)) constitute a distinct time-domain experiment designed to refocus phase evolution caused by slow frequency fluctuations. By inserting a refocusing π pulse halfway through the sequence, quasi-static noise contributions are suppressed, typically resulting in a longer coherence time $T_{2\,\mathrm{Echo}} > T_2^*$ [39, 105, 106]. Deviations from this trend can occur when the refocusing pulse introduces additional errors or when the dephasing noise is strongly non-Gaussian or non-stationary, effects that have been documented in particular for flux-type qubits [39].

The characteristic times T_1, T_2^*, and $T_{2\,\mathrm{Echo}}$ summarize key aspects of qubit coherence and provide a compact set of metrics for comparing device performance.

3.3 Noise and sources of decoherence

The coherent dynamics discussed above are ultimately limited by coupling to environmental degrees of freedom, which causes energy relaxation and dephasing. In flux-type circuits, fluctuations of the applied flux bias translate directly into frequency noise through the susceptibility $\partial\omega_{01}/\partial\Phi$ introduced in Eq. (3.4).

In the following, we review the dominant noise and loss channels relevant to superconducting flux qubits, with particular emphasis on the mechanisms most pertinent to quarton devices. For each noise source, we distinguish longitudinal coupling that leads to pure dephasing from transverse coupling that gives rise to energy relaxation. In the devices studied here, microscopic two-level systems in Josephson junctions and dielectrics, as well as low-frequency flux noise, provide the central physical framework for interpreting the measured coherence times (Sec. 3.2.3) and spectroscopic signatures (Sec. 3.2.2).

A general framework for describing decoherence is provided by the noise–susceptibility picture. If a circuit parameter λ fluctuates as $\lambda \to \lambda + \delta\lambda(t)$ with power spectral density (PSD) $S_\lambda(\omega)$, the resulting dephasing and relaxation rates are determined by the susceptibility of the qubit transition frequency ω_{01} to λ

and by the noise spectrum evaluated at the relevant frequencies. Low-frequency noise components ($\omega \to 0$) primarily contribute to pure dephasing, while noise at frequencies near the qubit transition ($\omega \approx \omega_{01}$) leads to energy relaxation [40].

Within a weak-coupling description, Fermi's golden rule relates the relaxation rate to the noise spectral density of the bath operator that couples to the qubit via $H_{\text{int}} = A\,X$:

$$\Gamma_1 = \frac{1}{\hbar^2}\,|\langle 0|A|1\rangle|^2\,S_X(\omega_{01}), \qquad \Gamma_\phi \propto \left(\frac{\partial\omega_{01}}{\partial\lambda}\right)^2 S_\lambda(\omega \to 0), \tag{3.19}$$

highlighting that different noise sources impose distinct coherence limits through both their spectral properties and the qubit's susceptibility. Here, $S_X(\omega)$ denotes the (one-sided) power spectral density of the bath fluctuations at frequency ω; $S_\lambda(\omega)$ is defined analogously for fluctuations of the parameter λ. With the one-sided convention used here, we absorb the convention-dependent 2π factor into the definition of the weighted mode density and use $S_X(\omega) = 2\pi\,\rho_{\text{env}}(\omega)$, such that Eq. (3.15) and the PSD form are consistent. Consequently, the dominant decoherence mechanism depends on the qubit transition frequency and on how sensitively ω_{01} responds to fluctuations of the relevant circuit parameters.

Strategies for mitigating decoherence therefore target either the noise source itself (by reducing $S_\lambda(\omega)$ through materials optimization, filtering, and shielding) or the device susceptibility, by engineering circuits whose transition frequencies are less sensitive to environmental fluctuations. In specific superconducting qubit implementations, these approaches can involve trade-offs, as reducing susceptibility to one noise channel may constrain tunability or control flexibility.

3.3.1 Two-level systems in Josephson junctions and dielectrics

Microscopic two-level systems (TLS) in amorphous oxides are a common coherence limit in superconducting quantum circuits and can contribute to both energy relaxation (T_1) and dephasing (T_2) [27, 28, 108, 109].

Across many qubit types, TLS-induced signatures appear both in spectroscopy and in time-domain coherence measurements. In spectroscopy, additional resonances become visible when the qubit transition is tuned through frequency and hybridizes with a TLS, producing a characteristic avoided level crossing [27, 28, 105, 110–112]. These resonances are typically only weakly affected by the qubit control parameters (e.g., magnetic flux in flux-type qubits), in contrast to the qubit transition itself. In the time domain, the same frequency intervals are frequently accompanied by pronounced reductions of T_1, consistent with an additional decay channel when the

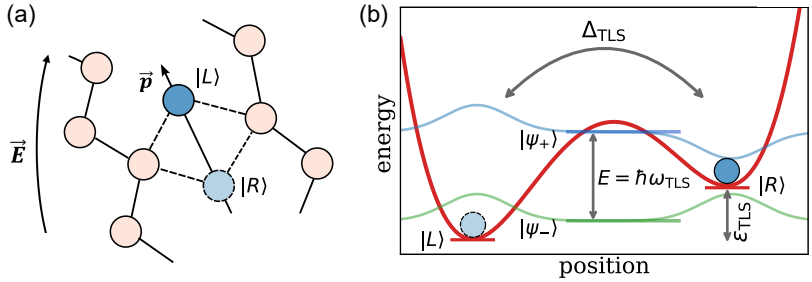

Figure 3.5: Standard tunneling model for two-level systems. (a) Example microscopic picture: a defect in an amorphous solid may occupy two nearby, meta-stable configurations. If the configurations differ in their charge distribution, the defect carries an electric dipole moment and can couple to the electric fields of superconducting qubits, for example the field across a Josephson junction barrier. (b) In the standard tunneling model, the defect is described by localized states $|L\rangle$ and $|R\rangle$ with asymmetry $\varepsilon_{\mathrm{TLS}}$ and tunneling amplitude Δ_{TLS}, yielding eigenstates $|\psi_\pm\rangle$ split by $\hbar\omega_{\mathrm{TLS}}$.

qubit is operated close to a TLS frequency [27, 28, 109]. Moreover, TLS frequencies and the apparent coupling features can drift slowly in time or change after thermal cycling, consistent with a microscopic origin rather than a fixed electromagnetic mode [27, 28, 113].

A consistent interpretation of these observations was proposed by Martinis *et al.*, who attributed both the frequency dependence of T_1 and the avoided level crossings to dielectric loss from microscopic defects in amorphous oxides associated with Josephson junction barriers [28]. As an example microscopic picture, one may consider a defect in the disordered oxide that occupies two nearby, meta-stable configurations (Fig. 3.5 (a)). At low temperatures, tunneling between these configurations yields an effective two-level degree of freedom. If the configurations differ in their local charge distribution, the defect carries an electric dipole moment and can couple to the electric field concentrated across a Josephson junction barrier [114].

The devices studied in this work use Josephson junctions with AlO_x tunnel barriers, making TLS in amorphous oxides a natural candidate to explain frequency-dependent relaxation and spectroscopic avoided level crossings observed later. In the following, we summarize the minimal TLS model and the resulting qubit–TLS interaction needed for this analysis.

Within the standard tunneling model (STM), a TLS is described by tunneling between two localized configurations $|L\rangle$ and $|R\rangle$ with energy asymmetry $\varepsilon_{\mathrm{TLS}}$ and

tunneling amplitude Δ_{TLS} as illustrated in Fig. 3.5 (b) [115, 116]. In the localized basis $\{|L\rangle, |R\rangle\}$, the TLS Hamiltonian reads

$$H_{\mathrm{TLS}} = \frac{1}{2}\,\varepsilon_{\mathrm{TLS}}\,\sigma_z + \frac{1}{2}\,\Delta_{\mathrm{TLS}}\,\sigma_x, \tag{3.20}$$

where $\sigma_{x,z}$ are Pauli matrices. The eigenenergies and the corresponding TLS transition frequency between the eigenstates $|\psi_{\pm}\rangle$ are

$$E_{\pm} = \pm\frac{1}{2}\sqrt{\varepsilon_{\mathrm{TLS}}^2 + \Delta_{\mathrm{TLS}}^2}, \qquad \hbar\omega_{\mathrm{TLS}} = \sqrt{\varepsilon_{\mathrm{TLS}}^2 + \Delta_{\mathrm{TLS}}^2}. \tag{3.21}$$

The TLS asymmetry depends on the local electric and strain fields,

$$\varepsilon_{\mathrm{TLS}} \to \varepsilon_{\mathrm{TLS}} + 2\,\vec{p}\cdot\vec{E} + 2\,\gamma S, \tag{3.22}$$

where $\vec{p}$ denotes the TLS electric dipole moment, $\vec{E}$ the local electric field, γ the deformation potential, and S an applied strain. Experiments that tune individual TLS by strain or DC electric fields directly confirm this coupling and enable extraction of TLS dipole moments [117–121].

In superconducting qubits, high local electric fields occur in capacitive elements, in particular across Josephson junction barriers. Thus, the same junction element that provides the nonlinearity enabling qubit operation (Sec. 3.1) can also host microscopic defects that limit coherence. A TLS located in such a region couples to the qubit degree of freedom via the electric-dipole interaction

$$H_{\mathrm{int}} = -\vec{p}\cdot\vec{E}, \tag{3.23}$$

where $\vec{E}$ is the qubit electric-field operator evaluated at the TLS position. In the TLS eigenbasis, this yields a transverse qubit–TLS coupling with strength [27, 109]

$$g = \frac{|\vec{p}|\,|\vec{E}_{\mathrm{rms}}|\cos\theta}{\hbar}\,\frac{\Delta_{\mathrm{TLS}}}{\omega_{\mathrm{TLS}}}, \tag{3.24}$$

with $\vec{E}_{\mathrm{rms}}$ the zero-point rms field amplitude associated with the qubit degree of freedom, and θ the orientation angle between dipole and field. The mixing factor $\Delta_{\mathrm{TLS}}/\omega_{\mathrm{TLS}}$ expresses that a strongly asymmetric TLS couples weakly in the eigenbasis.

For typical dipole moments $|\vec{p}| \sim (0.1\text{–}1)\,\mathrm{e\AA}$ in amorphous oxides of AlO_x tunnel barriers and junction-scale zero-point fields, couplings range from sub-MHz up to $\mathcal{O}(10\text{–}100)\,\mathrm{MHz}$, depending on dipole orientation and electric-field participation [28, 109, 120–122].

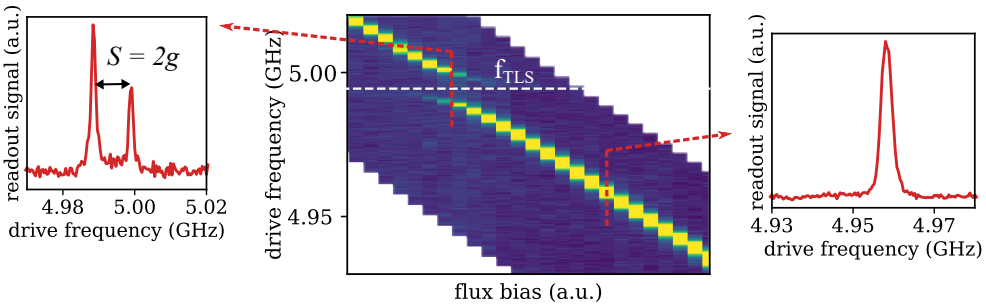

Figure 3.6: TLS spectroscopy and avoided level crossings. Spectroscopy of a quarton qubit measured by sweeping a weak microwave drive tone and recording the dispersive readout-resonator response. *Right:* at fixed flux, the qubit transition appears as a resonance feature (dip or peak) in the measured readout signal at the bare transition frequency ω_{01}. *Center:* repeating the measurement while sweeping the applied magnetic flux yields a spectroscopic map $\omega_{01}(\Phi)$. *Left:* when the qubit is tuned into resonance with an individual TLS, the hybridized eigenstates form an avoided crossing with splitting $S = 2g$. The data corresponds to Fig. 6.13 discussed in Sec. 6.6.1.

When the qubit transition frequency approaches the TLS frequency, $\omega_{01} \approx \omega_{\mathrm{TLS}}$, the two systems hybridize and can be described by a Jaynes–Cummings-like model for two coupled two-level systems,

$$H = \frac{\hbar\omega_{01}}{2}\,\tau_z + \frac{\hbar\omega_{\mathrm{TLS}}}{2}\,\sigma_z + \hbar g\,(\tau_+\sigma_- + \tau_-\sigma_+)\,, \tag{3.25}$$

where $\tau_{x,y,z}$ ($\sigma_{x,y,z}$) are Pauli operators acting on the qubit (TLS) subspace, and $\tau_\pm = (\tau_x \pm i\tau_y)/2$ and $\sigma_\pm = (\sigma_x \pm i\sigma_y)/2$ are the corresponding raising and lowering operators. Diagonalizing Eq. (3.25) yields the eigenenergies

$$E_\pm \;=\; \tfrac{\hbar}{2}(\omega_{01} + \omega_{\mathrm{TLS}}) \;\pm\; \hbar\sqrt{g^2 + (\Delta/2)^2}, \qquad \Delta = \omega_{01} - \omega_{\mathrm{TLS}}. \tag{3.26}$$

In spectroscopy, the hybridization appears as an avoided level crossing with splitting $S = 2g$ at resonance (see Fig. 3.6) [27, 28]. Importantly, the same resonances can also increase energy relaxation: bringing the qubit frequency close to a TLS frequency opens an additional decay channel and T_1 is frequently reduced in the same frequency interval where the avoided level crossing is observed [27, 28, 109].

On a coarse-grained level, an ensemble of TLS with a broad distribution of transition frequencies acts as a dissipative dielectric environment and contributes to energy relaxation predominantly through off-resonant coupling. In this picture, TLS-induced dissipation is parametrized by an effective loss tangent $\tan\delta$. Within the STM, an approximately energy-independent density of TLS states per unit energy, D_0, yields the standard relation for the energy-relaxation rate [27, 28, 109]

$$\Gamma_1(\omega_{01}) \equiv \frac{1}{T_1} \;\approx\; \omega_{01}\,\tan\delta_{\mathrm{bg}}, \qquad \tan\delta_{\mathrm{bg}} \;=\; \frac{\pi D_0 p^2}{3\,\varepsilon_r}, \tag{3.27}$$

where p denotes a typical TLS dipole magnitude and ε_r the relative permittivity. Equation (3.27) captures the smooth background loss expected from a dense ensemble of far-detuned defects. Resolved TLS, in contrast, produce sharp, frequency-local enhancements of Γ_1 when the qubit is tuned close to resonance. To connect such resolved avoided level crossings to the corresponding variations of T_1, it is useful to express the decay rate as a sum over individual defects.

For TLS labeled by j with transition frequency $\omega_{\mathrm{TLS},j}$, detuning $\Delta_j = \omega_{01} - \omega_{\mathrm{TLS},j}$, and coupling g_j (Eq. (3.24)), Fermi's golden rule yields the interpolating form [27, 28, 109]

$$\Gamma_1(\omega_{01}) \;=\; \sum_j \frac{2g_j^2 \Gamma_{1,j}}{\Delta_j^2 + \Gamma_{2,j}^2} \;+\; \omega_{01} \tan\delta_{\mathrm{bg}}, \tag{3.28}$$

where $\Gamma_{1,j}$ and $\Gamma_{2,j}$ denote the relaxation and transverse decoherence rates of TLS j, respectively (with $\Gamma_{2,j} = \Gamma_{1,j}/2 + \Gamma_{\varphi,j}$). The first term yields Lorentzian enhancements of Γ_1 whenever the qubit is tuned close to an individual TLS, while the second term represents a smooth, off-resonant background. Equation (3.28) thus makes explicit why pronounced T_1 variations coincide with avoided crossings.

TLS parameters are not strictly static. Interactions within the disordered defect environment can lead to slow fluctuations of TLS transition frequencies and effective couplings, commonly referred to as spectral diffusion [27, 113, 123, 124]. As a consequence, avoided-crossing positions can drift over time and T_1 at a fixed operating point can fluctuate. Such non-stationary loss directly degrades T_2: time-dependent Γ_1 produces additional dephasing (sometimes termed "T_1-noise-induced dephasing") and can lead to fluctuations of the measured Ramsey decay.

Beyond identifying individual TLS, spectroscopy provides access to the statistical distribution of qubit–TLS couplings. Within the STM, TLS dipoles are randomly oriented in the amorphous dielectric. For a given local field amplitude E_{rms}, Eq. (3.24) implies the scaling [28, 114]

$$g \;\propto\; p\, E_{\mathrm{rms}} \cos\theta, \tag{3.29}$$

with random orientation angle θ. This leads to a broad distribution of observable splittings $S = 2g$ and an approximately logarithmic growth of the cumulative number of resolved avoided level crossings that appear in the spectrum [27, 28].

A compact STM-based expression for the number density of avoided crossings per TLS energy E and coupling strength g reads [27, 28]

$$\frac{\partial^2 N_{\mathrm{TLS}}}{\partial E\, \partial g} \;=\; \sigma A\, \frac{\sqrt{1 - g^2/g_{\max}^2}}{2g}, \qquad 0 < g \le g_{\max}, \tag{3.30}$$

where A is the junction area and σ is a material-specific defect density per energy and area, while $g_{\max}$ is the maximal coupling strength set by the largest effective dipole moment and maximal field participation.

To obtain the cumulative number of splittings in an energy window ΔE, one integrates Eq. (3.30) over coupling,

$$N_{\mathrm{TLS}}(g_{\mathrm{res}} \le g \le g_0; \Delta E) = \int_{\Delta E} \mathrm{d}E \int_{g_{\mathrm{res}}}^{g_0} \mathrm{d}g \, \frac{\partial^2 N_{\mathrm{TLS}}}{\partial E \, \partial g}, \tag{3.31}$$

where g_{res} is a lower cutoff set by the finite experimental resolution. Equivalently, in terms of splittings $S = 2g$, the lower cutoff is $S_{\mathrm{res}} = 2g_{\mathrm{res}}$: splittings below S_{res} are not reliably detected and therefore do not enter the count.

The integral in Eq. (3.31) can be evaluated analytically, where the exact primitive contains a logarithmic term plus additional contributions that vary slowly for $g \ll g_{\max}$ (Appendix A). In the experimentally relevant regime $g \ll g_{\max}$, Eq. (3.30) simplifies to $\partial^2 N/(\partial E \, \partial g) \approx (\sigma A)/(2g)$. Inserting this limit into the cumulative definition in Eq. (3.31) yields the logarithmic count:

$$N_{\mathrm{TLS}}(S_{\mathrm{res}} \le S \le S_0; \Delta E) \;\approx\; \Delta E \, \sigma A \, \frac{1}{2} \ln\!\left(\frac{S_0}{S_{\mathrm{res}}}\right), \qquad (S = 2g). \tag{3.32}$$

For comparison across devices, it is convenient to express the result in terms of a *spectral TLS density* in units of "TLS per GHz" in ordinary frequency $f = \omega/2\pi$ (not angular frequency). In this work we define ρ_{TLS} as the number of TLS per GHz associated with a *specific junction of area* A_{J} (i.e., ρ_{TLS} includes the junction area and is therefore specific to a junction of size A_{J}):

$$\rho_{\mathrm{TLS}} \equiv \sigma A_{\mathrm{J}}, \qquad [\rho_{\mathrm{TLS}}] = \mathrm{TLS/GHz}. \tag{3.33}$$

Using $\Delta E = h \, \Delta f$ with Δf expressed in GHz and taking $A = A_{\mathrm{J}}$ for a single junction then yields

$$N_{\mathrm{TLS}}(S_{\mathrm{res}} \le S \le S_0; \Delta f) \;\approx\; \Delta f \, \rho_{\mathrm{TLS}} \, \frac{1}{2} \ln\!\left(\frac{S_0}{S_{\mathrm{res}}}\right). \tag{3.34}$$

The prefactor $1/2$ here follows the convention in Eq. (3.30); if alternative definitions of g or of the coupling distribution are used, this prefactor can be absorbed into the definition of ρ_{TLS}, while the logarithmic dependence on the ratio S_0/S_{res} remains the robust signature.

In the literature, the area-normalized defect density σ (often quoted as "TLS per GHz per $\mu\mathrm{m}^2$") is frequently used and offers a convenient comparison independent of junction area. The relation to the spectral density used here is simply $\rho_{\mathrm{TLS}} = \sigma A_{\mathrm{J}}$. In later chapters, we use Eqs. (3.32)–(3.34) to extract ρ_{TLS} (and thus σ) from cumulative splitting counts and to relate the result to junction geometry and oxide volume in stacked-junction circuits.

3.3.2 Flux noise and low-frequency magnetic fluctuations

Low-frequency magnetic flux noise constitutes a prominent source of dephasing in superconducting flux-type qubits. As discussed in Sec. 3.1, the transition frequency of these circuits depends explicitly on the magnetic flux threading a superconducting loop. Consequently, stochastic fluctuations of the effective flux bias directly translate into fluctuations of the qubit transition frequency through the susceptibility $\partial\omega_{01}/\partial\Phi$ introduced in Eq. (3.4).

A wide range of experiments on flux qubits and SQUID-based circuits have established that magnetic flux noise exhibits an approximately universal $1/f^{\alpha}$ power spectral density over many decades in frequency [38, 39],

$$S_{\Phi}(\omega) = A_{\Phi}^{2}\left(\frac{2\pi\cdot 1\,\mathrm{Hz}}{\omega}\right)^{\gamma_{\Phi}}, \qquad \gamma_{\Phi}\approx 0.8\text{–}1.0, \tag{3.35}$$

with a characteristic amplitude A_{Φ} typically on the order of $1\,\mu\Phi_0/\sqrt{\mathrm{Hz}}$ at 1 Hz. Remarkably, both the spectral form and the typical magnitude of this noise appear largely independent of device geometry and material system across a wide range of superconducting circuits, suggesting a common microscopic origin [38–40].

Substantial experimental evidence implicates dilute paramagnetic surface spins as a dominant source of low-frequency flux noise. Early experiments on SQUIDs and flux qubits identified correlations between flux noise and trapped vortices as well as thermally polarizing surface spins [125]. More recently, on-chip electron-spin-resonance experiments have directly detected and quantified dilute paramagnetic spins on Al_2O_3 surfaces, providing strong microscopic support for this interpretation [126]. These spins generate fluctuating magnetic fields that couple inductively to superconducting loops and produce the observed $1/f$ flux noise spectrum. While the microscopic dynamics of these spins remain an active topic of research, their phenomenological impact on qubit coherence is well established.

Flux noise enters the qubit Hamiltonian through fluctuations of the applied flux bias, $\Phi \to \Phi + \delta\Phi(t)$, which induce transition-frequency fluctuations

$$\delta\omega_{01}(t) \;\approx\; \left(\frac{\partial\omega_{01}}{\partial\Phi}\right)\delta\Phi(t) + \frac{1}{2}\left(\frac{\partial^{2}\omega_{01}}{\partial\Phi^{2}}\right)\delta\Phi(t)^{2} + \ldots. \tag{3.36}$$

At most flux-bias points, the linear term dominates and gives rise to longitudinal noise, which primarily causes pure dephasing. Only at special symmetry points of the circuit potential, where $\partial\omega_{01}/\partial\Phi = 0$, first-order sensitivity to flux noise is suppressed and dephasing is governed by the curvature term. Such first-order "flux sweet spots" therefore play a central role in mitigating flux-noise-induced decoherence in flux-type qubits [2, 4, 38, 39].

Within the noise–susceptibility framework introduced in Sec. 3.3, the impact of flux noise on coherence depends not only on the noise amplitude but also on the specific measurement protocol. Ramsey interferometry is sensitive to quasi-static and very low-frequency noise components and therefore yields the characteristic time T_2^* (Sec. 3.2.3). For $1/f$-type flux noise and operation away from a sweet spot, the resulting Ramsey decay envelope takes the form [40]

$$\langle \sigma_+(t) \rangle \propto \exp\left[-\tfrac{1}{2} \left(\frac{\partial \omega_{01}}{\partial \Phi} \right)^2 A_\Phi^2 \ln(\omega_\mathrm{h} t)\, t^2 \right], \tag{3.37}$$

where ω_h is an effective high-frequency cutoff determined by filtering and experimental timescales. The logarithmic factor reflects the integration of the $1/\omega^{\gamma_\Phi \approx 1}$ spectrum over the relevant frequency band.

Echo-type pulse sequences partially refocus slow flux fluctuations and suppress the contribution of the lowest-frequency noise components, usually leading to an extended coherence time $T_{2\,\mathrm{Echo}} > T_2^*$ [39, 105].

Flux noise illustrates a fundamental trade-off in the design of superconducting flux qubits. On the one hand, flux tunability enables in-situ control of qubit frequencies, the realization of tunable couplers, and flexible frequency allocation in multi-qubit processors [34, 84, 98] On the other hand, the same tunability introduces sensitivity to magnetic fluctuations that can limit coherence away from symmetry points. Different circuit architectures balance this trade-off in distinct ways [2].

The quarton devices investigated in this thesis are flux-type qubits whose transition frequencies and anharmonicities depend on an externally applied magnetic flux and are typically operated at a symmetry point, $\Phi = \Phi_0/2$. Flux noise therefore represents an inherent aspect of the operating environment of these devices.

3.3.3 Other noise sources

Beyond two-level systems and low-frequency flux noise, several additional noise sources can contribute to decoherence in superconducting qubits. In this section, they are briefly summarized for completeness.

Fluctuations of electric charges in the qubit environment lead to temporal variations of the electrostatic potentials of superconducting islands and thereby modulate the effective charging energies E_C. Since the qubit frequency ω_{01} depends on both E_J and E_C (Sec. 3.1), such charge fluctuations translate into qubit frequency noise. Charge noise in superconducting circuits is commonly characterized by an approximately $1/f$ power spectral density over many decades in frequency [39,

105]. Historically, charge noise constituted a major decoherence mechanism in early Cooper-pair box devices [57, 127]. The introduction of large shunt capacitances, most prominently in the transmon qubit, strongly suppresses charge dispersion by increasing the ratio E_J/E_C and thereby exponentially reduces charge-noise-induced dephasing (in the transmon analysis the charge dispersion decreases as $\propto \exp\left[-\sqrt{8E_J/E_C}\right]$) [82, 128]. Flux-type qubits with sufficiently large effective capacitance similarly exhibit a strongly reduced sensitivity to charge fluctuations [2]. The devices studied in this thesis typically realize $E_J/E_C \sim 10$, placing them in a regime where this exponential suppression is already significant [40].

Temporal fluctuations of the critical current in Josephson junctions lead to fluctuations of the Josephson energy E_J and thus to variations of the qubit Hamiltonian. Critical-current noise is commonly attributed to microscopic defects in the tunnel barrier and is often observed to follow a $1/f$ spectrum [129, 130]. In flux-type qubits, such fluctuations can modulate both the effective inductance of junction arrays and the properties of the small-junction, resulting in qubit frequency noise proportional to $\partial\omega_{01}/\partial E_J$. In practice, this contribution is frequently difficult to distinguish experimentally from other low-frequency noise sources and is typically smaller than the effects of flux noise or TLS-induced decoherence [105, 129].

Residual non-equilibrium quasiparticles in superconducting films (Sec. 2.2.3) provide an additional relaxation channel for superconducting qubits and can limit the energy relaxation time T_1 [131, 132]. Their presence may arise from stray infrared radiation, cosmic rays, or imperfect thermalization, such that quasiparticle-induced decay depends sensitively on device design as well as on shielding and filtering in the experimental setup.

Residual photons in readout resonators or control lines (Sec. 3.5) can induce dephasing through fluctuations of the ac Stark shift in the dispersive regime [133, 134]. Such photon shot noise is mitigated by operating the readout resonators at low average photon number, employing strong attenuation and filtering at cryogenic stages, and carefully engineering the microwave environment.

3.4 The flux qubit

Superconducting flux qubits are artificial atoms whose dynamics are governed by the interplay of Josephson tunnelling, capacitive charging, and magnetic flux quantization in a closed superconducting loop. They are realized by interrupting a superconducting ring with one or several Josephson junctions, giving rise to a potential landscape that can be tuned in situ by an external magnetic flux Φ_{ext}.

Flux qubits operate in the phase-dominated regime $E_J \gg E_C$, where the superconducting junction phase is a well-defined quantum variable conjugate to charge. This distinguishes them from charge-type qubits such as the Cooper-pair box or the transmon, which operate either in the charge-dominated regime $E_C \gg E_J$ or suppress charge dispersion exponentially by increasing E_J/E_C through a large shunt capacitance [57, 82]. In contrast to transmons, flux-type qubits are encoded in flux (or phase) degrees of freedom and exhibit energy levels that depend periodically on Φ_{ext}. They allow tunability over wide frequency ranges and can reach very long coherence times when designed with large inductances and weak flux sensitivity [3, 39].

Historically, the concept originated from the persistent-current qubit introduced by Orlando *et al.* [135], where two potential wells correspond to clockwise and counterclockwise circulating supercurrents. Later implementations such as the fluxonium qubit [2] achieved greatly enhanced lifetimes by inserting long Josephson junction chains as superinductors. The capacitively shunted flux qubit (CSFQ) [16] further reduced charge sensitivity by adding a large shunt capacitance, similar in spirit to the transmon. The *quarton* qubit studied in this thesis is a flux-type qubit whose conceptual design combines large anharmonicity with reduced susceptibility to charge and flux noise, while enabling compact circuit layouts with only a small number of junctions ($N \sim 10$) [4, 34].

In the following, we first derive the general Hamiltonian of a flux qubit based on a Josephson junction array inductance, then introduce the single-mode approximation and discuss the characteristic parameter regimes. After discussing how the model can be extended to include non-uniform capacitances and parasitic ground coupling, the quarton regime is introduced. Finally, the model is connected to the Jaynes–Cummings Hamiltonian, extending the description to qubit–resonator interaction and dispersive readout.

3.4.1 Derivation of the flux-qubit Hamiltonian

The generic circuit of a flux qubit is shown in Fig. 3.7. It consists of a superconducting loop interrupted by $(N+1)$ Josephson junctions and shunted by a capacitance C_{sh}. One junction (index 0) acts as the small qubit junction (in this work called the small-junction) with Josephson energy E_J and capacitance C_J, while the remaining N junctions form a homogeneous array with Josephson energy E_{JA} and capacitance C_{JA} each. The gauge-invariant phase differences across the array

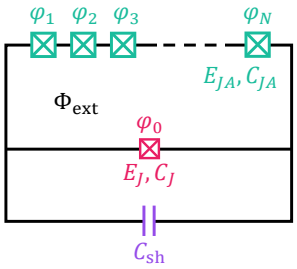

Figure 3.7: Schematic of a flux-qubit circuit Superconducting loop consisting of a small Josephson junction (E_J, C_J) in parallel with an array of N larger junctions (E_JA, C_JA) forming a superconducting loop threaded by an external magnetic flux Φ_ext. The loop is shunted by a capacitance C_sh. Phase differences $\phi_0 \dots \phi_N$ denote the gauge-invariant superconducting phases across each junction.

junctions are denoted φ_j ($j = 1 \dots N$). The externally applied magnetic flux Φ_ext enters via the fluxoid quantization condition (see Sec. 2.1.3)

$$\varphi_0 + \sum_{j=1}^{N} \varphi_j + \varphi_\text{ext} = 2\pi z, \qquad \varphi_\text{ext} = 2\pi \frac{\Phi_\text{ext}}{\Phi_0}, \tag{3.38}$$

where $\Phi_0 = h/2e$ is the flux quantum and $z \in \mathbb{Z}$.

The full Lagrangian following the notation of Catelani *et al.* [132] reads

$$\begin{aligned}\mathcal{L} = \frac{1}{2(2e)^2}\left[C_\text{sh}\left(\sum_{j=1}^{N}\dot{\varphi}_j\right)^2 + C_\text{J}\dot{\varphi}_0^2 + C_\text{JA}\sum_{j=1}^{N}\dot{\varphi}_j^2\right] \\ + E_\text{J}\cos\varphi_0 + E_\text{JA}\sum_{j=1}^{N}\cos\varphi_j,\end{aligned} \tag{3.39}$$

where the first term represents the kinetic energy due to the junction capacitances and the last two terms the Josephson potential of the loop (neglecting any geometric loop inductance, which is typically much smaller than the Josephson inductive energy). Eliminating the degree of freedom φ_0 via the fluxoid constraint $\varphi_0 = -\sum_{j=1}^{N}\varphi_j - \varphi_\text{ext}$ yields

$$\begin{aligned}\mathcal{L} = \frac{1}{2(2e)^2}\left[(C_\text{sh}+C_\text{J})\left(\sum_{j=1}^{N}\dot{\varphi}_j\right)^2 + C_\text{JA}\sum_{j=1}^{N}\dot{\varphi}_j^2\right] \\ + E_\text{J}\cos\left(\sum_{j=1}^{N}\varphi_j + \varphi_\text{ext}\right) + E_\text{JA}\sum_{j=1}^{N}\cos\varphi_j.\end{aligned} \tag{3.40}$$

The system possesses N dynamical degrees of freedom $\{\varphi_j\}$. To capture the collective flux dynamics, it is convenient to introduce the total phase drop across the array (which is equal to the phase drop across the small-junction by the fluxoid quantization condition),

$$\phi = \sum_{j=1}^{N} \varphi_j, \tag{3.41}$$

which acts as the generalized coordinate of the loop, and $N-1$ orthogonal difference coordinates ξ_k satisfying $\sum_j \xi_k^{(j)} = 0$ (for details, see Ref. [132]). For a homogeneous array ($E_{\mathrm{JA},j} = E_{\mathrm{JA}}$, $C_{\mathrm{JA},j} = C_{\mathrm{JA}}$), this transformation diagonalizes the kinetic term [41, 132, 136]. The Lagrangian then separates into a collective "qubit mode" and $N-1$ internal plasma modes, which are typically of higher energy:

$$\begin{aligned}\mathcal{L} = {} & \frac{1}{2(2e)^2}\left[C_\Sigma \dot{\phi}^2 + C_{\mathrm{JA}} \sum_{k=1}^{N-1} \dot{\xi}_k^2\right] \\ & + E_{\mathrm{J}} \cos(\phi + \varphi_{\mathrm{ext}}) + N\, E_{\mathrm{JA}} \cos\left(\frac{\phi}{N}\right) + \mathcal{L}_{\mathrm{plasma}}(\phi, \{\xi_k\}),\end{aligned} \tag{3.42}$$

with effective capacitance $C_\Sigma = C_{\mathrm{sh}} + C_{\mathrm{J}} + C_{\mathrm{JA}}/N$ and weak coupling terms between ϕ and ξ_k collected in $\mathcal{L}_{\mathrm{plasma}}$. A Legendre transformation gives the Hamiltonian

$$\begin{aligned}H = {} & 4E_{\mathrm{C}} n^2 + \sum_{k=1}^{N-1} 4E_{C,\mathrm{JA}} n_k^2 \\ & - E_{\mathrm{J}} \cos(\phi + \varphi_{\mathrm{ext}}) - N\, E_{\mathrm{JA}} \cos\left(\frac{\phi}{N}\right) + H_{\mathrm{plasma}}(\phi, \{\xi_k\}),\end{aligned} \tag{3.43}$$

where $E_{\mathrm{C}} = e^2/(2C_\Sigma)$ is the charging energy of the collective mode, $E_{C,\mathrm{JA}} = e^2/(2C_{\mathrm{JA}})$ that of the individual array junctions, and the operators $\partial\mathcal{L}/\partial\dot{\phi} = n$ and $\partial\mathcal{L}/\partial\dot{\phi}_k = n_k$ are conjugate to ϕ and ξ_k, respectively. Equation (3.43) represents the full multi-junction flux-loop Hamiltonian before any approximation. It assumes only a homogeneous array; extensions to inhomogeneous capacitance in the array are discussed later in Sec. 3.4.3.

3.4.2 Single-mode approximation and effective regimes

For large arrays ($N \gg 1$) with small phase drops across individual junctions ($|\varphi_j| \ll 1$ or equivalently $|\phi| \ll 2\pi N$ near the symmetry point) and $E_{C,\mathrm{JA}} \ll E_{\mathrm{JA}}$, the internal plasma modes oscillate at high frequencies

$$\omega_k \simeq \sqrt{8E_{\mathrm{JA}} E_{C,\mathrm{JA}}}/\hbar, \tag{3.44}$$

which correspond to the small-signal plasma frequency of a Josephson element (see Eq. (2.44)), identical to that obtained for a single junction in the RCSJ model (Sec. 2.2.5) and widely used in fluxonium-type circuits [41, 136]. For typical array junction parameters in this thesis ($L_J \sim 1\,\mathrm{nH}$, $C_J \sim 50$–$200\,\mathrm{fF}$), the corresponding plasma frequencies are about 15–30 GHz, while ω_{01} are about 3–5 GHz at the qubit operating point. This large difference in excitation frequencies justifies the single-mode approximation, in which the internal coordinates ξ_k remain near equilibrium.

Expanding the potential to quadratic order in ξ_k and keeping the full cosine dependence in ϕ yields the factorized Hamiltonian

$$H \simeq H_\phi + \sum_{k=1}^{N-1} H_k, \qquad H_\phi = 4E_C n^2 - E_J \cos(\phi + \varphi_{\mathrm{ext}}) - N E_{JA} \cos\left(\frac{\phi}{N}\right), \quad (3.45)$$

with $H_k = 4E_{C,JA} n_k^2 + \frac{1}{2} E_{JA} \xi_k^2$ describing harmonic plasma oscillations (H_k is omitted in the following). The low-energy dynamics are thus captured by the *one-dimensional* Hamiltonian H_ϕ, while residual mode couplings are of higher order $\mathcal{O}(\xi_k^2 \phi^2 / N^2)$ and negligible in the experimentally relevant parameter range. H_ϕ describes a collective mode of a flux qubit with a junction-array inductive shunt.

At the bias $\varphi_{\mathrm{ext}} = \pi$ (corresponding to $\Phi_{\mathrm{ext}} = \Phi_0/2$) the potential forms minima, at which the qubit is first-order insensitive to flux fluctuations [4]. Expanding the potential for $\varphi_{\mathrm{ext}} = \pi$ gives

$$U(\phi) = E_J[1 - \cos(\phi + \pi)] + N\, E_{JA}[1 - \cos(\tfrac{\phi}{N})], \quad (3.46)$$

and using $\cos(\phi/N) \approx 1 - \phi^2/(2N^2) + \phi^4/(24N^4)$ gives

$$U(\phi) \simeq E_J \left[\frac{1}{2}\Big(\frac{\gamma}{N} - 1\Big)\phi^2 + \frac{1}{24}\Big(1 - \frac{\gamma}{N^3}\Big)\phi^4\right], \quad \gamma = \frac{E_{JA}}{E_J}. \quad (3.47)$$

Depending on γ/N, three regimes arise [4, 41]:

(i) the *fluxon* regime ($\gamma/N < 1$) with a double-well potential as in the conventional persistent-current qubit [1, 135]. The fluxonium qubit extends this case to $\gamma/N \ll 1$ with long arrays of $N \sim 100$ [2],

(ii) the *plasmon* regime ($\gamma/N > 1$) with a nearly harmonic potential resembling a transmon or CSFQ [16, 82], and

(iii) the *quarton* regime ($\gamma/N = 1$) where the quadratic term cancels and the potential is purely quartic.

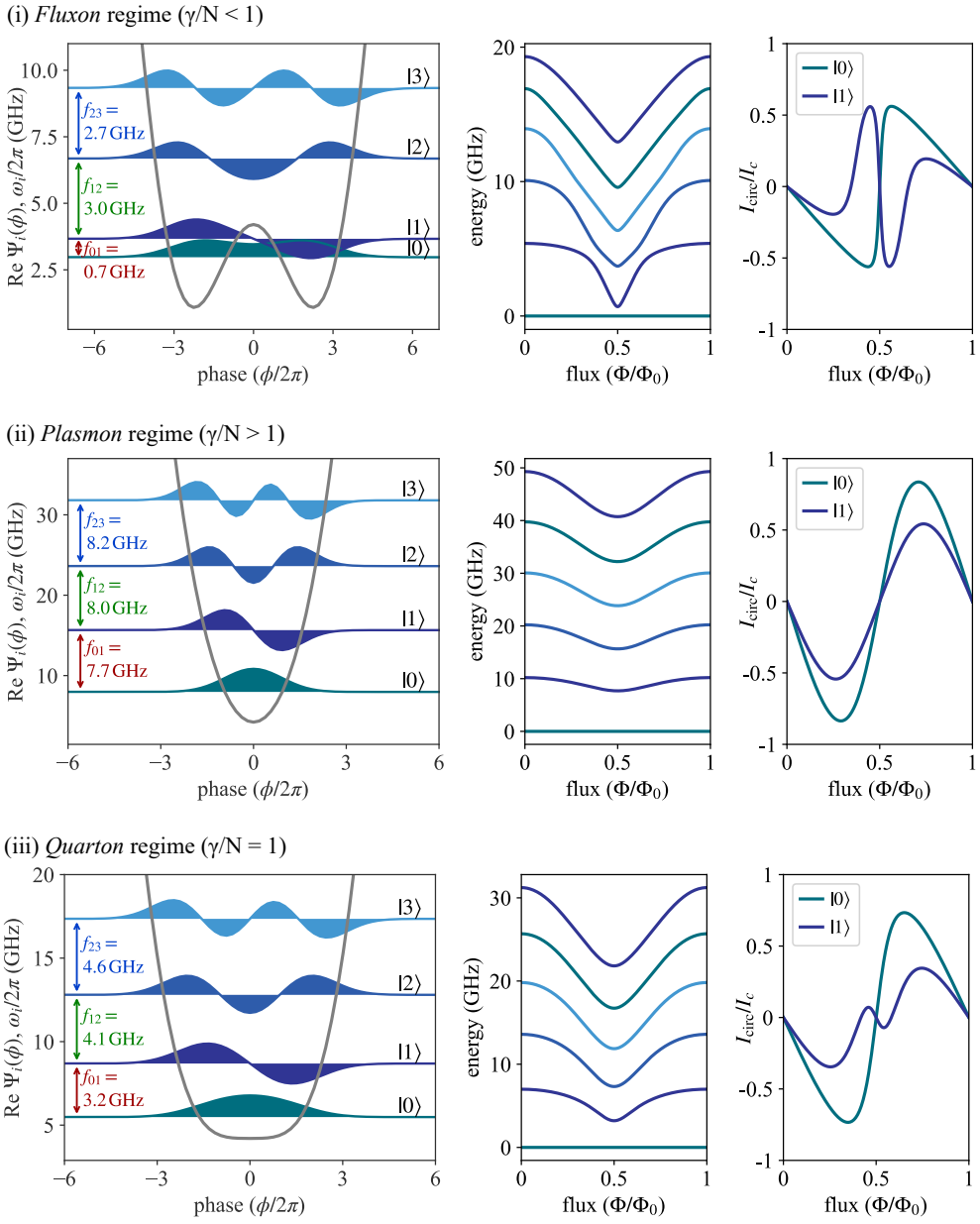

Figure 3.8: Flux-qubit potentials, eigenstates, spectra, and circulating currents in three characteristic regimes. Left: Potential $U(\varphi)$ and the lowest four wavefunctions at $\Phi_{\text{ext}} = \Phi_0/2$, illustrating the transition from a double-well (fluxon) to harmonic (plasmon) and nearly quartic (quarton) confinement. **Middle:** Energy levels $E_n(\Phi_{\text{ext}})$ versus flux bias. **Right:** Circulating currents $I(\Phi_{\text{ext}})$ of the lowest states. Each row corresponds to one parameter regime of Eq. (3.48) calculated with $\gamma/N = E_{\text{L}}/E_{\text{J}} =$ (i) 0.35, (ii) 3.0, and (iii) 1.0.

A combined visualization of the potentials, eigenstates, energy levels, and circulating currents in the three regimes is shown in Fig. 3.8. For $\gamma/N < 1$ the potential exhibits two minima separated by a barrier. As γ/N approaches unity, the barrier flattens and the potential is quartic near its minimum. At $\gamma/N > 1$ quadratic contributions reduce anharmonicity and increase the qubit frequency [4].

In the limit where the phase drop across each junction of the array remains small, $\phi/N \ll 1$, the cosine potential of the array can be expanded as $\cos(\phi/N) \approx 1 - \phi^2/(2N^2)$. This approximation is valid whenever the total phase ϕ distributes over many array junctions such that each individual junction experiences only a small phase drop, in particular, the array behaves as a nearly linear superinductance with an effective inductive energy $E_\mathrm{L} = \Phi_0^2/(4\pi^2 L_\mathrm{array})$. The resulting single-mode Hamiltonian,

$$H_\mathrm{lin} = 4E_\mathrm{C} n^2 + \tfrac{1}{2} E_\mathrm{L} \phi^2 - E_\mathrm{J} \cos(\phi + \varphi_\mathrm{ext}), \tag{3.48}$$

accurately captures the low-energy dynamics as long as the array remains in this linear regime. The phase distribution between the small-junction and the array depends on the inductive energies in the loop: in the fluxon regime ($E_\mathrm{L} \ll E_\mathrm{J}$) most phase drop occurs across the array, in the plasmon regime ($E_\mathrm{L} \gg E_\mathrm{J}$) across the small-junction, and in the quarton regime ($E_\mathrm{L} \approx E_\mathrm{J}$) the phase divides roughly equally between both.

Equation (3.48) serves as the practical basis for modeling the measured qubit spectra in this work. Using effective parameters $(E_\mathrm{C}, E_\mathrm{J}, E_\mathrm{L})$, the model reproduces the experimentally observed transition frequencies such as ω_{01} and ω_{12} with accuracy. Here, E_C represents the effective charging energy of the entire circuit, while E_J and E_L are phenomenological quantities that capture the nonlinear Josephson branch and the array's inductive response, respectively. Despite this simplification, fitted values of E_J and E_L typically provide realistic estimates of the critical current I_c of the small-junction and of the array inductance L_array, as demonstrated in previous experimental works employing junction arrays for fluxonium and related qubit designs [2–5].

3.4.3 Capacitance inhomogeneity and ground coupling

For non-uniform array junctions with different capacitances C_j, the kinetic term in Eq. (3.42) is a weighted sum $\sum_j C_j \dot{\varphi}_j^2$ that cannot be diagonalized by a simple orthogonal transformation. In this case, one introduces the capacitance matrix $\mathbf{C} = \mathrm{diag}(C_1, \ldots, C_N)$ and defines the collective mode as the phase combination

$\phi = \sum_j \varphi_j$ that minimizes the kinetic energy for fixed $\dot{\phi}$. This yields an effective capacitance

$$C_{\text{eff}} = C_{\text{sh}} + C_{\text{J}} + \left(\sum_{j=1}^{N} \frac{1}{C_j} \right)^{-1}, \tag{3.49}$$

and hence an effective charging energy $E_{\text{C}} = e^2/(2C_{\text{eff}})$ [41, 136]. Ferguson *et al.* [41] and Viola *et al.* [136] showed in numerical calculations with variations $\Delta C_j/C_j \sim 0.1$, that corrections to E_{C} remain below a few percent, validating the one-dimensional approximation (3.45).

In realistic devices, each island of the array also possesses a small parasitic capacitance C_{g} to ground or adjacent wiring. Including these terms adds

$$\mathcal{L}_{\text{kin}} = \frac{1}{2(2e)^2} \Big[(C_{\text{sh}} + C_{\text{J}}) \left(\sum_j \dot{\varphi}_j \right)^2 + \sum_j (C_{\text{JA}} + C_{\text{g}}) \dot{\varphi}_j^2 \Big], \tag{3.50}$$

which introduces weak cross-coupling between the collective and plasma coordinates ($\propto \dot{\phi}\,\dot{\xi}_k$) and slightly renormalizes the effective capacitance to

$$C_{\text{eff}} \simeq C_{\text{sh}} + C_{\text{J}} + \frac{C_{\text{JA}}}{N} + \beta N C_{\text{g}}, \tag{3.51}$$

where $\beta < 1$ depends on the spatial voltage profile along the array [41]. For typical parameters of the stacked-junction arrays in this work ($C_{\text{g}}/C_{\text{JA}} \sim 10^{-3}$–$10^{-2}$), the resulting correction to E_{C} is negligible.

Only even-parity plasma modes couple to the collective coordinate due to the parity selection rule of the phase distribution [136]. Intuitively, plasma modes with nodes at both array ends carry opposite charges on neighboring islands and thus produce no net voltage drop across the full array, leading to vanishing dipole coupling to the global mode. The remaining weak couplings slightly renormalize the qubit frequency but do not invalidate the single-mode approximation for the parameter range relevant to the stacked-junction flux qubits studied here.

3.4.4 The quarton regime

The *quarton regime* is a distinct operating regime of flux qubits that emerges when the effective inductive energy of the Josephson junction array, E_{L}, is comparable to the Josephson energy E_{J} of the small-junction. Using the notation introduced above, this balance condition is expressed as

$$\frac{\gamma}{N} = \frac{E_{\text{L}}}{E_{\text{J}}} = 1, \tag{3.52}$$

where $\gamma = E_{JA}/E_J$ denotes the ratio of the array-junction and small-junction Josephson energies, and N is the number of junctions in the array.

At the symmetry point $\Phi_{ext} = \Phi_0/2$, this balance leads to a qualitative change of the effective potential of the collective phase coordinate ϕ: the quadratic contribution in the expansion of Eq. (3.47) vanishes, and the confinement is dominated by a quartic term. This situation defines the quarton regime (Fig. 3.8 (iii)) [4, 35, 41, 136]. As a consequence of the absence of a quadratic restoring term, the qubit transition frequency is first-order insensitive to flux fluctuations at $\Phi_{ext} = \Phi_0/2$ [4]. At the same time, the strong nonlinearity of the quartic confinement gives rise to a large intrinsic anharmonicity. The quarton regime thus combines suppressed flux dispersion with strong anharmonicity.

In the ideal quarton limit $\gamma/N = 1$, the one-dimensional Hamiltonian is

$$H_Q = 4E_C n^2 + \frac{E_J}{24}\phi^4, \tag{3.53}$$

where E_C denotes the effective charging energy of the circuit. Solving the corresponding Schrödinger equation yields a discrete spectrum with a *positive* anharmonicity of approximately one third of the fundamental transition frequency,

$$\mathcal{A} \approx \tfrac{1}{3}\hbar\omega_{01}, \tag{3.54}$$

with $\omega_{01} \propto (E_J E_C^2)^{1/3}$ [4, 34, 35].

Small deviations from the ideal balance condition, $\gamma/N = 1 + \delta$ with $|\delta| \ll 1$, reintroduce a weak quadratic contribution to the potential,

$$H_Q = 4E_C n^2 + \tfrac{1}{2}E_J\delta\,\phi^2 + \frac{E_J}{24}\phi^4, \tag{3.55}$$

resulting in a *tilted quarton* [36, 37, 41]. In this case, the quartic term remains dominant while the quadratic contribution leads to small, approximately linear corrections of the energy levels.

Figure 3.9 illustrates how the qubit properties evolve when the ratio γ/N is tuned away from the ideal quarton point [4, 34, 36]. While the transition frequency f_{01} increases approximately linearly with γ/N, the relative anharmonicity $\mathcal{A}/f_{01}$ decreases monotonically. For $\gamma/N < 1$, the qubit operates at lower frequencies with enhanced relative anharmonicity, whereas for $\gamma/N > 1$ the frequency increases at the expense of reduced anharmonicity. Importantly, in the vicinity of $\gamma/N = 1$ the confinement remains weakly curved near $\Phi_{ext} = \Phi_0/2$, such that the qubit retains a suppressed first-order flux sensitivity [4, 34, 36]. As a result, the properties of the

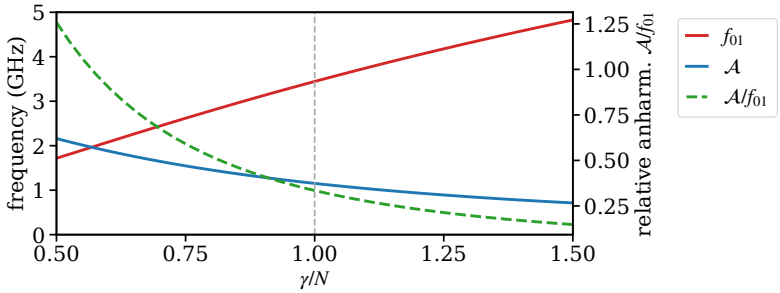

Figure 3.9: Calculated qubit frequency f_{01} and anharmonicity $\mathcal{A}$ as a function of $\gamma/N = E_L/E_J$. The vertical dashed line marks the quarton point $\gamma/N = 1$, where the quadratic term in the potential cancels and the confinement is purely quartic. At this balance point, the qubit combines large anharmonicity of $\mathcal{A}/f_{01} \approx 1/3$ with minimal flux dispersion.

quarton regime—strong anharmonicity and low flux dispersion— persist over a finite and experimentally accessible parameter range.

Experimental and theoretical research on the quarton regime is still comparatively young and actively developing. Following the initial experimental demonstration by Yan *et al.* [4], subsequent work explored quarton-based nonlinear couplers and enhanced readout schemes, both experimentally and theoretically [34–37].

In this work, quarton qubit circuits with stacked Josephson junction arrays are implemented experimentally and operated at the half-flux bias point. The focus of this thesis is on their realization and characterization as computational qubits.

3.4.5 Qubit–resonator coupling and dispersive regime

In circuit quantum electrodynamics, qubits are typically operated in the dispersive regime, where they remain far detuned from the readout resonator. This operating point enables a non-invasive measurement of the qubit state via a state-dependent shift of the resonator frequency, while avoiding energy exchange between qubit and resonator [40]. At the same time, dispersive operation strongly suppresses radiative decay through the resonator mode, known as Purcell loss (see Sec. 3.3.3).

The interaction between a superconducting qubit and a single electromagnetic mode is captured by the Jaynes–Cummings Hamiltonian, the cornerstone of circuit quantum electrodynamics (cQED). [84, 104]. For a qubit coupled capacitively or inductively to a resonator mode, the total Hamiltonian reads

$$H_{JC} = \hbar\omega_r a^\dagger a + \frac{\hbar\omega_{01}}{2}\sigma_z + \hbar g(a\sigma_+ + a^\dagger\sigma_-), \tag{3.56}$$

where ω_r and ω_{01} denote the bare frequencies of the resonator and qubit, g is the coupling rate, and a ($a^\dagger$) are the photon annihilation (creation) operators. The qubit is treated as an effective two-level system with Pauli operators σ_z, $\sigma_\pm$. The third term describes coherent exchange of excitations between the two subsystems, and the rotating-wave approximation applies when $g \ll \omega_r, \omega_{01}$.

The eigenstates of Eq. (3.56) form the JC ladder of hybridized states

$$|n,\pm\rangle = \frac{1}{\sqrt{2}}\big(|e,n\rangle \pm |g,n+1\rangle\big), \tag{3.57}$$

whose energies

$$E_{n,\pm} = \hbar\omega_r(n+1/2) \pm \frac{1}{2}\hbar\sqrt{\Delta^2 + 4g^2(n+1)} \tag{3.58}$$

depend on the detuning $\Delta = \omega_{01} - \omega_r$. When the detuning is large compared to the coupling strength ($|\Delta| = |\omega_{01} - \omega_r| \gg g$), the JC Hamiltonian can be diagonalized perturbatively by means of a Schrieffer–Wolff transformation, leading to the dispersive Hamiltonian

$$H_{\text{disp}} = \hbar\big(\omega_r + \chi\sigma_z\big)a^\dagger a + \frac{\hbar}{2}\big(\omega_{01} + \chi\big)\sigma_z, \quad \chi = \frac{g^2\Delta}{\Delta^2 - (\alpha/2)^2} \overset{|\alpha|\ll|\Delta|}{\approx} \frac{g^2}{\Delta}, \tag{3.59}$$

where α is the qubit anharmonicity and χ is the state-dependent frequency shift (dispersive shift) of the resonator [84]. Here, α is understood as the effective anharmonicity extracted from the lowest transitions of the qubit spectrum. The common approximation $\chi \approx g^2/\Delta$ holds strictly for weakly anharmonic systems (e.g. transmons), but for flux-type qubits with large positive α the full expression must be used. Equation (3.59) shows that the resonator frequency depends on the qubit state, forming the basis of the dispersive readout scheme. The dispersive shift χ arises as a second-order effect in the qubit–resonator coupling g, reflecting virtual photon exchange processes between the two systems. These off-resonant interactions lead to a state-dependent frequency renormalization of both the qubit and the resonator, while conserving the total excitation number. In the same perturbative picture, the Purcell decay can be interpreted as a real-photon counterpart of the same mechanism, in which energy leakage through the resonator mode provides a decay channel for the qubit [84, 137].

The large positive anharmonicity of the quarton qubit enhances the magnitude of χ for a given coupling g, allowing efficient state discrimination while keeping the system in the dispersive regime ($g/\Delta \ll 1$). The same large α simultaneously suppresses the Purcell decay rate,

$$\Gamma_{\text{Purcell}} = \frac{\kappa g^2}{\Delta^2 + (\kappa/2)^2} \overset{|\Delta|\gg\kappa/2}{\approx} \kappa\left(\frac{g}{\Delta}\right)^2, \tag{3.60}$$

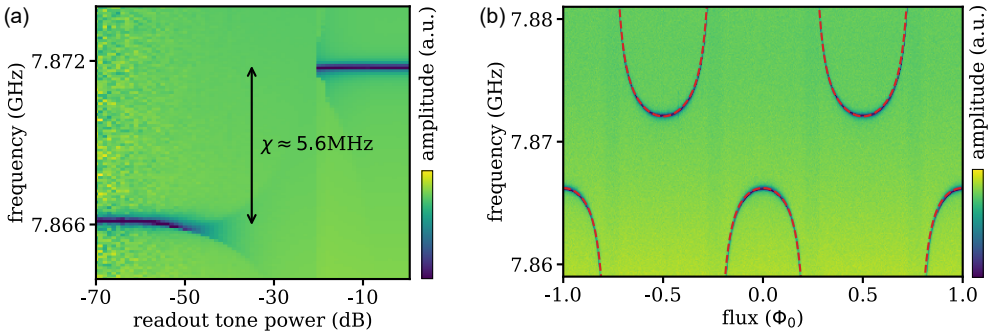

Figure 3.10: Dispersive readout and flux dependence of the resonator frequency. (a) Readout-tone power sweep at zero flux showing how the qubit and resonator hybridize at low photon number and decouple at high power. The resulting shift of the resonator frequency ($\chi \approx 5.6\,\mathrm{MHz}$) yields a coupling strength of $g \approx 63\,\mathrm{MHz}$ via the dispersive relation. (b) Resonator frequency versus applied flux in the weakly driven regime. The Φ_0-periodic modulation reflects the flux-dependent qubit transition frequency, which detunes by several GHz across the scan. The red line is a fit to the Jaynes–Cummings model in Eq. (3.56), yielding $g \approx 63\,\mathrm{MHz}$ in excellent agreement with panel (a). The avoided crossings between integer and half-integer flux values illustrate where the qubit approaches resonance condition with the readout mode. Data shown were taken on flux-qubit device *L-D1* with a stacked-junction inductor (see Table 6.2 in Sec. 6.3).

where κ is the resonator linewidth. This expression follows from a Lindblad treatment of the coupled qubit–resonator system and shows that large detuning and strong anharmonicity both reduce spontaneous emission through the resonator [84, 137]. This balance of strong dispersivity and reduced radiative loss constitutes one of the main practical advantages of the quarton qubit in cQED architectures.

All qubit spectroscopy and time-domain experiments presented in this work operate deeply in this dispersive regime, ensuring that the resonator acts solely as a non-invasive probe of the qubit state and Eq. (3.59) can be applied. The readout signal arises from the qubit-state-dependent shift of the resonator frequency $\omega_\mathrm{r} \to \omega_\mathrm{r} \pm \chi$, measurable through the transmitted or reflected microwave tone. This principle underlies both the steady-state spectroscopy of the quarton qubit and its pulsed readout during coherence measurements.

In the measured devices $\omega_{01}/2\pi \approx 3 - 5\,\mathrm{GHz}$, $\omega_\mathrm{r}/2\pi \approx 7.5 - 8\,\mathrm{GHz}$, and $g/2\pi \approx 50 - 70\,\mathrm{MHz}$. The qubit–resonator detuning is $|\Delta| \sim (45\text{–}90)\,g$, ensuring dispersive operation with sufficient readout contrast while limiting Purcell loss. The dispersive shift $\chi/2\pi$ is in the range of several MHz, which is consistent with experimental observations at a representative device in Fig. 3.10. The following section introduces the microwave environment and resonator design used for dispersive readout and qubit control.

3.5 Microwave circuits

Superconducting qubits operate in the microwave frequency range and are embedded in on-chip networks of resonators, transmission lines, bias elements, and filters. These microwave circuits form an integral part of the experimental setup for qubit experiments: they are fabricated on the same chip as the qubit, are specifically designed for a given device, and mediate both control and readout of the quantum degrees of freedom.

A quantitative description of these circuits is therefore essential for understanding how qubits couple to propagating electromagnetic modes and how microwave signals are injected, routed, and detected. This section introduces the theoretical background required to describe superconducting microwave circuits in the frequency range of several gigahertz.

3.5.1 Impedance

The concept of impedance extends the notion of DC resistance to time-dependent signals and provides a unified description of how microwave circuits respond to oscillating electromagnetic fields. In the frequency domain, it relates voltage and current via

$$Z(\omega) = \frac{V(\omega)}{I(\omega)} = R(\omega) + iX(\omega), \tag{3.61}$$

where $R(\omega)$ and $X(\omega)$ denote the frequency-dependent resistance and reactance, respectively. For purely reactive circuit elements, the impedance reduces to

$$Z_{\mathrm{L}} = i\omega L, \qquad Z_{\mathrm{C}} = \frac{1}{i\omega C}, \tag{3.62}$$

corresponding to ideal inductors and capacitors.

The concept of impedance becomes essential once the wavelength of the signal is comparable to the characteristic dimensions of the circuit. In this regime, voltage and current exhibit spatial dependence and acquire phase shifts along the circuit, rendering a purely lumped-element description insufficient.

A circuit element can be treated within the *lumped-element approximation* as long as its physical size l is much smaller than the wavelength λ of the relevant signal, typically $l \lesssim \lambda/20$ [138, 139]. For superconducting qubit circuits operating at frequencies of order 10 GHz, typical on-chip dimensions of a few hundred micrometers remain well within this regime. Accordingly, qubits and their immediate

circuit environment can be modeled using discrete inductances, capacitances, and Josephson junctions, while extended circuit structures are more appropriately described as transmission lines.

Coplanar transmission lines are modeled as distributed networks characterized by a per-unit-length inductance L' and capacitance C'. These effective parameters account for electromagnetic energy stored both in the substrate and in the vacuum above the conductors. The characteristic impedance and phase velocity of the line are given by

$$Z_0 = \sqrt{\frac{L'}{C'}}, \qquad v_{\mathrm{ph}} = \frac{1}{\sqrt{L'C'}}. \tag{3.63}$$

For a line segment of total length l, the propagation constant is $\beta = \omega/v_{\mathrm{ph}}$. Standing-wave modes arise when the boundary conditions enforce an integer multiple of half the wavelength along the line. In circuit quantum electrodynamics, nearly all on-chip microwave components—including transmission lines, resonators, and Purcell filters—can be treated as such distributed two-port networks.

The free-space impedance $Z_{\mathrm{vac}} = \sqrt{\mu_0/\varepsilon_0} \approx 377\ \Omega$ provides a natural reference scale for electromagnetic wave propagation by defining the intrinsic ratio of electric to magnetic field amplitudes. In practical microwave systems, coplanar and coaxial transmission lines are commonly designed for a characteristic impedance of $Z_0 \approx 50\ \Omega$, enabling efficient power transfer and minimizing reflections at interfaces.

When a microwave signal encounters a load impedance Z_{L} different from Z_0, a fraction of the incident wave is reflected. This reflection is quantified by the reflection coefficient [138, 139]

$$\Gamma = \frac{Z_{\mathrm{L}} - Z_0}{Z_{\mathrm{L}} + Z_0}, \qquad |\Gamma|^2 = \frac{P_{\mathrm{ref}}}{P_{\mathrm{inc}}}, \tag{3.64}$$

where P_{ref} and P_{inc} denote the reflected and incident powers, respectively. Impedance mismatches are particularly critical in signal paths where phase and amplitude information encode measurement data, such as in qubit readout circuits. In contrast, moderate mismatches in drive lines are often tolerable, as increased drive power can compensate for partial reflections.

For more complex microwave networks with multiple ports and frequency-dependent coupling, it is convenient to generalize the impedance concept to matrix relations between voltage and current amplitudes. This formulation naturally leads to the scattering matrix (S-matrix) representation discussed in the following subsection.

3.5.2 Scattering parameters and microwave networks

Linear microwave networks are conveniently described in terms of scattering parameters, or *S-parameters*, which relate incoming and outgoing traveling waves at the ports of a device. For an N-port network, the column vectors $\vec{a} = (a_1, \ldots, a_N)$ and $\vec{b} = (b_1, \ldots, b_N)$ denote the complex amplitudes of the incident and outgoing waves, respectively, and are related by $\vec{b} = \mathbf{S}\,\vec{a}$ [138]. The matrix elements S_{ij} quantify the reflection ($i = j$) and transmission ($i \neq j$) properties of the network, assuming matched source and load impedances $Z_0 = 50\ \Omega$.

For a two-port system, this relation reads

$$b_1 = S_{11}a_1 + S_{12}a_2, \tag{3.65}$$

$$b_2 = S_{21}a_1 + S_{22}a_2, \tag{3.66}$$

where S_{11} and S_{22} describe reflections at the respective ports, while S_{21} and S_{12} quantify forward and backward transmission. The amplitudes are normalized such that $|a_i|^2$ and $|b_i|^2$ correspond to the incident and outgoing power at each port.

For a one-port device, such as a reflection-type resonator, the relevant quantity is the reflection coefficient S_{11}. Its magnitude determines the reflected power fraction, while the phase $\arg(S_{11})$ contains information about the frequency-dependent impedance of the device. Deviations of the load impedance from Z_0 lead to partial reflection of the incident wave.

The incoming and outgoing wave amplitudes at port i can be expressed in terms of the total voltage V_i and current I_i as [138, 139]

$$a_i = \frac{1}{2\sqrt{Z_0}}(V_i + Z_0 I_i), \qquad b_i = \frac{1}{2\sqrt{Z_0}}(V_i - Z_0 I_i). \tag{3.67}$$

For a lossless network, power conservation implies the unitarity condition $\mathbf{S}^\dagger\mathbf{S} = \mathbf{1}$.

The S-matrix formalism is particularly well suited for describing complex microwave circuits composed of multiple interconnected components, as commonly used in circuit quantum electrodynamics. Experimentally, scattering parameters are obtained from complex transmission and reflection measurements, for example using a vector network analyzer.

Microwave resonators used for qubit readout can be realized either as reflection-type devices, probed via S_{11}, or as notch-type resonators side-coupled to a transmission line and measured in transmission (S_{21}). Both geometries can be implemented as $\lambda/4$ or $\lambda/2$ resonators, corresponding to standing-wave modes with current nodes and antinodes determined by the boundary conditions.

For a reflection-type resonator coupled capacitively to a transmission line, the scattering response takes the form [40]

$$S_{11}(\omega) = 1 - \frac{\kappa_c}{i(\omega - \omega_r) + \kappa/2}, \tag{3.68}$$

where ω_r denotes the resonance frequency, κ_c the external coupling rate, and $\kappa = \kappa_i + \kappa_c$ the total linewidth including internal and external loss contributions. The coupling rate sets the strength of the interaction between the resonator and the measurement line and thereby determines the measurement bandwidth and signal strength. Knowledge of the scattering response allows one to directly infer the frequency-dependent impedance of a device. For a one-port network, the impedance is given by [138]

$$Z(\omega) = Z_0 \frac{1 + S_{11}(\omega)}{1 - S_{11}(\omega)}. \tag{3.69}$$

In the following section, these concepts are applied to coplanar microwave resonators, which constitute the central coupling elements between superconducting qubits and measurement lines.

3.5.3 Resonators and Purcell filter for qubit readout

Superconducting qubits are read out dispersively via on-chip microwave resonators that are capacitively coupled to a common transmission line. Each resonator acts as a narrow-band filter that translates the qubit-state-dependent frequency shift into a measurable change of the complex microwave response, as discussed in Sec. 3.4.5. To suppress radiative qubit decay through the readout channel, a broadband Purcell filter is integrated between the resonators and the transmission line.

The readout circuit consists of four microwave resonators, all coupled to the same Purcell filter and transmission line (an image of a fabricated device is shown in Fig. 6.1 in Sec. 6.1). The individual resonator frequencies are set by their geometric lengths between 4.7 and 4.9 mm, resulting in designed frequency spacings of approximately 100 MHz. Their resonance frequencies range from 7.55 to 7.85 GHz, as visible in the measured scattering response shown in Fig. 3.11. The Purcell filter is designed with a center frequency of approximately 7.6 GHz, i.e. in the middle of the resonator band. Due to its large bandwidth ($\kappa_f/2\pi \sim 1$ GHz), the filter resonance spectrally overlaps with the resonator responses and is therefore not directly resolved in the measured spectrum.

The coplanar waveguide (CPW) resonators are patterned in superconducting aluminum and consist of a center conductor separated by narrow gaps from ground

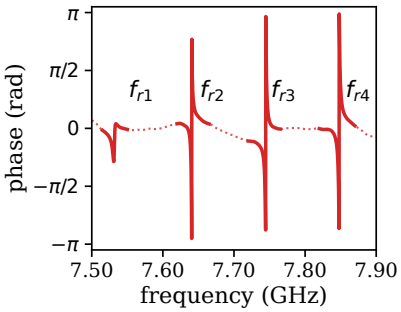

Figure 3.11: S-response measurement.

Table 3.1: Results from circle fits. Resonance frequencies, linewidths, and quality factors extracted from the circle fits shown in Fig. 3.11. The coupling quality factor Q_c quantifies the coupling of each resonator to the shared transmission line (including the Purcell filter; its broad resonance around 7.6 GHz is not resolved due to a large linewidth).

res.	f_r (GHz)	$\kappa/2\pi$ (MHz)	Q_L	Q_c
r1	7.55	1.35	5600	4800
r2	7.65	1.25	6100	5200
r3	7.75	1.15	6600	5400
r4	7.85	1.05	7300	5900

planes on both sides. Suspended aluminum links (air bridges) connect all ground-plane segments to avoid charging effects and parasitic modes. The CPW geometry supports quasi-TEM modes characterized by the per-unit-length inductance L' and capacitance C'. For a $\lambda/4$ resonator of length l, which is shorted at one end and open at the other, the resonance frequencies follow from the standing-wave condition

$$f_n = \frac{(2n-1)v_{\mathrm{ph}}}{4l}, \qquad v_{\mathrm{ph}} = \frac{1}{\sqrt{L'C'}}, \qquad n = 1, 2, \ldots, \tag{3.70}$$

where v_{ph} denotes the phase velocity of the coplanar mode. The fundamental mode ($n = 1$) is used for qubit readout.

Each CPW resonator is implemented as a $\lambda/4$ line that is shorted to ground at the junction with the Purcell filter and capacitively coupled to the qubit via a T-junction at the opposite end (Fig. 6.1). This geometry results in a current antinode at the filter side and a voltage antinode at the qubit side, consistent with strong coupling to the transmission line network at the filter side and capacitive coupling to the qubit at the opposite end.

Near resonance, the scattering response of a readout resonator is well described by a Lorentzian line shape [138]

$$S_{21}(f) = 1 - \frac{Q_L/Q_c}{1 + 2iQ_L(f - f_r)/f_r}, \tag{3.71}$$

where f_r denotes the resonance frequency, Q_L the loaded quality factor, and Q_c the external coupling quality factor; the total linewidth κ is related to Q_L by [138]

$$\kappa = \frac{\omega_r}{Q_L}, \qquad \frac{1}{Q_L} = \frac{1}{Q_i} + \frac{1}{Q_c}, \tag{3.72}$$

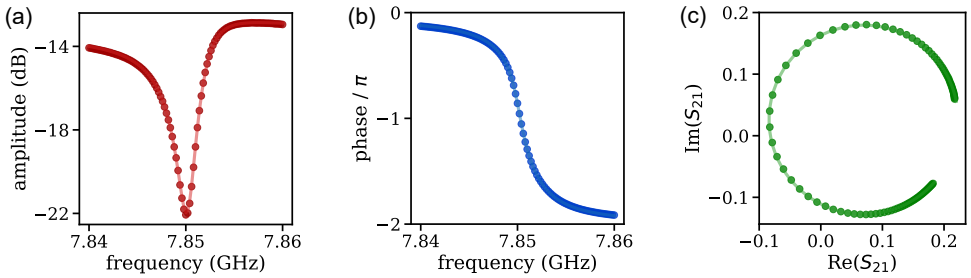

Figure 3.12: Reflection response of a readout resonator. (a) Amplitude, (b) phase, and (c) polar representation of the complex scattering response of resonator *r4* listed in Table 3.1. Solid lines indicate fits to a complex circle-fit model proportional to Eq. (3.71). The response is recorded at the vector network analyzer as a complex transmission signal (S_{21}), although it corresponds physically to a reflection measurement, due to the use of a circulator in the measurement chain.

with Q_i denoting the internal quality factor. Internal losses can originate from dielectric loss due to microscopic two-level systems in amorphous surface oxides, radiation loss, residual quasiparticles, and imperfections of the superconducting film or substrate [24, 26, 114, 132].

Depending on the relative magnitude of Q_i and Q_c, resonators can be undercoupled ($Q_\mathrm{c} \gg Q_\mathrm{i}$), critically coupled ($Q_\mathrm{c} \approx Q_\mathrm{i}$), or overcoupled ($Q_\mathrm{c} \ll Q_\mathrm{i}$). In the devices of this work, the readout resonators are intentionally designed to be overcoupled to the shared transmission line, including the Purcell filter described below, such that the loaded quality factor is dominated by the external coupling, in order to maintain a sufficiently broad measurement bandwidth and a high signal-to-noise ratio in spectroscopy measurements of the resonator frequencies.

In the chip layout, the readout resonators are coupled to a coplanar transmission line that is connected to a single microwave port, while the opposite end of the line is terminated at ground. Consequently, the readout is performed in reflection. To separate the weak reflected signal from the strong incident probe tone, a microwave circulator is used in the measurement chain (see Fig. 4.1 (b)), which routes the reflected signal to the detection line. At the vector network analyzer (VNA), located at room temperature, the reflected response is recorded as a complex transmitted signal. For this reason, the measured quantity is denoted as S_{21} throughout this section, even though the underlying physical process corresponds to a reflection measurement of the resonator.

A representative dataset of the scattering response measured with a VNA is shown in Fig. 3.12. As the probe frequency is swept across the resonance, the complex response traces out a circle in the complex plane. Fitting this circular response

using a complex-plane circle-fit model [140, 141] yields the resonance frequency f_r, the loaded quality factor Q_L, and the coupling quality factor Q_c.

Radiative decay of the qubit into the electromagnetic modes of the readout resonator and transmission line gives rise to the Purcell effect [142, 143]. In the dispersive regime, where the qubit–resonator detuning $\Delta_\mathrm{r} = \omega_{01} - \omega_\mathrm{r}$ greatly exceeds their coupling strength g, the corresponding decay rate scales as $\Gamma_\mathrm{Purcell} \propto \kappa(g/\Delta_\mathrm{r})^2$ [137, 144]. To suppress this decay channel while maintaining a broad readout bandwidth, a broadband Purcell filter is implemented between the resonators and the transmission line [145].

The filter consists of a capacitor shunted by a short section of CPW, forming a strongly coupled resonant network with coupling quality factor $Q_\mathrm{c} \approx 10$ and a center frequency $\omega_\mathrm{f}/2\pi \approx 7.6\,\mathrm{GHz}$ in the design. Due to its large linewidth $\kappa_\mathrm{f}/2\pi \approx 1\,\mathrm{GHz}$, the filter resonance overlaps spectrally with the readout resonators and is therefore not directly resolved in the measured spectrum. In the presence of the filter, the Purcell decay rate is expected to be reduced to [143]

$$\Gamma^{(\mathrm{f})}_\mathrm{Purcell} = \Gamma_\mathrm{Purcell} \left(\frac{\Delta_\mathrm{f}}{\kappa_\mathrm{f}} \right)^2, \tag{3.73}$$

where $\Delta_\mathrm{f} = \omega_{01} - \omega_\mathrm{f}$, $\kappa_\mathrm{f} = \omega_\mathrm{f}/Q_\mathrm{c}$, and Γ_Purcell denotes the Purcell decay rate in the absence of the filter. For the design parameters of the Purcell filter used in the devices of this work, a Purcell suppression factor of 10–100 is estimated for qubit–filter detunings of 3–5 GHz.

3.5.4 Local field coils and drive lines for qubit control

Qubit control in the devices studied in this thesis is realized via on-chip microwave lines and local field coils patterned in close proximity to each qubit loop. Each qubit features one dedicated *flux bias line* for tuning its transition frequency and, in the case of the four calculating flux qubits, an additional *drive line* for coherent control of its quantum state.

A current I_Φ through a local on-chip coil induces a magnetic flux $\Phi = MI_\Phi$ in the qubit loop, where M denotes the mutual inductance between the coil and the loop. To estimate this coupling, the magnetic field generated by a thin wire carrying current I_Φ at a point with distance r is expressed by the Biot–Savart law,

$$\vec{B}(\vec{r}) = \frac{\mu_0 I_\Phi}{4\pi} \int \frac{d\vec{\ell} \times \vec{r}}{|\vec{r}|^3}, \tag{3.74}$$

where μ_0 is the vacuum permeability and $d\boldsymbol{\ell}$ the differential line element along the conductor [138]. In the simplified case of a long, straight bias line placed parallel to the edge of a square qubit loop, the induced flux can be approximated by

$$M \simeq \frac{\mu_0 l}{2\pi} \ln\left(\frac{b}{a}\right), \tag{3.75}$$

where l is the loop side length, and a and b denote the inner and outer distances from the bias line to the loop edges. In this geometry, the coupling depends only weakly on the loop size but varies logarithmically with the coil–loop separation $d \approx a$. Typical designs in this work yield estimated mutual inductances of $M \approx 0.9$–$1.2\,\mathrm{pH}$, corresponding to a flux quantum of Φ_0 per bias current of roughly 1.8–2.3 mA.

The qubit loops are typically rectangular with areas of about $20 \times 30\,\mu\mathrm{m}^2$ and are placed at a vertical distance of approximately $d \approx 10\,\mu\mathrm{m}$ from the bias line. In some devices, the loop is implemented in a gradiometric loop geometry, for which only the magnetic field gradient contributes to the net flux. Because the magnetic field generated by a stripline decays approximately as $1/x$ with distance x, gradiometric loops are therefore typically positioned closer to the coil in order to achieve comparable coupling strengths. The design trade-off is that a smaller distance increases both the capacitive coupling and the risk of microwave-induced relaxation through the bias structure, which effectively behaves as a transmission line. To mitigate this effect, the bias lines are dimensioned such that their fundamental standing-wave mode is designed to lie well above 10 GHz, far from the qubit transition frequencies. They are designed with a $50\,\Omega$ characteristic impedance, enabling the combination of DC flux tuning with rapid flux pulses in future experiments.

The DC filtering of all flux bias lines in the cryostat is realized by a cascade of low-pass stages on several temperature levels, comprising both RCR and LCL filters, as described in detail in chapter 4.

While the flux bias lines control the qubit frequency via magnetic flux, the drive lines provide coherent excitation of the qubit state through capacitive coupling to the qubit island. Each drive line is implemented as a $50\,\Omega$ coplanar transmission line routed close to the qubit junction loop to enable predominantly local excitation with minimal cross-coupling to neighboring qubits. The coupling capacitance C_d determines the external quality factor Q_c of the qubit,

$$Q_\mathrm{c} = \frac{2C_{\mathrm{eff,q}}}{C_\mathrm{d}^2 \omega_{01} Z_0}, \tag{3.76}$$

where $C_{\mathrm{eff,q}}$ is the effective qubit capacitance, ω_{01} its transition frequency, and $Z_0 = 50\ \Omega$ the line impedance [143, 146]. The coupling capacitance was obtained

from electromagnetic simulations of the complete chip layout. Typical values of $C_d \approx 20$–$40\,\mathrm{aF}$ yield external quality factors in the range of $Q_c \sim 10^6$–10^7, corresponding to estimated Purcell-limited relaxation times exceeding $100\,\mu\mathrm{s}$. The drive lines are terminated in broadband matched microwave connectors at the chip carrier to avoid standing waves and reflections that could distort short control pulses.

Both types of control lines are essential components of the qubit circuitry, providing magnetic and electric access to the quantum states while being designed to maintain low cross-talk and minimal microwave back-action.

4 Experimental setup and instrumentation

This chapter describes the cryogenic infrastructure and electronic measurement setups used for both microwave spectroscopy and DC transport characterization of the qubit devices.

Superconducting quantum circuits operate in a parameter regime that requires careful control of temperature, electromagnetic environment, and signal fidelity. The aluminum-based Josephson junctions used throughout this work become superconducting below their critical temperature of approximately $T_C \approx 1.2\,\mathrm{K}$ [71]. However, to reach the quantum ground state and suppress thermal excitations of the qubit and resonator modes, the experiments must be performed at temperatures well below $k_B T \ll \hbar\omega_{01}$, corresponding to a few tens of millikelvin for qubit transition frequencies around 3–5 GHz.

Besides temperature, noise and radiation play a crucial role in preserving qubit coherence (Sec. 3.3). Moreover, stray infrared photons or black-body radiation entering through the wiring can generate quasiparticles in the superconducting films, which cause energy relaxation [147, 148]. To mitigate these effects, the experimental setup employs extensive magnetic and radiation shielding, typically combining cryoperm and superconducting enclosures as well as infrared filters and attenuators at multiple temperature stages [147, 149, 150].

A central challenge in superconducting qubit experiments lies in maintaining high signal integrity between the room-temperature electronics and the millikelvin stage. The control and readout electronics—such as arbitrary waveform generators, microwave sources, and digitizers—are typically operated at room temperature, while the qubits reside at the coldest stage of the refrigerator. This requires carefully designed signal lines that combine strong attenuation of thermal noise from higher temperature stages with low loss and high bandwidth for qubit control. On the input side, microwave drive and flux-bias lines are successively attenuated at the 3 K, 700 mK, and 10 mK stages to thermalize the photons and reduce noise reaching the sample. On the output side, the extremely weak readout signal is amplified by a

chain consisting of a low-noise cryogenic amplifier followed by room-temperature amplifiers and mixers.

While large-scale quantum processors now integrate hundreds of control and readout lines in cryogenic environments [149, 151–153], even small multi-qubit chips already demand a significant wiring complexity. In our experiment, the chip hosts four flux-type qubits and three tunable couplers, requiring one microwave readout line, one drive line per qubit, and one flux-bias line for each qubit and coupler. In total, this corresponds to nine microwave lines and at least seven DC lines for flux control.

The experiments described in the following sections were conducted using the cryogenic setup introduced below. Figure 4.1 provides an overview of the dilution refrigerator, the cryogenic wiring, and the room-temperature microwave and transport electronics. Section 4.1 introduces the dilution refrigerator and its wiring scheme, followed by Section 4.2 on the microwave circuitry and Section 4.3 describing the transport measurement setup.

4.1 Dilution refrigerator

All experiments presented in this work were carried out in a *Bluefors LD250* dry ^{3}He/^{4}He dilution refrigerator with a base temperature of approximately 10–20 mK. The cryostat provides five discrete temperature stages: the room-temperature flange, the first pulse-tube (PT) stage at about 45 K, the second PT stage at about 3 K, the still stage at approximately 700 mK, and the mixing chamber (MC) at the base temperature.

The dilution refrigerator is pre-cooled by a two-stage pulse-tube cryocooler. High-pressure helium gas is periodically compressed and expanded in the pulse tube, transporting heat from the cold end to the warm end via acoustic pressure oscillations. The first stage at $\sim$ 45 K precools the radiation shields and wiring. The second stage at $\sim$ 3 K serves as a thermal anchor for cold amplifiers (HEMTs) and acts as the condensation point for the ^{3}He/^{4}He mixture. At this stage, a Joule–Thomson valve is integrated in the cycle, cooling the mixture via isenthalpic expansion. Below this stage, the mixture flows through a heat exchanger chain consisting of capillaries and sintered silver blocks that provide large surface area for thermal exchange. The still stage at $\sim$ 700 mK evaporates ^{3}He, which is continuously pumped out by a rotary pump at room temperature. This circulation maintains the concentration gradient that drives cooling in the mixing chamber. Continuous circulation of the ^{3}He/^{4}He mixture cools the MC by exploiting the enthalpy of

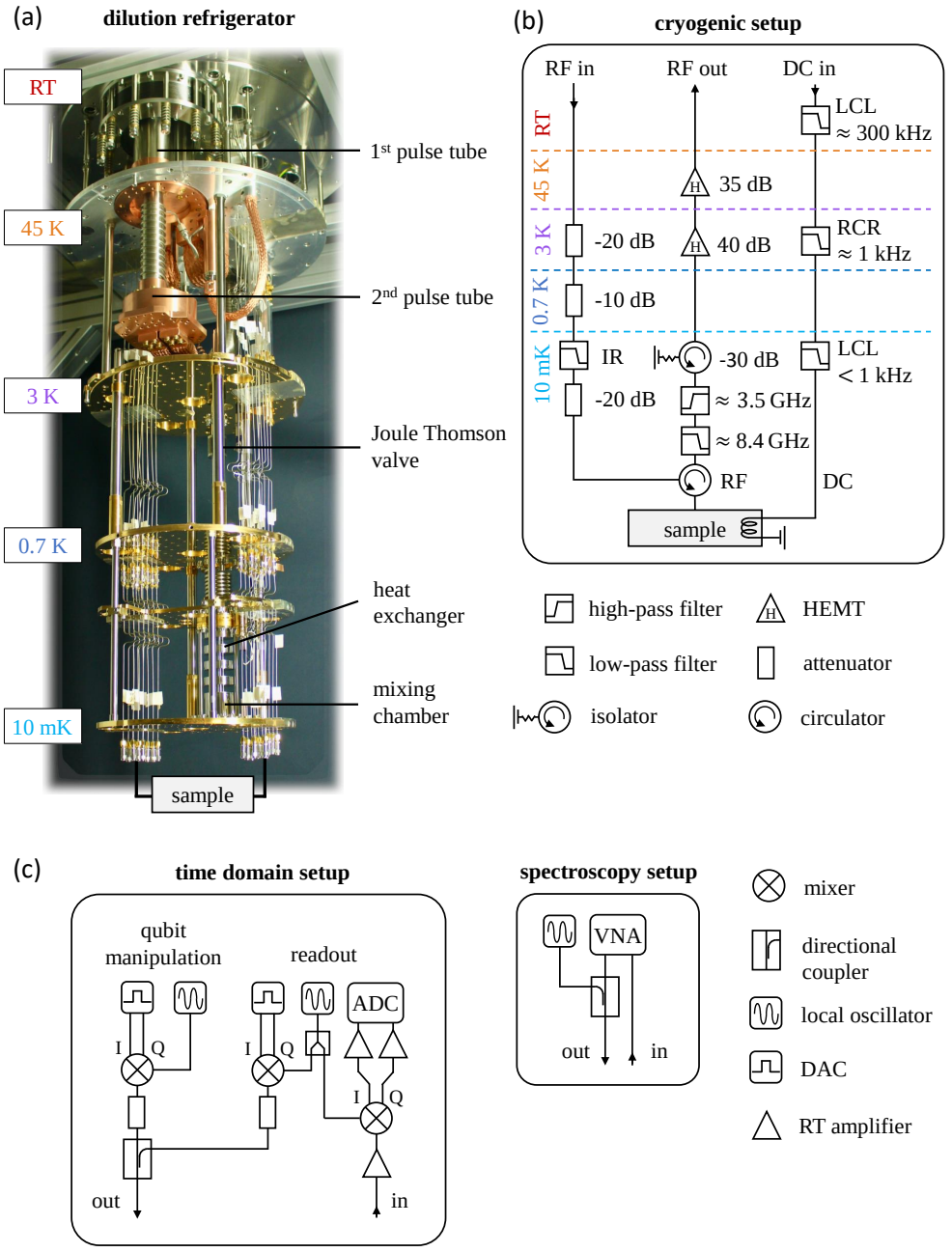

Figure 4.1: Overview of the cryogenic and room-temperature measurement setup. (a) Photograph of the *Bluefors LD250* dilution refrigerator used in this work, showing the temperature stages from room temperature down to the mixing chamber. (b) Schematic of the cryogenic wiring, including attenuation, filtering, and amplification of the RF and DC lines at the temperature stages to (a). (c) Room-temperature electronics for continuous-wave spectroscopy and pulsed time-domain experiments, including signal generation, mixing, and digitization.

dilution: when ^{3}He atoms cross the phase boundary between the concentrated and dilute phases, entropy is absorbed. The resulting cooling power scales with the ^{3}He circulation rate $\dot{n}_3$ as

$$\dot{Q}_{\mathrm{mix}} \propto \dot{n}_3 \, (T_{\mathrm{still}}^2 - T_{\mathrm{MC}}^2), \tag{4.1}$$

valid for temperatures below about 0.1 K [154, 155]. In our system, typical cooling powers of several microwatts are achieved at base temperatures of 10–20 mK. According to the Bluefors LD250 specifications, the refrigerator provides approximately 10 µW at 20 mK and 250 µW at 100 mK, corresponding to circulation rates on the order of $\dot{n}_3 \sim 1\,\mathrm{mmol/s}$ [156].

The entire experimental insert is operated in high vacuum below 10^{-6} mbar, effectively preventing convective and gaseous heat transfer. Multiple radiation shields attached to all stages above the MC reduce black-body radiation. Copper sample boxes offer good thermalization, while superconducting aluminum boxes additionally provide magnetic shielding. Both types were used in the experiments of this thesis.

All signal lines are thermalized and filtered at the temperature stages, as depicted in Fig. 4.1 (b), to minimize thermal noise and stray infrared radiation. On the input side, microwave control lines are attenuated in steps of 20 dB at the 3 K stage, 10 dB at the still, and 10 dB at the mixing-chamber stage. Attenuators at cryogenic temperatures serve both as power dividers and thermalizers: they dissipate thermal photons from higher-temperature stages and re-emit noise corresponding to their local temperature. For an attenuator with power loss A (in dB) anchored at temperature T, the equivalent noise temperature is [138]

$$T_N^{\mathrm{att}} = T_{\mathrm{in}}\, 10^{-A/10} + T\,(1 - 10^{-A/10}). \tag{4.2}$$

A cascade of attenuators at progressively lower temperatures yields a total attenuation of $A_{\mathrm{tot}} \approx 60$–$70$ dB, which effectively thermalizes the line to $T_{\mathrm{eff}} \lesssim 50$ mK for microwave frequencies of a few gigahertz. The corresponding mean photon occupation of a mode at frequency ω is

$$\bar{n} = \frac{1}{e^{\hbar\omega/k_{\mathrm{B}}T_{\mathrm{eff}}} - 1} \approx \frac{k_{\mathrm{B}}T_{\mathrm{eff}}}{\hbar\omega} \quad (\text{for } k_{\mathrm{B}}T_{\mathrm{eff}} \gg \hbar\omega). \tag{4.3}$$

For qubit frequencies of 3–5 GHz, the thermal energy $\hbar\omega/k_{\mathrm{B}} \approx 150$–$240$ mK is well above the effective line temperature, ensuring ground-state operation of the qubit and its input lines.

On the output side, the weak readout signal is successively amplified. The first stage is a cryogenic HEMT amplifier at $T \approx 3$ K, followed by a second amplifier at $T \approx 45$ K providing additional gain. The total power gain $G_{\mathrm{tot}} \approx 60$–$70$ dB ensures a sufficient signal-to-noise ratio for readout.

4.2 Microwave setup

The microwave setup provides all control and readout signals required for qubit spectroscopy and time-domain characterization. It connects the room-temperature electronics to the cryogenic quantum chip and defines the signal path from microwave generation to digitization. The physical principles underlying these measurements are introduced in Secs. 3.2.2–3.2.3, while the general network description of reflection and transmission measurements is discussed in Sec. 3.5.2. An overview of the room-temperature microwave signal chain is shown in Fig. 4.1 (c).

Depending on the experiment, the setup is operated either in continuous-wave mode or in pulsed time-domain mode. For continuous-wave and two-tone spectroscopy, a vector network analyzer (VNA) probes the complex scattering parameters of the readout resonator (Sec. 3.5.3), while a second microwave source provides a swept tone near the qubit transition frequency. Changes in the resonator response induced by the qubit are used to extract spectroscopic information.

For time-domain measurements, an arbitrary waveform generator (AWG) produces shaped baseband envelopes that are up-converted to microwave frequencies using an IQ mixer driven by a low-phase-noise local oscillator (LO). Separate microwave sources serve as LOs for the qubit drive and the resonator readout. The resulting microwave pulses are routed through a switch matrix that selects the desired experimental configuration before entering the cryostat.

Microwave control signals reach the chip either through a dedicated qubit drive line or via the readout resonator port. In devices without a separate drive line, the qubit drive tone is injected through the readout line using a directional coupler. In this configuration, the drive tone traverses both the Purcell filter and the readout resonator before coupling to the qubit. The additional insertion loss is compensated by adjusting the drive amplitude at room temperature. This approach avoids additional wiring per qubit and is well suited for single-qubit experiments, where crosstalk is not a limiting factor.

The signal reflected from or transmitted through the readout resonator carries information about the qubit state. After cryogenic and room-temperature amplification, the microwave signal is down-converted to an intermediate frequency (IF) and digitized by a high-speed analog-to-digital converter (ADC). Digital demodulation yields the in-phase (I) and quadrature (Q) components of the signal. In this work, the shot-averaged response of the demodulated signal is used to extract resonance shifts and qubit-induced dispersive signatures.

The microwave setup was employed for continuous-wave spectroscopy as well as standard time-domain experiments, including Rabi oscillations, Ramsey interferometry, spin-echo measurements, and energy-relaxation measurements. All time-domain data presented in this thesis were acquired in the averaged regime, without single-shot state discrimination.

4.3 Transport measurement setup

Four-point transport measurements were performed to characterize the superconducting properties and critical currents of the fabricated Josephson junctions. In this measurement geometry, a bias current is applied to the device under test via two leads, while the resulting voltage drop is detected across a separate pair of leads. This configuration allows the intrinsic device resistance to be measured independently of contact and wiring resistances, which is essential for the characterization of superconducting junctions at cryogenic temperatures.

To record the current–voltage (I–V) characteristics, a current-bias scheme is used. The bias current is generated by a home-made low-noise voltage-controlled current source with selectable transconductance. The circuit provides transconductance ranges between 2×10^{-2} A/V and 2×10^{-6} A/V, allowing stable biasing over several orders of magnitude. The voltage control signal is supplied by a source-measure unit (SMU) and pre-filtered by a low-noise preamplifier to suppress high-frequency noise.

The voltage drop across the sample is amplified by a low-noise instrumentation amplifier and measured by the second channel of the SMU. The I–V characteristics are typically acquired by performing linear staircase sweeps of the bias current. After each step, a short delay allows transients to decay before the voltage is recorded. The integration time of the analog-to-digital converter is synchronized to integer multiples of the power-line cycle to minimize residual 50 Hz noise.

5 Compact stacked junction inductors

This chapter is based on results published in Kreuzer et al. [32]. We first summarize Josephson junction arrays as inductive elements and introduce the stacked-junction geometry studied in this work. We then quantify stray and ground capacitances and derive the resulting mode structure. Finally, we characterize fabricated stacks by cryogenic current–voltage measurements.

5.1 Junction arrays as high-impedance inductors

Inductive circuit elements set the characteristic energy scales, mode frequencies, and coupling strengths in superconducting quantum circuits [83]. The inductance L defines the magnetic energy $E_\mathrm{L} = (\Phi_0/2\pi)^2/L$ and the circuit impedance $Z(\omega) = \omega L$ at microwave frequencies. Josephson junctions provide a compact, dissipationless inductance originating from the nonlinear phase–current relation discussed in Sec. 2.2.1. This Josephson inductance can reach values corresponding to impedances on the order of, or exceeding, the superconducting resistance quantum $R_\mathrm{Q} = h/(2e)^2 \simeq 6.45\,\mathrm{k}\Omega$ [5, 83].

Circuits with $Z \gg R_\mathrm{Q}$ are commonly referred to as *high-impedance* or *superinductive* circuits. They play a central role in several architectures, including flux qubits with an inductive shunt such as fluxonium or quarton qubits [2, 4], long Josephson junction chains used as low-loss microwave inductors [5, 94, 157, 158], and protected or strongly anharmonic qubit designs based on superinductors [3, 22, 159, 160].

Various physical mechanisms can be used to realize large inductances (Sec. 2.2.2): geometric inductors based on extended current loops, kinetic inductors exploiting the inertia of Cooper pairs in disordered superconductors such as NbN, TiN, or granular aluminum [20, 22, 161, 162], and series arrays of Josephson junctions operated in the regime $E_\mathrm{J} \gg E_\mathrm{C}$ [2, 5, 163].

For a series array of Josephson junctions, the collective inductance scales as $L_\mathrm{array} \approx NL_\mathrm{J}$, where N is the number of junctions and L_J the Josephson inductance of an individual junction. An increase of L_array can therefore be achieved either by

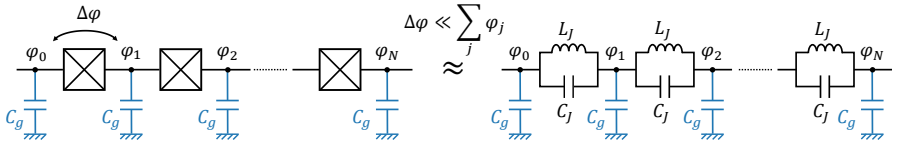

Figure 5.1: Equivalent circuit of a Josephson junction array. Each island couples capacitively to ground via C_g. For small phase drops $\Delta\varphi_i$ across individual junctions compared to the total phase drop across the array, the array behaves as a linear inductor with series inductances L_J.

reducing the critical current I_c of each junction, which increases L_J, or by connecting many junctions in series. Reducing I_c enhances the nonlinearity of the Josephson potential, leading to a strong phase dependence of the inductance and to large phase drops across the junctions. In contrast, increasing the number of junctions allows the total inductance to be scaled while keeping each junction well within the regime of small phase fluctuations. For this reason, large inductances are typically realized by increasing N rather than reducing I_c.

In many quantum-circuit implementations, Josephson junction arrays are realized as planar chains of superconducting electrodes patterned directly on the substrate, with overlapping electrodes forming the tunnel barriers. Planar junction arrays have been studied for many years and continue to be explored in a wide range of designs and layouts [5, 94, 157, 158, 163]. For long arrays, the parasitic capacitance to ground and neighboring conductors lowers the frequencies of collective plasma modes in the array, bringing them into the frequency range relevant for quantum-circuit operation. This shift in frequency thus motivates the analysis of the oscillation modes, which determine the regime in which the array behaves as a lumped-element inductor versus a distributed circuit.

5.2 Parasitic capacitance and oscillation modes

In this section, we derive the oscillation modes of a Josephson junction array and their dependence on parasitic capacitance.

We model a Josephson junction array as N identical junctions connected in series, each characterized by a Josephson energy E_J and a junction capacitance C_J. The superconducting islands possess a parasitic capacitance C_g to ground, as illustrated schematically in Fig. 5.1. For small phase excursions, the array can be described as a discrete transmission line composed of series inductances L_J and shunt capacitances

C_g [5, 164]. In the low-frequency limit ($\omega \ll \omega_p = 1/\sqrt{L_J C_J}$), this distributed circuit can be approximated as an effective lumped inductance

$$L_{\text{array}} = N L_J. \tag{5.1}$$

The ground capacitance C_g allows charge to accumulate on the islands, leading to Coulomb screening of electric fields within the array. The strength of this screening is quantified by the dimensionless *screening length* [5]

$$\lambda = \sqrt{\frac{C_J}{C_g}}, \tag{5.2}$$

which determines the number of junctions over which an injected charge or phase perturbation spreads before being screened by ground capacitance. For $\lambda \gg N$, all junctions share nearly the same phase drop and the array behaves as a single linear inductor. When λ becomes comparable to N, the islands near the center of the array become decoupled from the ends, phase and charge fluctuations are no longer uniform, and an array can no longer be described as a single lumped inductive element. In the case $\lambda < N$, increasing the number of junctions no longer increases the total inductance, as charge and current fluctuations are confined within a screening length. This defines a practical upper bound [5, 33]

$$N_{\max} \approx \pi\lambda, \tag{5.3}$$

beyond which the array is no longer well described as a lumped inductive element.

To understand the role of screening length and ground capacitance, we now derive the mode spectrum of the array. In particular, the lowest oscillation mode ω_1 defines the cutoff frequency below which the array can be treated as a linear inductance. At higher frequencies, the distributed nature of the circuit becomes relevant [164].

The oscillation modes of a junction array can be derived within the linear approximation by writing the Lagrangian in terms of the node fluxes ϕ_i (with $\dot{\phi}_i = V_i$ the node voltages) [2, 5, 94]:

$$\mathcal{L} = \sum_{i=1}^{N} \frac{C_J}{2}(\dot{\phi}_{i+1} - \dot{\phi}_i)^2 + \sum_{i=0}^{N} \frac{C_g}{2}\dot{\phi}_i^2 - \sum_{i=1}^{N} \frac{1}{2L_J}(\phi_{i+1} - \phi_i)^2. \tag{5.4}$$

Here, the first term describes the electrostatic energy in the junction capacitances, the second term accounts for the parasitic capacitances to ground, and the last term represents the magnetic energy stored in the Josephson inductors. The variables ϕ_i are flux coordinates rather than phases, $\phi_i = (\Phi_0/2\pi)\varphi_i$, such that the inductive and capacitive energies appear in symmetric form.

Applying the Euler–Lagrange equations yields a set of coupled linear difference equations for the node fluxes. Assuming open-circuit (floating) boundary conditions — appropriate for capacitively terminated arrays commonly used in floating-island circuit designs — and performing a discrete Fourier transform, one obtains the dispersion relation [5, 12, 164]

$$\omega_k = \omega_\mathrm{p} \sqrt{\frac{2(1-\cos k_m)}{\frac{C_\mathrm{g}}{C_\mathrm{J}} + 2(1-\cos k_m)}}, \qquad k_m = \frac{m\pi}{N+1}, \quad m = 1, \ldots, N, \tag{5.5}$$

where the overall frequency scale of these oscillation modes is set by the single-junction plasma frequency $\omega_\mathrm{p} = 1/\sqrt{L_\mathrm{J} C_\mathrm{J}}$. The reduction of mode frequencies below ω_p is determined by the array length N. A larger C_g relative to C_J shortens the screening length and shifts all oscillation modes to lower frequencies.

This expression describes N discrete oscillation modes of the array. The lowest-frequency mode ($m = 1$) corresponds to an almost homogeneous phase drop across the array and represents a collective oscillation of all junctions, the *fundamental mode*. Higher-order modes exhibit spatially varying phase patterns and are generally localized within a few screening lengths [5, 94, 157].

For $m = 1$, in the limits $C_\mathrm{g} \ll C_\mathrm{J}$ and $N \gg 1$, Eq. (5.5) simplifies to [5, 33, 157]

$$\omega_1 \simeq \frac{\pi}{N} \frac{1}{\sqrt{L_\mathrm{J} C_\mathrm{g}}} = \frac{\pi Z_\mathrm{c}}{L_\mathrm{array}}, \qquad Z_\mathrm{c} = \sqrt{\frac{L_\mathrm{J}}{C_\mathrm{g}}}, \tag{5.6}$$

which gives the frequency ω_1 and introduces the characteristic impedance Z_c associated with the distributed nature of the array. As the array becomes longer or the parasitic coupling to ground increases, ω_1 approaches the operational frequency range of typical quantum circuits ($\sim$1–10 GHz).

In realistic devices, capacitive couplings extend beyond nearest neighbors and are not captured by the simple analytical model. We therefore generalize the Lagrangian in Eq. (5.4) to a matrix formulation in the linear regime (small φ_i) to describe oscillation modes with arbitrary stray and mutual island capacitances,

$$\mathcal{L} = \tfrac{1}{2}\, \dot{\boldsymbol{\phi}}^\mathrm{T} \mathbf{C} \dot{\boldsymbol{\phi}} - \tfrac{1}{2}\, \boldsymbol{\phi}^\mathrm{T} \mathbf{L}^{-1} \boldsymbol{\phi}, \tag{5.7}$$

where $\boldsymbol{\phi} = (\phi_1, \phi_2, \ldots, \phi_N)^\mathrm{T}$ denotes the node fluxes, and $\mathbf{C}$ and $\mathbf{L}$ are the capacitance and inductance matrices. The symmetric matrix $\mathbf{C}$ contains all capacitive couplings between islands and to ground,

$$C_{ij} = \begin{cases} C_{\mathrm{g},i} + \sum_{k \neq i} C_{ik}, & \text{for } i = j, \\ -C_{ij}, & \text{for } i \neq j. \end{cases} \tag{5.8}$$

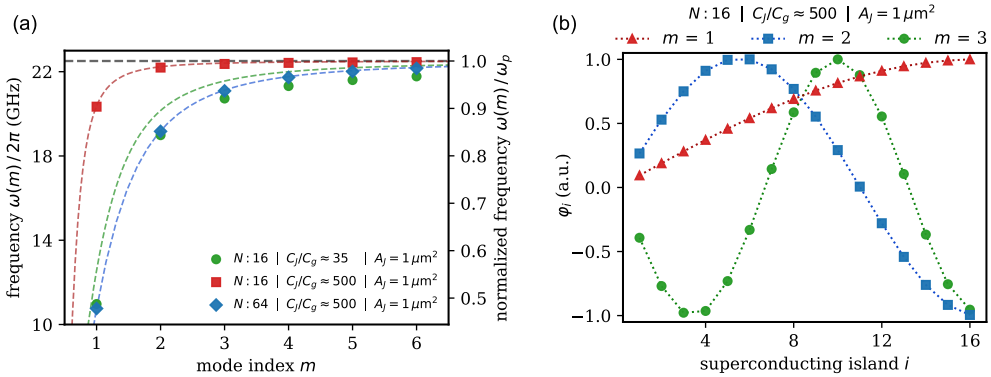

Figure 5.2: Mode dispersion in planar Josephson junction arrays. (a) Eigenmode frequencies $\omega(m)$ for three parameter sets with different ratios C_J/C_g and array lengths N. Markers denote numerically obtained eigenfrequencies from the eigenvalue problem in Eq. (5.10), dashed lines show the analytical dispersion from Eq. (5.5). (b) Normalized phase profiles along the array for the three lowest modes of the red data set in (a).

Nearest-neighbor *junction capacitances* $C_{i,i+1} = C_J$ appear on the first off-diagonals, *stray capacitances* $C_{i,j}$ with $|i-j| > 1$ on further off-diagonals (capacitive couplings between more distant islands that do not form a junction), and the *parasitic ground capacitances* $C_{g,i}$ contribute to the diagonal elements.

The inductive coupling between neighboring nodes is described by the inverse inductance matrix

$$L_{ij}^{-1} = \begin{cases} 2/L_J, & i = j, \\ -1/L_J, & |i-j| = 1, \\ 0, & \text{otherwise}, \end{cases} \tag{5.9}$$

reflecting that each island connects to two junctions (except at the ends). Applying the Euler–Lagrange equations yields the coupled equation of motion, $\mathbf{C}\,\ddot{\boldsymbol{\phi}} + \mathbf{L}^{-1}\boldsymbol{\phi} = 0$, which for harmonic solutions becomes the generalized eigenvalue problem

$$\mathbf{L}^{-1}\boldsymbol{\phi}_k = \omega_k^2\,\mathbf{C}\,\boldsymbol{\phi}_k, \tag{5.10}$$

with eigenvalues ω_k^2 corresponding to the squared oscillation-mode frequencies and eigenvectors $\boldsymbol{\phi}_k$ defining the spatial flux or phase profiles.

For a uniform array with only nearest-neighbor coupling (C_J), the eigenmodes of Eq. (5.10) are plane waves $\phi_n \propto e^{ikn}$, and their eigenfrequencies reproduce exactly the analytical dispersion of Eq. (5.5).

Figure 5.2 (a) shows the lowest six eigenmodes for three parameter sets calculated with values of C_J/C_g reported for planar junction arrays in the literature [165,

166]. For all three parameter sets, the single-junction plasma frequency is $\omega_p/2\pi \approx 22.5\,\mathrm{GHz}$, corresponding to typical junction parameters of $L_J = 1\,\mathrm{nH}$ and $C_J = 50\,\mathrm{fF}$. The fundamental mode frequency ω_1 of a 16-junction array with $C_J/C_g \sim 10$ (green points) lies at roughly one half of ω_p and falls close to the few-gigahertz range. For a larger ratio $C_J/C_g \sim 100$ (red squares), ω_1 occurs at a higher fraction of ω_p. Increasing the array length from $N = 16$ to $N = 64$ reduces ω_1 to a value close to that obtained for the shorter array with smaller C_J/C_g, consistent with the scaling $\omega_1 \propto 1/N$ given in Eq. (5.6). In all cases, the numerically obtained eigenfrequencies lie slightly below the analytical dispersion relation of Eq. (5.5) (dashed curves). This deviation arises because the analytical expression neglects stray capacitance terms between the islands, while next-nearest-neighbor couplings $C_{i,i+2}$ are included in the numerically calculated eigenfrequencies.

Figure 5.2 (b) shows the phase profiles at each superconducting island for the first three modes of the red data set in Fig. 5.2 (a). The fundamental mode corresponds to the lowest collective oscillation of the array and exhibits a smooth, monotonic phase profile, while higher-order modes show additional nodes along the array.

The examples discussed above illustrate how parasitic ground capacitance and array length determine the lowest collective modes of planar junction arrays. To explore geometries with reduced parasitic capacitance to ground, alternative array layouts have been proposed, including planar arrays suspended from the substrate [163, 167]. In the following section, we analyze the stray and ground capacitances in vertically stacked Josephson junction arrays.

5.3 Stray and ground capacitance in junction stacks

In a *stacked junction array*, multiple Josephson junctions are vertically stacked within a single junction footprint on the substrate, forming a three-dimensional inductive element. This geometry lifts the superconducting electrodes from the substrate and exposes only narrow sidewalls, enabling the realization of arrays with low parasitic capacitance to ground.

Figure 5.3 (a) schematically illustrates the basic building block of such a stacked array. Two vertical n-junction stacks are connected by a suspended superconducting bridge, forming an array with $2n + 1$ superconducting islands. Each island i is capacitively coupled to its neighbors via the junction capacitance C_J and exhibits additional stray couplings $C_{i,j}$ to more distant electrodes and to ground $C_{g,i}$, as summarized in Fig. 5.3 (b). The vertical integration lifts all electrodes above the

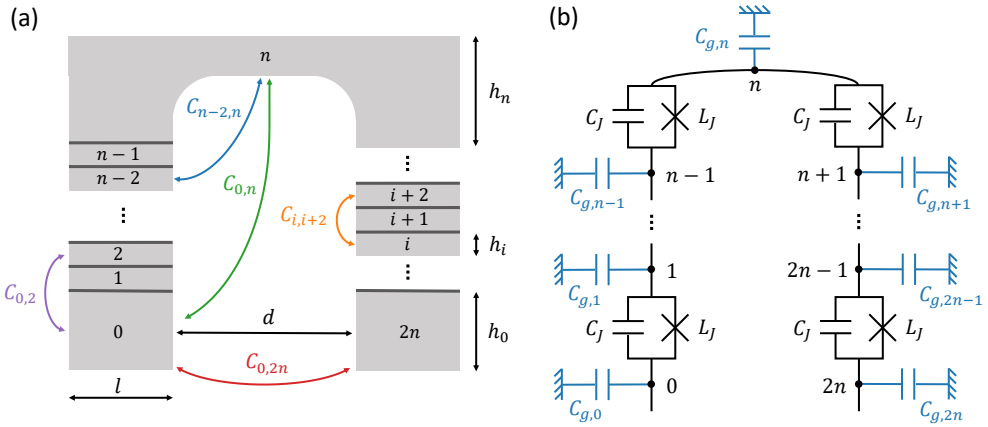

Figure 5.3: Schematics of a stack pair. (a) Schematic side view of two junction stacks connected by a superconducting bridge. The bridge width w_n is oriented perpendicular to the sketch plane. (b) Equivalent circuit representation of a double stack comprising $2n$ Josephson junctions. C_J and L_J denote the junction capacitance and inductance, and $C_{\mathrm{g},i}$ the island's capacitance to ground.

dielectric substrate, such that only the bottom electrode maintains direct contact to the substrate, while the bridge is suspended in vacuum.

We consider square stacks with footprint width l and stack distance d, as defined in Fig. 5.3. The bottom electrode has a thickness h_0 and the bridge connects the two top electrodes with height h_n and width w_n. The inner electrodes have thicknesses $h_i \ll l$. The coupling between the bottom electrodes of the two connected stacks is dominated by the electric field inside the substrate (e.g., silicon, sapphire), which typically has a dielectric constant an order of magnitude larger than that of vacuum. Capacitances between inner electrodes (with an effective capacitor area $\propto l \cdot h_i$ and $h_i \sim 10\,\mathrm{nm}$) of different stacks are negligible on the scale considered here for $d > 1\,\mu\mathrm{m}$. We consider a narrow bridge arch with $w_n < d$ and assume a linear scaling of the associated stray capacitance with w_n. Since the bridge height h_n is comparable to its width w_n, we additionally include the stray capacitance between each stacked electrode and the arch. Within this geometry, stray capacitances originate primarily from coupling between (Fig. 5.3 (a)):

(i) next-nearest-neighbor electrodes within a stack ($C_{i,i+2}$),

(ii) the bottom electrode and all inner electrodes within a stack ($C_{0,i}$),

(iii) the two bottom electrodes of opposing stacks ($C_{0,2n}$),

(iv) the bottom electrode and the suspended bridge ($C_{0,n}$), and

(v) all lower electrodes within both stacks coupling to the bridge ($C_{i,n}$).

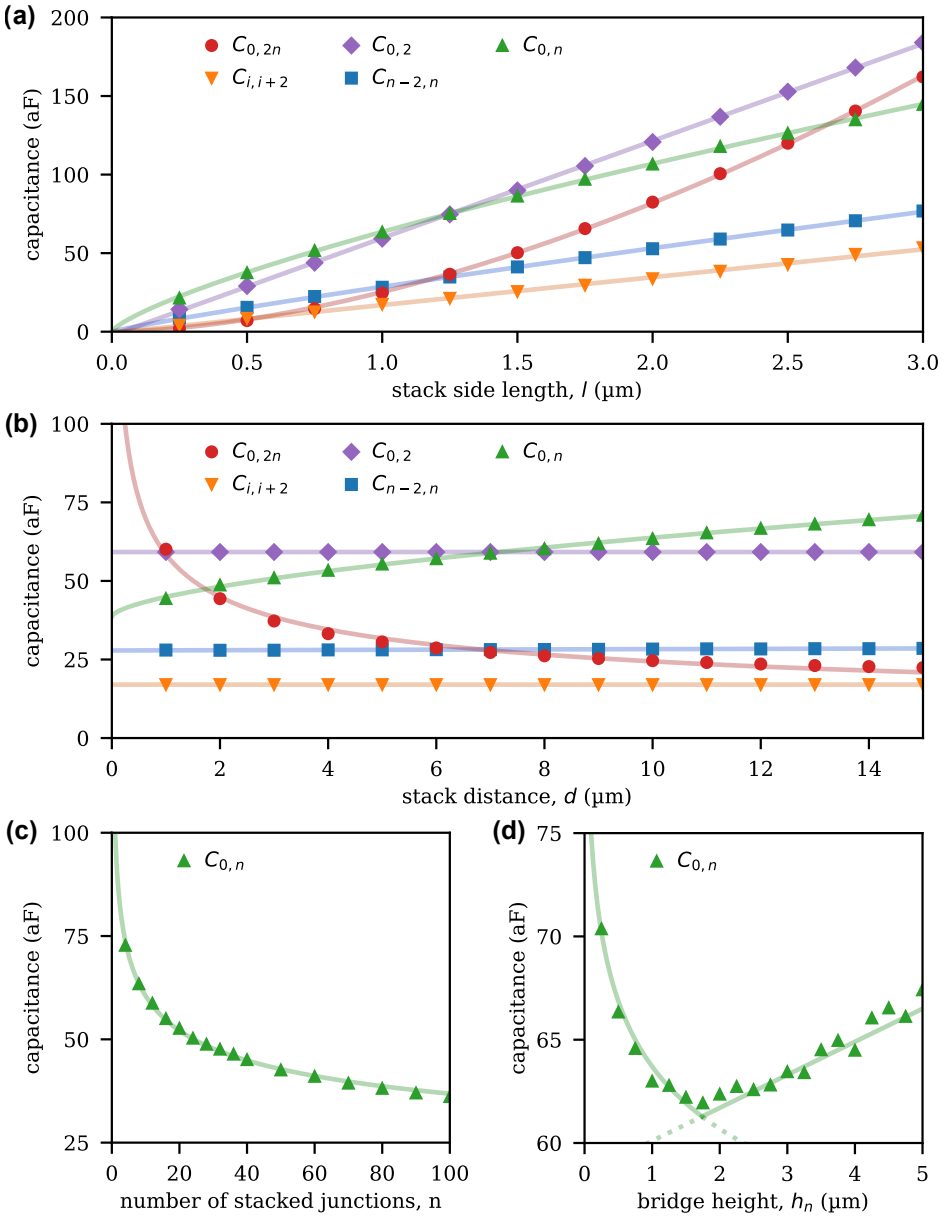

Figure 5.4: Simulated stray capacitances between superconducting islands of a stacked-junction pair. Shown as a function of (a) the footprint width l, (b) the stack distance d, (c) the number of junctions n, and (d) the bridge height h_n. The data were fitted by the empirical power-law relations summarized in Table 5.1.

Table 5.1: Empirical fits to the simulated stray-capacitance components as a function of footprint l, stack distance d, junctions per stack n, bottom electrode height h_0, and bridge height h_n (fits to Fig. 5.4). The indices (i)–(v) correspond to the coupling components introduced in the text.

comp.	C (aF)	l (µm)	d (µm)	n	h_0 (µm)	h_n (µm)
(i)	$C_{i,i+2}$	$18\,l - 1$	–	–	–	–
(ii)	$C_{0,2}$	$62\,l - 2$	–	–	$64\,h_0^{0.1}$	–
(iii)	$C_{0,2n}$	$25\,l^{1.7}$	$58\,d^{-0.4}$	–	$10\,h_0 + 24$	–
(iv)	$C_{0,n}$	$64\,l^{0.8}$	$6\,d^{0.6} + 39$	$99\,n^{-0.2}$	$30\,h_0 + 60$	$\begin{cases} 64\,h_n^{-0.1}, & h_n < 1.7\,\mathrm{m} \\ 2\,h_n + 59, & h_n \geq 1.7\,\mathrm{m} \end{cases}$
(v)	$C_{n-2,n}$	$29\,l^{0.9}$	–	–	–	–

All capacitance terms were obtained from a 3D finite-element simulation using *Ansys Maxwell* [168]. The dependence of the extracted capacitances on the geometrical parameters is shown in Fig. 5.4. For all stacks with l below 3 µm the stray capacitance is dominated by $C_{0,2}$ and $C_{0,n}$, i.e., the coupling from the bottom electrode to the next-nearest neighbor electrode in the stack and to the bridge (Fig. 5.4 (a)). For footprints larger than 3 µm the substrate contribution $C_{0,2n}$ between adjacent stacks becomes increasingly relevant. This contribution can be reduced by increasing the stack distance further (Fig. 5.4 (b)). Increasing d beyond roughly $10l$ no longer yields substantial reduction of stray coupling.

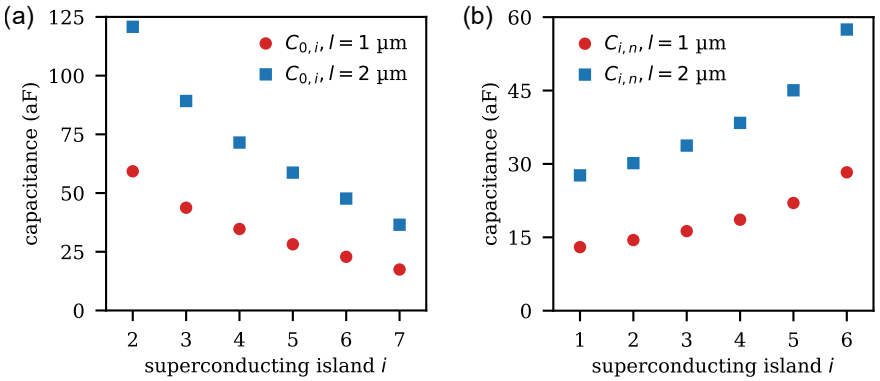

Figure 5.5: Stray capacitance contributions of inner islands. (a) Coupling of island i to the bottom electrode $C_{0,i}$, (b) coupling of island i to the bridge $C_{i,n}$. The coupling strength decreases by about a factor of three with distance to the bottom or bridge arch among the six next-nearest-neighbor islands. The absolute contribution per island scales approximately with stack width l between 1 µm (red dots) and 2 µm (blue squares) wide stacks.

The fitted scaling laws derived from the numerical data are summarized in Table 5.1. They indicate that the coupling to the bridge $C_{0,n}$ decreases with increasing number of junctions n, as the bridge is separated further from the substrate (Fig. 5.4 (c)). For narrow stacks with $n \sim 10$, lifting the arch with increasing h_n allows a reduction of $C_{0,n}$, while excessively tall bridges ($h_n > 3\,\mu\text{m}$) again increase the coupling due to their enlarged surface area (Fig. 5.4 (d)).

Among the various stray-capacitance contributions, the direct coupling between the suspended bridge and the bottom electrode, $C_{0,n}$, is the largest single term and reaches values on the order of 50–100 aF for the geometries considered here. Even this contribution, however, remains at the level of $\sim 10^{-3}$ of a typical specific junction capacitance ($C_\text{J} \approx 50\,\text{fF}/\mu\text{m}^2$ for $\text{Al}/\text{AlO}_x/\text{Al}$ junctions [47]). A LC estimate illustrates why such direct couplings do not generate additional low-energy eigenmodes. The resonance associated with a hypothetical bridge–to–bottom-electrode oscillation would occur at $\omega_{0,n} \simeq 1/\sqrt{L_{\text{seg}} C_{0,n}}$, where L_seg denotes the effective series Josephson inductance between the two nodes. Comparing this to the junction plasma frequency $\omega_\text{p} = 1/\sqrt{L_\text{J} C_\text{J}}$ with $L_\text{seg} \sim L_\text{J}$ yields $\omega_{0,n}/\omega_\text{p} \approx \sqrt{C_\text{J}/C_{0,n}} \gtrsim 30$ for $C_{0,n}/C_\text{J} \sim 10^{-3}$. Consequently, any mode primarily associated with such stray couplings lies far above the operating band and the lowest plasma modes of the array.

Even if individual stray-capacitance terms do not introduce additional low-energy modes, their cumulative effect enters the inductance in a manner analogous to the ground-capacitance term in the Lagrangian of Eq. (5.4). The total stray capacitance of island i is therefore obtained by summing all pairwise contributions,

$$C_{\text{stray},i} = \sum_{j,\,|i-j|>1} C_{i,j}. \tag{5.11}$$

This quantity determines the renormalization of the local charging energy and thus quantifies how strongly parasitic couplings modify the low-energy dynamics [164, 169].

Table 5.2 lists the dominant contributions for an exemplary eight-junction stack pair. The bottom electrode (island 0) couples to all electrodes in its own stack and to the neighboring bottom electrode, while the bridge electrode (island $n = 8$) exhibits additional coupling to nearly all other islands of both stacks. Inner electrodes show decreasing $C_{0,i}$ and $C_{i,n}$ with distance from these elements (see Fig. 5.5 for stacks of $l = 1\,\mu\text{m}$ and $2\,\mu\text{m}$). The contributions for the second stack ($i = 9, .., 16$) follow symmetrically.

The calculated values of $C_{\text{stray},i}$ are shown in Fig. 5.6. For parameters of fabricated devices in this work ($n = 8$, $l = 1$–$2\,\mu\text{m}$, $d = 10\,\mu\text{m}$, $h_0 = 100\,\text{nm}$, $h_i = 35\,\text{nm}$, $h_n = 3\,\mu\text{m}$, $w_n = 1\,\mu\text{m}$), the ratio $C_{\text{stray},i}/C_\text{J}$ remains below 10^{-3} for all islands.

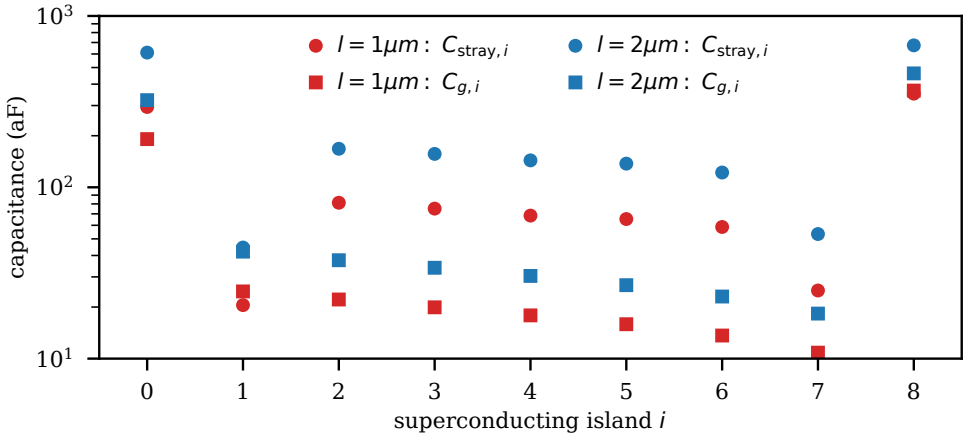

Figure 5.6: Total stray capacitance $C_{\mathrm{stray},i}$ (dots) and ground capacitance $C_{g,i}$ (squares) along an eight-junction stack. Red markers denote a 1 µm wide stack, blue markers correspond to 2 µm. The outermost islands correspond to the bottom electrode ($i = 0$) and the bridge arch ($i = 8$).

For the geometries considered here, the simulated stray-capacitance values indicate that stray couplings primarily renormalize the inductance, leading to small frequency shifts and weak modifications of the phase profiles, without introducing additional low-lying resonances or mode segmentation. The stacked array is therefore well captured by a nearest-neighbor model augmented by island-dependent ground capacitances [170, 171].

Table 5.2: Dominant contributions to the stray capacitance of each superconducting island in one stack of an eight-junction stack pair. Only terms with $C_{i,j} > 10^{-4} C_{\mathrm{J}}$ are included.

island i	dominant contributions
0	$\sum_{j=2}^{n} C_{0,j} + C_{0,2n}$
1	$C_{1,3} + C_{1,n}$
2	$C_{0,2} + C_{2,4} + C_{2,n}$
3	$C_{0,3} + C_{1,3} + C_{3,5} + C_{3,n}$
4	$C_{0,4} + C_{2,4} + C_{4,6} + C_{4,n}$
5	$C_{0,5} + C_{3,5} + C_{5,7} + C_{5,n}$
6	$C_{0,6} + C_{4,6} + C_{6,n}$
7	$C_{0,7} + C_{5,7}$
8	$2\sum_{j=0}^{n-2} C_{j,n}$

Analogous to the stray-capacitance terms, the ground capacitances $C_{g,i}$ of the individual superconducting electrodes (including the suspended bridge) were obtained from FEM simulations in *Ansys Maxwell* [168]. All exposed or substrate-supported metallic bodies of the stack geometry were modeled as lossless conductors. The ground reference was implemented as an extended lossless ground plane on the backside of a sapphire substrate. For each island i, $C_{g,i}$ corresponds to the electrostatic coupling between electrode i and this backside ground plane.

The calculated ground capacitances $C_{g,i}$ exhibit a non-uniform distribution along the stack. For example, for the red squares in Fig. 5.6, the bottom electrode on the substrate shows $C_{g,0} \approx 100\,\mathrm{aF}$, the intermediate electrodes yield $C_{g,i} \sim 10\text{–}20\,\mathrm{aF}$, and the suspended bridge reaches $C_{g,8} \approx 370\,\mathrm{aF}$. In a multi-stack array, this pattern repeats periodically along the array axis.

For an eight-junction stack with $l = 1\,\mu\mathrm{m}$ ($A_J = 1\,\mu\mathrm{m}^2$) and $C_J \approx 50\,\mathrm{fF}$, the average over all individual ground couplings $\overline{C_g} \approx 59\,\mathrm{aF}$ yields a ratio $C_J/C_g \approx 850$. Doubling the stack width to $l = 2\,\mu\mathrm{m}$ increases this ratio by more than a factor of two: for the blue squares in Fig. 5.6, $\overline{C_g} \approx 90\,\mathrm{aF}$ and $C_J/C_g \approx 2220$. This trend follows directly from the geometry of a stack. The sidewall area that couples to ground increases approximately $\propto l$, whereas the junction area – and thus C_J – scales $\propto l^2$. As a result, the ratio C_J/C_g can increase markedly for $l \gg h_i$. An exception are the bottom electrodes, whose area scales $\propto l^2$, similar to all junctions in planar layouts, and which therefore couple more strongly to ground through the substrate (by approximately a factor ε). In addition to the stack width, reducing the bridge width w_n provides an independent design parameter to further suppress the ground capacitance C_g.

The quantitative capacitance values derived here form the basis for constructing the complete capacitance matrix C of stacked-junction arrays. In the following section, this matrix is used to calculate the collective oscillation modes of the array.

5.4 Collective modes in stacked junction arrays

In the previous section, we determined the stray and ground capacitances of a single stack pair. Building on this capacitance model, we now calculate the collective mode spectrum of junction arrays composed of multiple stacks connected in series. Each stack consists of n Josephson junctions, and m stacks form an effective array of $N = n \times m$ junctions.

The capacitance matrix C of the stacked junction array is assembled according to Eq. (5.8), including all dominant stray capacitance contributions listed in Table 5.2.

The inductance matrix L is constructed as defined in Eq. (5.9). The collective mode frequencies are obtained by numerically solving the generalized eigenvalue problem in Eq. (5.10) for different stack geometries and array configurations, while keeping the single-junction plasma frequency ω_p constant.

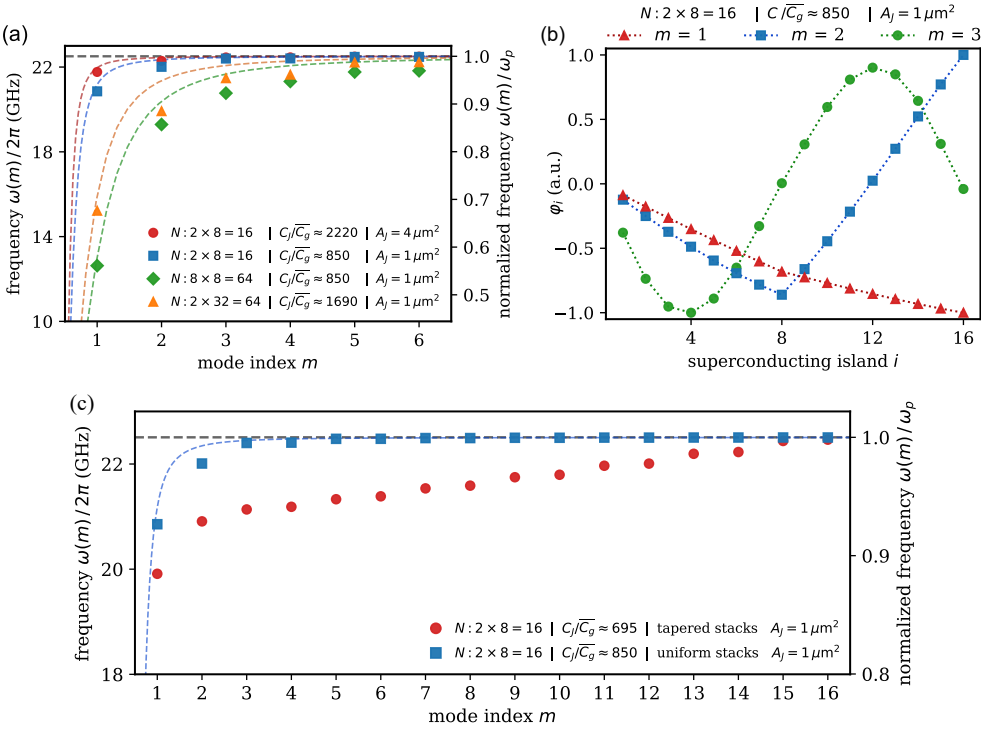

Figure 5.7: Mode dispersion in stacked junction arrays. (a) Calculated dispersion relations $\omega(m)$ for several array geometries with different stack heights and junction footprints A_J. Here, m denotes the mode index, and 2×8 corresponds to an array composed of two stacks with eight junctions each. (b) Normalized phase profiles along the array for the three lowest modes of the blue data set in (a). (c) Comparison of the mode dispersion for uniform and tapered 2×8 stacks. Tapering corresponds to a gradual increase of the junction area from the top to the bottom electrode. The fundamental-mode frequencies ω_1 corresponding to the arrays shown are summarized in Table 5.3. Markers in (a, c) denote numerically obtained eigenfrequencies from the eigenvalue problem in Eq. (5.10), dashed lines show the analytical dispersion from Eq. (5.5).

The resulting dispersion relations are shown in Fig. 5.7 (a). Dashed curves indicate the analytical dispersion relation from Eq. (5.5), evaluated using the average ground capacitance $\overline{C_\mathrm{g}} = \sum_i^N C_{\mathrm{g},i}/N$. All curves converge to the plasma frequency ω_p for higher modes, whereas the fundamental mode ω_1 varies systematically with the effective capacitance ratio $C_\mathrm{J}/\overline{C_\mathrm{g}}$. Table 5.3 summarizes ω_1, the mean screening

length $\overline{\lambda} = \sqrt{C_J/\overline{C_g}}$, the corresponding maximum array length $N_{max} \approx \pi\overline{\lambda}$, and the resulting array inductance $L_{array} = N_{max}L_J$.

Stacks with a large footprint (red dots) exhibit the highest ratio $C_J/\overline{C_g}$ and allow arrays exceeding one hundred junctions. However, the inductance per junction is small for large junction areas, when compared to arrays based on smaller junctions (see $A_J = 1\,\mu m^2$ in Table 5.3), which yield a larger total inductance for a given number of junctions. Extending a 2×8 array (blue squares) to an 8×8 array (green diamonds) reduces the fundamental mode frequency ω_1 to slightly above $\omega_p/2$, corresponding to a maximal array length of $N_{max} \approx 88$ junctions (Eq. (5.3)).

The maximal array length can be further increased by making taller stacks. In this case, the ratio $C_J/\overline{C_g}$ increases because junctions and bridges are located farther from the substrate and fewer bottom electrodes and bridges are required, resulting in a reduced average ground capacitance $\overline{C_g}$. This trend is illustrated by the comparison between the 8×8 (green) and 2×32 (orange) arrays in Fig. 5.7 (a): using 32-junction stacks, N_{max}—and thus $L_{array} \propto N_{max}$—increases to approximately 130. High stacks therefore combine a compact footprint with a reduced capacitive coupling to ground.

In fabricated devices, the junction area within a stack increases gradually from the top to the bottom electrode. For an eight-junction stack with a nominal footprint of $1\,\mu m^2$, we find a junction area of approximately $1.45\,\mu m^2$ at the bottom junction (Sec. 5.5.2). As a result, the fabricated stacks are tapered rather than uniform.

Tapered stacks are designed such that the single-junction inductance L_J remains approximately constant, while the junction capacitance scales with junction area as $C_J = C_{spec}A_J$ (see Secs. 5.5). Consequently, the local plasma frequency depends on the junction area, $\omega_p(A_J) \propto 1/\sqrt{A_J}$ such that an $n \times m$ stacked array exhibits n distinct local plasma frequencies, each repeated m times across the array.

Figure 5.7 (c) compares the dispersion of arrays composed of uniform and tapered 2×8 stacks. Two characteristic features emerge for tapered stacks as a consequence of the spatially varying junction parameters. First, the spectrum acquires a staircase-like structure: instead of converging towards a single plasma frequency, the modes cluster pairwise at local plasma frequencies $\omega_p(A_J)$, resulting in a piecewise nearly linear envelope. Second, the entire spectrum is shifted towards lower frequencies, with ω_1 reduced by approximately 1 GHz.

For stacks fabricated with tapering, this leads to a design trade-off. Increasing the number of junctions per stack reduces the capacitive coupling to ground by lifting the electrodes farther away from the substrate, similar to the case of uniform stacks. At the same time, fabrication-induced tapering increases the lateral extent

of the stack and thereby the capacitance to ground. This increase in C_g lowers the collective mode frequencies, in particular the fundamental mode $\omega_1 \propto 1/\sqrt{\overline{C_g}}$. As a result, taller stacks can remain advantageous for reducing ground coupling, while fabrication-induced tapering introduces an opposing contribution by increasing C_g and compressing the mode spectrum.

Table 5.3: Simulation results for ground capacitance and derived array parameters. Shown are representative array configurations with N junctions and single-junction footprint A_J. The average capacitance to ground per island $\overline{C_g}$ is obtained from FEM simulations (Secs. 5.2–5.3). From these values, the ratio $C_J/\overline{C_g}$ is calculated using a specific junction capacitance of $C_J \approx 50\,\mathrm{fF}/\mu\mathrm{m}^2$ for $Al/AlO_x/Al$ junctions [47]. Also listed are the screening length $\overline{\lambda} = \sqrt{C_J/\overline{C_g}}$, the fundamental mode frequency $\omega_1/2\pi$, the maximum effective array length $N_{max} \approx \pi\overline{\lambda}$ (Eq. (5.3)), and the corresponding array inductance $L_{array} = N_{max}L_J$, where L_J/A_J is fixed for comparison. A planar array configuration corresponding to Fig. 5.2 is included as a reference.

configuration	N	A_J ($\mu\mathrm{m}^2$)	$\overline{C_g}$ (aF)	$C_J/\overline{C_g}$	$\overline{\lambda}$	$\omega_1/2\pi$ (GHz)	N_{max}	L_{array} (a.u.)
2×8 stacks	16	4	90	2220	47	21.8	148	37
2×8 stacks	16	1	59	850	29	20.9	91	91
8×8 stacks	64	1	59	850	29	12.6	91	91
2×32 stacks	64	1	30	1690	41	15.2	129	129
tapered 2×8 stacks	16	1	72	695	26	19.9	83	83
planar array	16	1	100	500	22	20.3	70	70

The phase distributions corresponding to the modes of Fig. 5.7 (a) are shown in Fig. 5.7 (b). Although the capacitance to ground $C_{g,i}$ varies by more than one order of magnitude along a stack (see Fig. 5.6), the phase amplitude evolves smoothly across the array. For the fundamental mode, the phase exhibits an almost linear variation across the two stacks, indicating a globally coherent oscillation. Only near the air bridge and the bottom electrode, where $C_{g,i}$ is largest, a slight curvature of the phase profile is observed.

This behavior can be understood in terms of the screening length $\lambda_i = \sqrt{C_J/C_{g,i}}$ at island i. Despite the strong spatial variation of $C_{g,i}$, the ratio $C_J/C_{g,i}$ remains large throughout the array, resulting in $\lambda_i \gg 1$ at all islands. For stacks with $A_J = 1\,\mu\mathrm{m}^2$, λ_i reaches values of $\sim$ 30–50 in the center of a stack, where $C_{g,i} \sim$ 10–20 aF, and decreases to $\sim$ 10–15 near the air bridge or bottom electrode, where $C_{g,i} \sim$ 200–300 aF. Despite these local reductions of the screening length, the phase profiles remain extended across the array, consistent with a lumped linear inductive element [172, 173].

5.5 Fabrication of stacked junction arrays

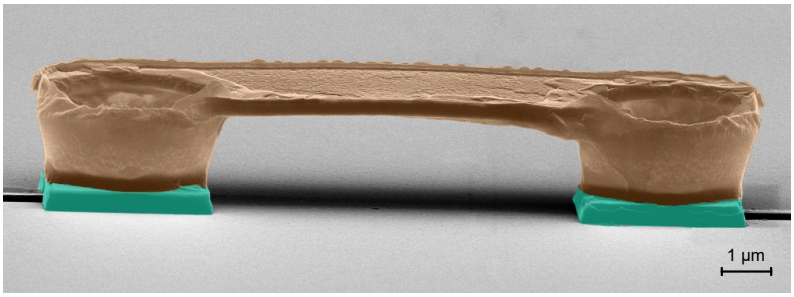

Figure 5.8: Connected stack pair. False-color scanning electron microscopy image of two stacks connected by an aluminum bridge (orange). Each stack consists of eight $Al/AlO_x/Al$ junctions (turquoise).

5.5.1 Subtractive multilayer process

The fabrication process shown in Fig. 5.9 begins with the *in situ* deposition of an $Al/(AlO_x/Al)_N$ multilayer in a Plassys^{TM} evaporator on a sapphire substrate. The multilayer consists of aluminum films separated by tunnel barriers formed by oxygen exposure, with each intermediate aluminum layer deposited to a thickness of approximately 35 nm, while the bottom and top layers are made thicker for wiring and contact purposes.

In the next step, the stacked junctions are defined by a square resist mask and etched by a dry $ArCl_2/ArCl_2O_2$ reactive-ion etching (RIE) process using an inductively coupled plasma (ICP) tool. The etch depth is calibrated to stop within the 100 nm-thick bottom layer, which serves as a wiring layer for subsequent patterning.

To connect pairs of stacks on top, a PMMA scaffold is applied to suspend the superconducting link above the substrate and prevent shorts to the junctions. The PMMA layer is spun to a thickness sufficient to cover all junctions in the stack while leaving part of the top electrode exposed to enable galvanic contact.

Stack pairs can be connected either by a suspended superconducting arch as in Fig. 5.9 (b), which requires an additional lithography step, or by a straight superconducting link as in Fig. 5.9 (c). To form an arch, a reflowed positive photoresist is patterned on top of the stacks. Before aluminum deposition and etching, native oxides on the stack surfaces are removed *in situ* in the Plassys^{TM} evaporator, after

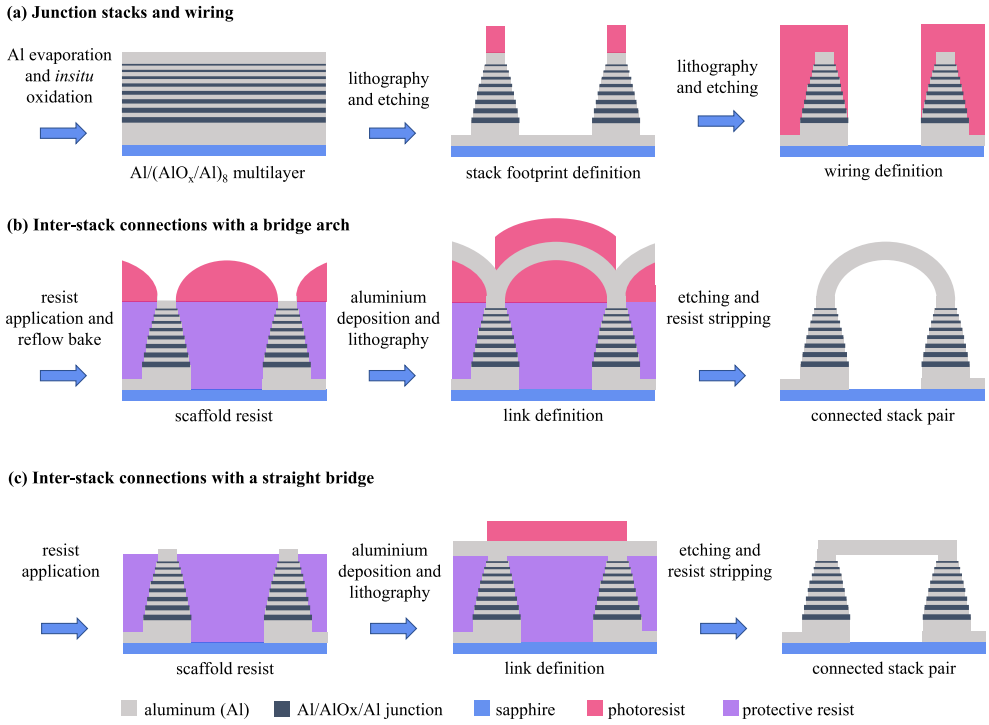

Figure 5.9: Schematic fabrication flow (not to scale). (a) Formation of Josephson junction stacks and wiring on a substrate. (b,c) Stack pairs can be interconnected either by a suspended superconducting link with a bridge arch (b) or by a straight superconducting link (c).

which the suspended link is defined by lithography and etching. For straight links, the reflowed photoresist step is omitted.

After fabrication, the wafers are diced into $5 \times 5\,\mathrm{mm}^2$ samples, followed by solvent stripping and an oxygen plasma clean.

The result of a representative array with 2×8 junctions is shown in Fig. 5.8. The two square junction stacks have a footprint of approximately $3\,\mu\mathrm{m} \times 3\,\mu\mathrm{m}$, while the bridge arch has a typical height of about $3\,\mu\mathrm{m}$ and a length of roughly $10\,\mu\mathrm{m}$.

While the multilayer process defines the overall stack geometry, the isotropic RIE step introduces a systematic tapering of the sidewalls, as visible in the scanning electron micrographs in Fig. 5.8 and Fig. 6.2 in Sec. 6.1. The resulting variation in junction area is compensated by the method described in the following subsection.

5.5.2 Compensation of junction area inhomogeneity

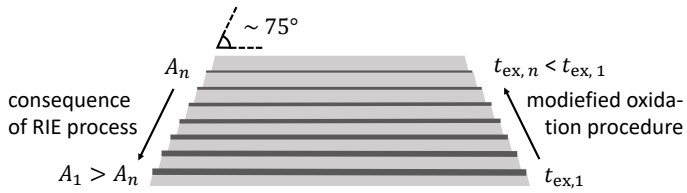

Figure 5.10: Tapered junction stack profile. Schematic cross section of a junction stack (not to scale). The slightly isotropic RIE of the $Al/AlO_x/Al$ multilayer results in a tapered profile. To compensate for the resulting junction area variations, the oxygen exposure time is progressively reduced from bottom to top.

Fabricated junction stacks exhibit tapered profiles, with junction areas increasing systematically from top to bottom within each stack, as illustrated in Fig. 5.10. This results from the slightly isotropic RIE of the $(AlO_x/Al)_N$ multilayer using $ArCl_2/ArCl_2O_2$, which etches aluminum faster than AlO_x. Consequently, when all tunnel barriers are fabricated with the same nominal critical current density, the critical currents increase with junction area according to $I_c = J_c A$. Such inhomogeneities distort the current–phase relation of the array and limit its use as a linear and scalable inductive element (see Sec. 2.2). To realize arrays that maintain a linear current–phase relation and a well-defined inductance, these effects must therefore be compensated.

In the underlying work of this thesis, two complementary strategies are implemented to mitigate the impact of junction-area variations. First, the dry-etch process is optimized to increase the sidewall angle from approximately 50° to about 75°, improving the intrinsic uniformity of the stack geometry. Second, and uniquely enabled by the stacked architecture, the tunnel barriers of individual junctions are fabricated with deliberately adjusted oxidation parameters to compensate the remaining area variations.

Specifically, the oxidation procedure in the first step of Fig. 5.9 is modified to gradually reduce the oxidation time from the bottom to the top of the stack, such that the critical currents are approximately equalized across the array. This exploits the scaling $I_c = J_c A$ and $J_c \propto \mathcal{E}^{-\alpha}$ with oxygen exposure $\mathcal{E} = p_{O_2} \cdot t_{ox}$, as discussed in Sec. 2.2.4. Consequently, the resistance–area product of each junction scales as $R_i A_i \propto \mathcal{E}^{\alpha}$, where R_i and A_i denote the normal resistance and area of the i-th junction.

Keeping a constant oxygen pressure p_{O_2}, the oxidation times are chosen to yield approximately equal normal resistances across all junctions, such that $(\mathcal{E}_i/\mathcal{E}_1)^{\alpha} \approx$

A_i/A_1, where $i = 1$ refers to the bottom junction with area A_1. An empirically determined exponent $\alpha \approx 0.4$ is used for the exposure range of 10^2 to 10^4 mbar · s [74]. During oxidation, the oxygen pressure is kept constant while only the exposure duration is varied. The resulting oxidation times are given by

$$t_{\mathrm{ox},i} = t_{\mathrm{ox},1} \left(\frac{A_i}{A_1} \right)^{1/\alpha} . \tag{5.12}$$

Table 5.4 lists the calculated oxidation times used for area-compensated stacked junctions with design footprints of $0.8\,\mu\mathrm{m}^2$ and $4\,\mu\mathrm{m}^2$. The individual junction areas A_i were not directly measured in this work. Instead, the inhomogeneity profile is inferred from the thickness of the deposited superconducting layers and the sidewall angle extracted from SEM cross sections. From these images, a typical sidewall angle of approximately 75° is estimated, which determines the bottom-to-top area ratio A_1/A_n.

Table 5.4: Calculated oxidation times for area-compensated stacked junctions. Times t_i correspond to the oxygen exposure time for the i-th junction from bottom ($i = 1$) to top ($i = 8$) of a stack.

A_{stack} (μm^2)	t_1 (s)	t_2 (s)	t_3 (s)	t_4 (s)	t_5 (s)	t_6 (s)	t_7 (s)	t_8 (s)
0.8	1266	1116	980	858	747	648	559	480
4.0	996	904	818	739	666	599	537	480

5.6 Transport measurements

In this section, transport measurements are used to characterize the electrical behavior of the fabricated stacked Josephson junction arrays. First, room-temperature resistance measurements are presented and compared for arrays with different stack footprints and junction numbers, providing information on how the normal resistance scales with the design parameters. Subsequently, current–voltage characteristics measured at cryogenic temperatures are analyzed to investigate the dynamical properties of the junctions in the superconducting state, including their switching behavior.

5.6.1 Room temperature characteristics

To study the dependence of the tunnel barrier on oxygen exposure, four wafers were fabricated under different oxidation conditions. In addition, for each wafer,

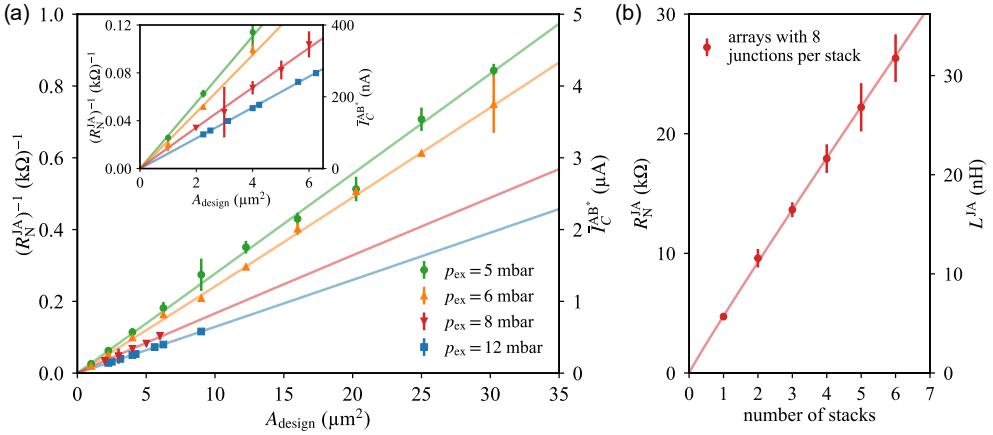

Figure 5.11: Room-temperature characteristics of stacked junction arrays. (a) Inverse normal resistance $(R_N^{JA})^{-1}$ for arrays of 2×8 junctions as a function of the designed junction area A_{design} for four oxidation pressures p_{O_2}. Solid lines are linear fits corresponding to specific resistances ρ listed in Table 5.5. The right-hand axis shows the estimated average critical current per junction $\bar{I}_c^{AB^*}$ obtained from the Ambegaokar–Baratoff relation. (b) Normal resistance R_N^{JA} versus the number of stacks n for arrays with fixed junction geometry ($A_{design} = 2 \times 2\,\mu m^2$). A fit to $R_N^{JA} = \rho\, n^b$ yields an exponent $b \approx 0.96$, consistent with the expected linear scaling ($b = 1$). The right-hand axis indicates the estimated inductance per stack.

the junction sizes were systematically varied in the design of array test structures between 1 and 30 μm^2. Figure 5.11 (a) shows the inverse normal resistance values $(R_N^{JA})^{-1}$ for arrays consisting of two stacks with eight junctions each (2×8) as a function of the designed junction area A_{design}, which is equal to the stack footprint. Each data point represents the median value of twenty test structures, and the error bars denote the corresponding standard deviation. From the Ambegaokar–Baratoff relation introduced in Sec. 2.2.4, an approximately linear scaling of $(R_N^{JA})^{-1}$ is expected with A_{design}. This expected behavior agrees with the solid lines, which are linear fits assuming a constant specific resistance ρ for each wafer. The extracted values are listed in Table 5.5. The right-hand axis gives the estimate of the average critical current per junction for each data point, $\bar{I}_c^{AB^*}$, derived from Eq. (2.32) using $\Delta_{Al} = 180$ μeV [62, 71].

In a separate experiment, arrays with eight junctions per stack were fabricated, keeping the junction footprint ($2 \times 2\,\mu m^2$) and the oxygen exposure pressure (6 mbar) fixed while the total number of stacks was varied between the test structures. Figure 5.11 (b) shows the resulting normal resistance R_N^{JA} as a function of the number of stacks n. A fit to $R_N^{JA} = \rho n^b$ yields an exponent $b \approx 0.96$, consistent with the expected linear scaling ($b = 1$). This behavior is consistent with an approximately equal contribution of each stack to the total normal resistance.

From the slope we obtain a specific resistance $\rho = 4.8\,\mathrm{k}\Omega/\mu\mathrm{m}^2$, corresponding to an inductance of approximately $L_\mathrm{J} = \Phi_0/2\pi I_\mathrm{c} \approx 5.4\,\mathrm{nH}$ per stack, using the Ambegaokar–Baratoff estimate for I_c.

Table 5.5: Specific resistance of junction stacks. Average specific resistances $\rho = R_\mathrm{N}^\mathrm{JA}/A_\mathrm{design}$ extracted from twenty arrays per wafer at different oxidation pressures p_{O_2}. The data correspond to the measurements shown in Fig. 5.11 (a).

p_{O_2} (mbar)	5	6	8	12
ρ ($\mathrm{k}\Omega/\mu\mathrm{m}^2$)	36.3	43.2	57.5	79.6

5.6.2 Cryogenic current–voltage characteristics

In this subsection, the current–voltage characteristics (IVC) of stacked junction arrays measured at millikelvin temperatures are presented and discussed within the RCSJ framework introduced in Sec. 2.2.5. The data were acquired using the setup described in Sec. 4.3 in the dilution refrigerator introduced in Sec. 4.1. We first present the IVC of tapered stacks without area compensation and subsequently compare them to compensated stacks.

Figure 5.12 shows the measured IVC of an *uncompensated* array comprising $2 \times 4 = 8$ Josephson junctions with a footprint of $4 \times 4\,\mu\mathrm{m}^2$. The measured IVC exhibits a pronounced hysteresis characteristic of strongly underdamped Josephson junctions. From the slope of the normal branch $V = R_\mathrm{N}^\mathrm{JA} I + V_0$ (see Eq. (2.52)) we obtain a normal resistance $R_\mathrm{N}^\mathrm{JA} = 1.64\,\mathrm{k}\Omega$. The total gap voltage of the array is $V_\mathrm{gap}^{(\mathrm{tot})} = 2.84\,\mathrm{mV}$, corresponding to an average single-junction gap voltage $\bar{V}_\mathrm{gap} = 355\,\mu\mathrm{V}$ for eight junctions, in good agreement with the BCS value $2\Delta/e \simeq 360\,\mu\mathrm{V}$ for aluminum at millikelvin temperatures [62, 71]. The subgap resistance, determined from the slope at small bias voltage $|V| < V_\mathrm{gap}^{(\mathrm{tot})}$, is $R_\mathrm{sg} \approx 40\,R_\mathrm{N}^\mathrm{JA}$. The ratio of switching to retrapping current yields a Stewart–McCumber parameter $\beta_\mathrm{c} = (4I_\mathrm{c}/\pi I_\mathrm{r})^2 \approx 10^3$, which indicates strongly underdamped dynamics ($\beta_\mathrm{c} \gg 1$).

A distinctive feature of the uncompensated array is the staircase-like switching on the critical-current branch. As individual junctions switch at different bias currents, the IVC exhibits discrete voltage jumps at approximately integer multiples of the single-junction gap voltage. The switching currents range from about 350,nA to 1,µA, corresponding to a spread of at least a factor of three. This spread is likely even larger because once the first junction switches to the resistive state, a dissipative quasiparticle current flows and heats the small volume of the stacked

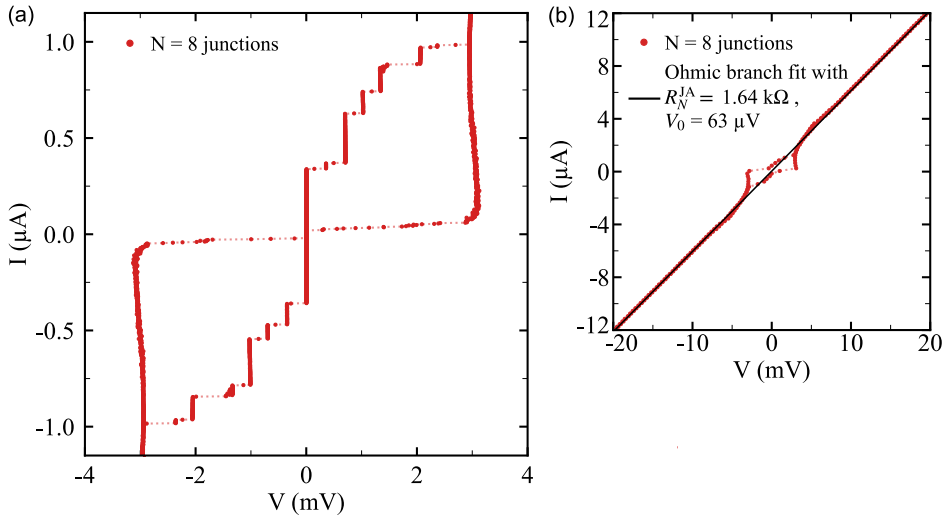

Figure 5.12: IVC of an uncompensated stacked-junction array. Array with 2×4 junctions (footprint $4 \times 4\,\mu m^2$). (a) Detail view of the hysteresis curve, showing that the individual junctions within the array switch to the normal state at bias currents between 350 nA and 1 μA. (b) IVC over an extended voltage range together with a linear fit to the normal branch, from which the normal resistance R_N^{JA} is extracted.

electrodes. The resulting local heating suppresses the superconducting energy gap and reduces the apparent I_c of the remaining junctions, promoting premature switching [72, 174].

A *large* critical-current inhomogeneity within a stack has important implications for the array's inductive behavior. Even before any junction becomes normal-conducting, nonuniform I_c causes an unequal distribution of the phase drop across the stack. Junctions with smaller I_c experience a disproportionately large phase drop and therefore dominate the total inductance (Sec. 5.1). For quantum-circuit applications, it is desirable to have junctions with approximately uniform I_c such that the phase φ is evenly distributed across the array. In this case, and for small phase excursions $\Delta\varphi < \pi/4$, each junction contributes linearly to the total inductance, which then scales approximately as $L_{array} \simeq N(\Phi_0/2\pi I_c)$ [172, 173].

To realize arrays with a linear current–phase relation and scalable inductance, these fabrication-induced nonuniformities must be compensated. We therefore compare the uncompensated arrays discussed above with arrays fabricated using an area-compensation method described in Sec. 5.5.2.

Figure 5.13 shows the measured IVC of a *compensated* array comprising $2 \times 8 = 16$ Josephson junctions with a footprint of $3 \times 3\,\mu m^2$. The IVC shows an almost

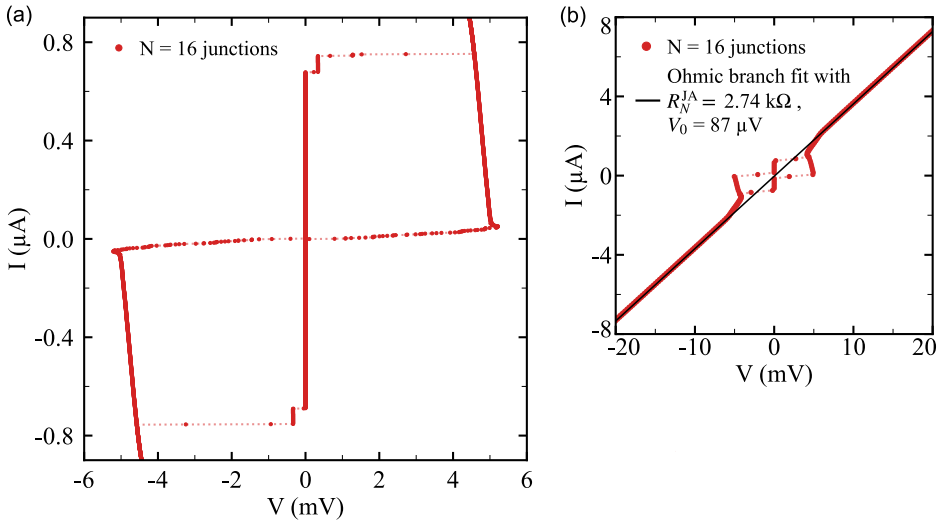

Figure 5.13: IVC of a compensated stacked-junction array. Array with 2×8 junctions (footprint $3 \times 3\,\mu m^2$) fabricated using graded oxidation exposure from bottom to top of the stack. (a) Detail view of the current–voltage characteristic, showing an almost simultaneous switching of all junctions. (b) IVC over an extended voltage range together with a linear fit to the normal branch, from which the normal resistance R_N^{JA} is extracted.

simultaneous switching of all junctions at a bias current close to 750 nA. The McCumber parameter is on the order of $\beta_c \sim 10^5$, indicating strongly underdamped junction dynamics.

From the slope of the normal branch, a total normal resistance of $R_N^{JA} = 2.74\,k\Omega$ is extracted. The subgap resistance exceeds 100 kΩ, corresponding to $R_{sg}/R_N^{JA} \sim 10^2$, which is consistent with a low subgap leakage current. The total gap voltage of the array amounts to $V_{gap}^{(tot)} \approx 5.2$ mV, yielding an average single-junction gap voltage of $\bar{V}_{gap} \approx 326\,\mu V$, consistent with the expected value for aluminum at low temperatures. Using the Ambegaokar–Baratoff relation in Eq. (2.32), the corresponding critical current is estimated as $I_c^{AB} \simeq 1.6\,\mu A$ per junction.

Assuming uniform critical currents, the array inductance is estimated as $L_{array} = N(\Phi_0/2\pi I_c) \approx 3.3$ nH, using I_c^{AB} and $N = 16$. At a representative frequency of 6 GHz, the corresponding characteristic impedance amounts to approximately $Z = \omega L_{array} \approx 120\,\Omega$, below the resistance quantum $R_Q = h/(2e)^2 \approx 6.45\,k\Omega$, but sufficiently large to serve as a linear, low-loss inductive element in superconducting circuits. This impedance can be further increased by increasing the number of stacked junctions or reducing I_c.

6 Quarton qubits with junction stacks

Compact stacked Josephson junctions, introduced and characterized in the previous chapter, enable highly inductive and low-loss circuit elements suitable for superconducting qubits. In this chapter, the spectral and coherence properties of quarton qubits employing stacked junction inductors are investigated. To identify the mechanisms limiting qubit coherence, the role of external flux noise is examined using a persistent-current bias scheme, and TLS-induced decoherence is analyzed through avoided level crossings observed in the qubit spectra.

6.1 Quarton qubit design

This section presents a design of flux qubits operating in the *quarton* regime. As discussed in Sec. 3.4.4, quarton qubits are characterized by comparable inductive energy of the junction array and Josephson energy of the small-junction, $E_\mathrm{L} \approx E_\mathrm{J}$. At $\Phi_\mathrm{ext} = \Phi_0/2$ (half-flux bias), the qubit transition frequency becomes symmetric and forms local minima, at which the potential is first-order insensitive to flux noise. Near the potential minimum at $\Phi_\mathrm{ext} = \Phi_0/2$, the qubit Hamiltonian can be approximated by

$$H \approx -4E_\mathrm{C}\frac{\partial^2}{\partial\varphi^2} + E_\mathrm{J}\left[\tfrac{\gamma/N-1}{2}\varphi^2 + \tfrac{1}{24}\varphi^4 + \mathcal{O}(\varphi^6)\right] \overset{\gamma/N=1}{\approx} -4E_\mathrm{C}\frac{\partial^2}{\partial\varphi^2} + \frac{E_\mathrm{J}}{24}\varphi^4, \quad (6.1)$$

which becomes purely quartic only when

$$\frac{E_\mathrm{L}}{E_\mathrm{J}} = \frac{L_\mathrm{J}}{L} = \frac{\gamma}{N} = 1. \quad (6.2)$$

Here, L denotes the total linear inductance of the junction array in the qubit loop and L_J the Josephson inductance of the small-junction. The parameter $\gamma = L_\mathrm{J}/L_\mathrm{JA}$ is the inductance ratio between the small-junction and a single array junction, and N is the total number of Josephson junctions in the array, such that $\gamma/N = L_\mathrm{J}/L$.

In this *quarton regime*, the qubit potential exhibits a positive anharmonicity on the order of one third of the qubit transition frequency [4].

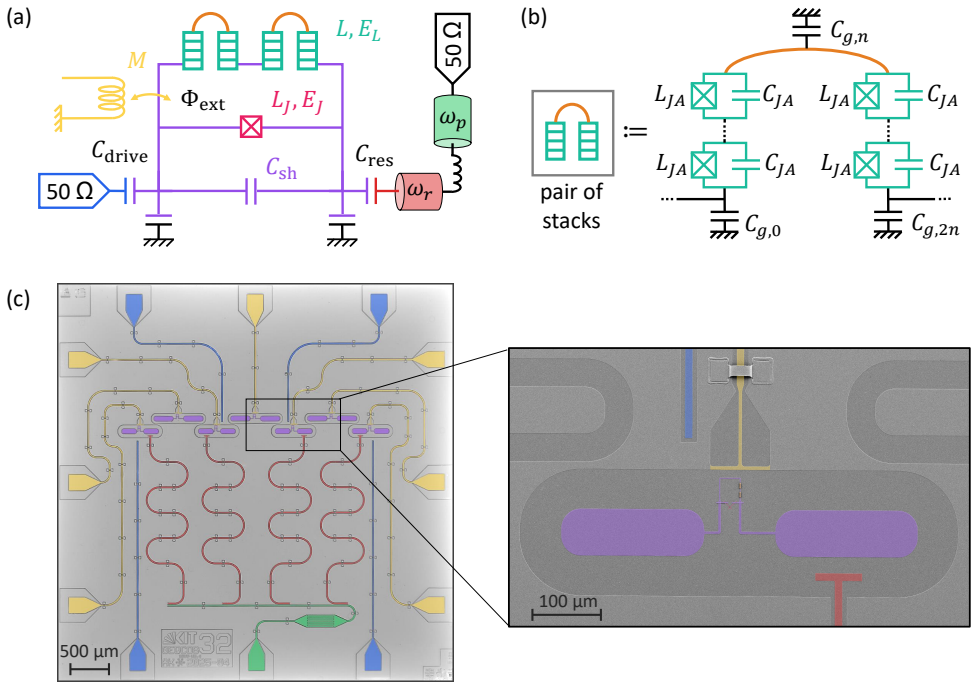

Figure 6.1: Quarton qubit implementation with stacked junction inductor. (a) Schematic of a quarton qubit circuit (purple) coupled to an external flux-bias coil (yellow), a microwave drive line (blue), and a readout resonator (red) connected to a Purcell filter (green). The inductance is implemented with junction stack pairs. (b) Circuit diagram of a pair of n-junction stacks (turquoise) connected by a link (orange). L_{JA} and C_{JA} denote the inductance and capacitance of one junction in a stack, and $C_{\text{g},i}$ the parasitic capacitance of superconducting islands to ground. (c) False-color micrograph of a $5 \times 5\,\text{mm}^2$ processor chip hosting seven quarton qubits. Four computational qubits are coupled to microwave drive lines, individual readout resonators, and a shared Purcell filter, while three additional qubits serve as tunable couplers. The zoom shows a SEM image of one computational qubit and parts of two couplers. Colors correspond to the schematic components in panel (a).

In the quarton qubit circuit layout of this work (Fig. 6.1), the linear inductance is implemented with pairs of stacked junctions. Each stack contains n Josephson junctions, and m connected stacks form an array with $N = m \cdot n$ junctions in series. These contribute to the total inductance and capacitance, resulting in $L \approx NL_{\text{JA}} = N(L_{\text{J}}/\gamma)$ and $C \approx C_{\text{JA}}/N$, where L_{JA} and C_{JA} denote the inductance and capacitance of a single stacked junction (see Sec. 3.4.2). The small-junction in the loop is realized as a cross-type (Manhattan-style) $\text{Al}/\text{AlO}_x/\text{Al}$ junction, see Fig. 6.2 (a),(d). It is formed by the orthogonal overlap of two electrodes with width w_{J}. The junction area $A_{\text{J}} \approx w_{\text{J}}^2$ sets the Josephson energy E_{J} and the capacitance C_{J}. The total qubit capacitance is $C_\Sigma = C_{\text{J}} + C_{\text{JA}}/N + C_{\text{sh}} + C_{\text{g}}$, including a shunt

capacitor C_{sh}, and stray capacitance C_g to ground. Based on FEM simulations and design data, typical parameter values are $C_{sh} \approx 20\,\text{fF}$, $C_J \approx 2\,\text{fF}$ (estimated from $C_{spec} \approx 50\,\text{fF}/\mu\text{m}^2$ and a area of the small-junction $\sim 0.04\,\mu\text{m}^2$), $C_{JA}/N \approx 1$–$10\,\text{fF}$ (for stack footprints of 0.8–4 μm^2 and $N = 16$–48), and C_g of a few fF as discussed in Sec. 5.3. The shunt capacitance ensures operation in the flux regime $E_J \gg E_C$.

small-stack design variant:

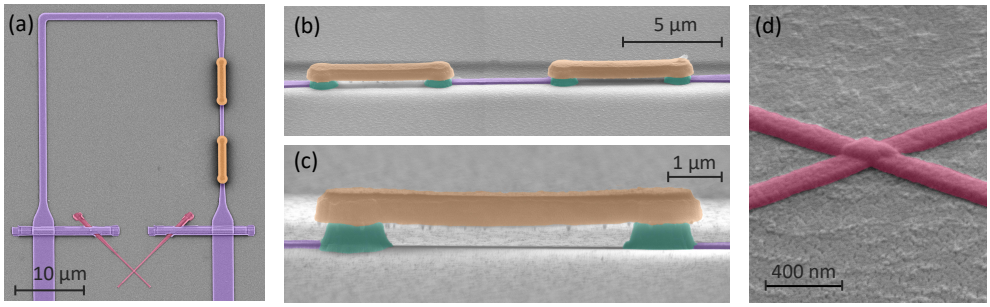

large-stack design variant:

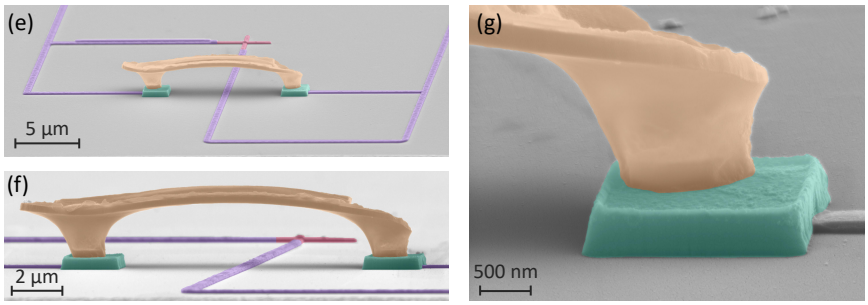

Figure 6.2: Fabricated quarton qubit loops. Top: small-stack design variant. (a) False-color SEM image of a square-shaped qubit loop comprising two stack pairs (4×8-junction array) and a small cross-type junction (pink). The loop is located between the shunt-capacitor pads visible in the zoom of Fig. 6.1 (c). (b–c) Cylindrical stacks (turquoise) have a diameter of about 1 µm and are connected by a straight superconducting link (orange). (g) Close-up of a small cross-type junction fabricated in Manhattan-style with a junction area $\sim 140 \times 140\,\text{nm}^2$. Bottom: large-stack design variant. (e) Gradiometric qubit loop in the shape of a "eight". (f–g) Two stacks with square-shaped footprint of about 2 µm side length form a 2×8-junction array. The superconducting arch has a height of about 3 µm and length of 10 µm.

The qubit loop is embedded in a cutout of a coplanar superconducting ground plane and coupled to a $\lambda/4$ coplanar resonator for dispersive readout, as well as to a local flux-bias coil and microwave drive line for control. The chip layout in Fig. 6.1 (c) contains four computational quarton qubits with identical design parameter in a row. Each qubit is capacitively coupled to its dedicated readout

resonator with resonance frequencies f_r between 7.45 and 7.85 GHz (100 MHz spacing) and to a shared Purcell filter, and is equipped with an individual drive line and flux-bias coil. Details on the single components are given in Sec. 3.5.

Additional quarton qubit circuits are placed between neighboring computational qubits and used as frequency-tunable couplers. They differ from the computational qubits mainly by larger shunt-capacitor pads and the absence of direct drive and readout resonators. The effective transverse coupling rate between a coupler (c) and a qubit (q) can be estimated in the weak-coupling limit as

$$g_{c,q} \approx \frac{C_{c,q}}{2\sqrt{C_{\Sigma,q}C_{\Sigma,c}}}\sqrt{\omega_q\omega_c}, \tag{6.3}$$

which follows from the standard capacitive-coupling Hamiltonian in circuit QED [82, 104]. For the design parameter used in this work ($C_{\Sigma,c} \approx C_{\Sigma,q} \approx 25-35$ fF and an effective coupling capacitance $C_{c,q} \approx 0.2$ fF), this yields $g_{c,q}/2\pi \approx 10-15$ MHz. In the dispersive regime, $|\Delta_{c,q}| = |\omega_c - \omega_q| \gg g_{c,q}$, the residual interaction is $J_{\text{eff}} \approx g_{c,q}^2/\Delta_{c,q}$. In all measurements of this work, the couplers were detuned far from the computational qubits ($\Delta_{c,q}/2\pi > 1$ GHz), resulting in $J_{\text{eff}}/2\pi < 200$ kHz. Under these conditions, qubit–coupler and qubit–qubit interactions are negligible.

Two distinct qubit loop design variants were implemented in fabricated qubit devices, as illustrated in Fig. 6.2. A large-stack design variant employs 4 µm^2 stacks with square-shaped footprint and connected by round arches, forming a gradiometric "eight" loop, while a small-stack design variant uses 0.8 µm^2 cylindrical[1] stacks connected by straight links (non-gradiometric loop).

In this work, qubit loops with two, four and six junction stacks have been realized to vary the array inductance L. For each design value of L, the width w_J of the small-junction electrodes was adjusted to tune its overlap area A_J and inductance L_J such that the quarton condition in Eq. (6.2) was targeted for the design values.

[1] Fabrication-induced junction area variations are more pronounced for stacks with small footprints (see Sec. 5.5). A circular footprint, featuring a lower perimeter-to-area ratio than square geometries, is therefore employed to reduce junction-area variations within the small stack.

6.2 Fabrication of a quarton qubit processor chip

The fabrication process of quarton qubit processor chips (Fig. 6.1 (c)) combines junction stacks, a small cross-type junction, and on-chip microwave wiring in three fabrication steps (Fig. 6.3):

1. Fabrication of $Al/AlO_x/Al$ junction stacks, qubit shunt capacitors, base wiring, ground planes, and coplanar waveguides.
2. Addition of a single $Al/AlO_x/Al$ junction to the qubit loop.
3. Connection of stack pairs with suspended superconducting links.

The process started with polished 2″ sapphire wafers featuring a 100 nm niobium backside layer, cleaned in a piranha solution. The stacked junctions were fabricated using the subtractive process described in Sec. 5.5.1. Each stack consisted of alternating $Al/AlO_x/Al$ layers forming eight stacked junctions by controlled *in situ* oxidation. For a given wafer, the stack footprint A_{stack} is fixed to one size in the design at all qubits, and a single oxidation recipe was used so that the critical current density of the stacked tunnel barriers and thus L_{JA} were nominally uniform across the wafer. Typical oxidation pressures for the stack junctions were on the order of a few millibar, consistent with the parameters in Table 6.1. The oxidation times were varied for each tunnel barrier according to the compensation method described in Sec. 5.5.2, using the graded oxidation times listed in Table 5.4. After deposition, stacks and wiring were patterned in two electron-beam lithography and RIE steps using a negative photoresist.

The small-junctions were fabricated using a standard Manhattan-style shadow evaporation and lift-off process adapted from Kono *et al.* [175]. They were defined in an electron-beam lithography step using an MMA/PMMA double-layer resist and evaporated and oxidized in a Plassys$^{\mathrm{TM}}$ evaporator after *in situ* argon plasma milling of native oxides to ensure galvanic contact to the qubit wiring. The oxidation pressures for the small-junctions and the stacks are given in Table 6.1.

In the final step, superconducting links between stack pairs were fabricated following the process steps described in Sec. 5.5.1. Two link geometries were used: straight links in non-gradiometric layouts and arch-type links in gradiometric “eight” loops, as shown in Fig. 6.2. At one wafer, only one link geometry is used at the stacks. The qubit processor chip features large suspended arch-type links ("air bridges") to connect parts of the ground planes separated through coplanar waveguides. If small arch-type links between stacks were deployed, all links on the wafer were fabricated together in a single process step. For designs with straight

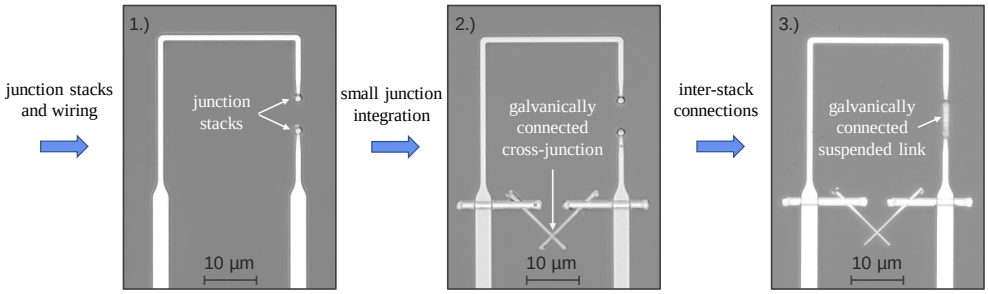

Figure 6.3: Fabrication steps to build a quarton qubit loop. Microscope images of a qubit loop with one stack pair, showing the completed structure after the three main process steps. The structures correspond to the design shown in Fig. 6.2 (a)–(d), but with one stack pair.

links between stacks, the straight links were fabricated first, followed by a separate process step to form the arch-type links connecting the ground planes.

After fabrication, the wafers were diced into $5 \times 5\,\mathrm{mm}^2$ samples (compare Fig. 6.1 (c)), followed by solvent stripping and oxygen plasma cleaning. Finally, the chips were mounted in sample holders, wire-bonded to the microwave circuit board and waveguides, and cooled down in a dilution refrigerator for characterization.

Table 6.1: Fabrication parameters of the devices listed in Table 6.2. A_{stack} is the stack footprint, N the junction number in the array, $p_{\mathrm{ox,JA}}$ the oxidation pressure used for stack junctions, w_{J} the width of the small-junction electrodes, and $p_{\mathrm{ox,J}}$ the oxidation pressure used for the small-junction.

Devices	A_{stack} (µm^2)	N	$p_{\mathrm{ox,JA}}$ (mbar)	w_{J} (nm)	$p_{\mathrm{ox,J}}$ (mbar)
S-A1, S-A2, S-A3, S-B1, S-B2, S-C1, S-C2	0.8	32	0.75	140	3.5
S-D1, S-D2, S-D3, S-E1	0.8	16	0.75	235	3.5
L-A1, L-A2, L-A3, L-A4	4.0	48	6.0	200	0.3
L-B1, L-B2, L-B3, L-B4	4.0	32	6.0	200	0.3
L-C1, L-C2, L-C3	4.0	32	7.0	160	5.0
L-D1	4.0	16	6.0	225	0.15
L-E1	4.0	16	7.0	230	3.0

6.3 Investigation of the quarton spectrum

In this section, the focus is on measurements of the flux-dependent energy spectrum of quarton qubits, while time-domain measurements are discussed separately in Sec. 6.4. The qubit transition frequencies were determined by two-tone microwave spectroscopy (see Secs. 3.2.2 and 3.4.5), where a continuous-wave tone probes the readout resonator frequency and a second microwave tone is swept across a wide frequency range to excite the qubit. The qubit state is inferred from the dispersive shift of the resonator frequency.

Figure 6.4 shows a representative two-tone spectroscopy measurement of a quarton qubit with 4×8 stacked junctions. Panel (a) displays the resonator signal as a function of flux bias (horizontal axis) and drive frequency (vertical axis). A pronounced modulation with period Φ_0 is observed, with a minimum of the qubit transition frequency at half-flux bias and a maximum near zero flux, characteristic of flux-type qubits. The colored data points in panel (b) give the extracted qubit transition frequencies obtained from the dips or peaks in the resonator response. The red dots correspond to the fundamental transition f_{01}, which tunes from about 7.0 GHz at zero flux bias to 3.2 GHz at half-flux bias. At higher drive powers, additional transitions involving the second excited state become visible: the f_{12} transition (green triangles) and the two-photon transition $f_{02}/2$ (blue diamonds), where two photons of nearly equal energy excite the system.

The transition frequencies in Fig. 6.4 (b) were fitted to the eigenenergies of the flux-qubit Hamiltonian defined by E_C, E_J, and E_L in Eq. (3.48), as discussed in Sec. 3.4.2. The fits were performed using the simulation package `scqubits` [176] and reproduce the measured transitions over one flux quantum Φ_0. The extracted parameters are $E_C = 0.8\,\text{GHz}$, $E_L = 4.3\,\text{GHz}$, and $E_J = 4.2\,\text{GHz}$. This corresponds to a ratio $E_L/E_J = \gamma/N \approx 1.02$, at which the qubit potential becomes quartic at $\Phi_0/2$ flux bias. The corresponding potential and wavefunctions at half-flux bias, calculated for these parameters, are shown in Fig. 3.8 in Sec. 3.4.2. The anharmonicity versus flux bias is plotted in Fig. 6.4 (c). The anharmonicity reaches its maximum value at half-flux bias, $\mathcal{A} \approx 0.9\,\text{GHz}$, which is approximately one third of the qubit frequency. Away from the half-flux bias point, $\mathcal{A}$ decreases and changes sign around $0.4\,\Phi_0$ and $0.6\,\Phi_0$ and reaches negative minima of about $-0.6\,\text{GHz}$ near $0.3\,\Phi_0$ and $0.7\,\Phi_0$. Positive anharmonicity is generally advantageous for qubit operation (suppression of excitation leakage to higher energy levels), while negative anharmonicity can be exploited in specific contexts such as multi-level dynamics or tunable couplers [4, 14, 177].

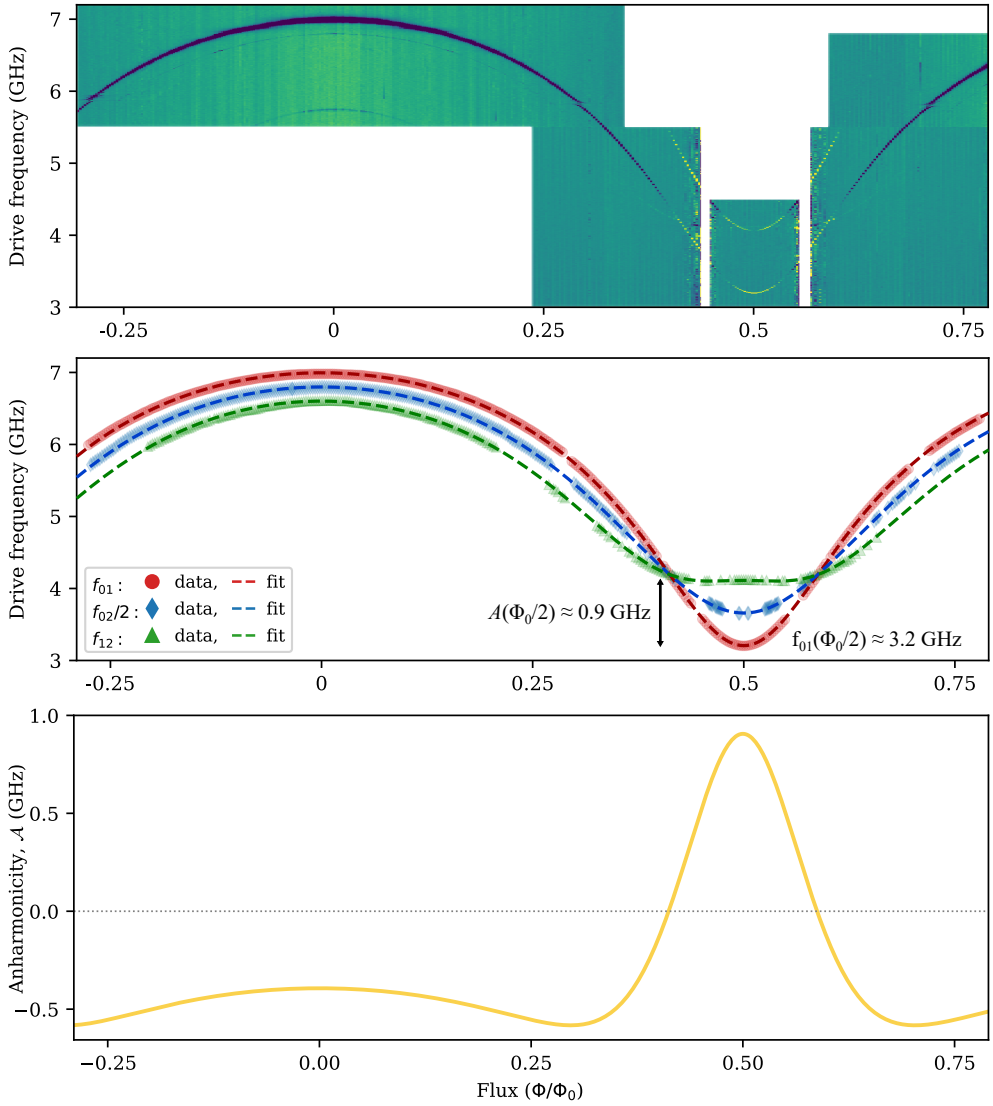

Figure 6.4: Two-tone spectroscopy of a quarton qubit. (a) Measured readout resonator signal (phase) as a function of applied flux and drive frequency. The readout frequency was calibrated for each flux bias value with f_r around 7.8 GHz. (b) Extracted transition frequencies together with a numerical fit to the flux-qubit Hamiltonian. The data points correspond to the qubit transitions f_{01} (red dots), f_{12} (green triangles), and the two-photon transition $f_{02}/2$ (blue diamonds). (c) Anharmonicity $\mathcal{A} = f_{12} - f_{01}$ calculated from the fits.

After discussing the spectroscopy data of one representative device, we now compare the spectroscopy results of all measured qubits. To assess how precisely the inductive energy of stacked-junction arrays can be controlled, we fabricated and characterized more than twenty quarton qubits with systematically varied array geometries. The stack footprint and the array length N were adjusted to tune the inductive energy E_L, while the Josephson energy E_J of the small-junction was scaled accordingly to target $\gamma/N \approx 1$ across all designs (see Table 6.2 for device parameters).

Figure 6.5 summarizes the qubit properties measured at half-flux bias as a function of the inductive energy ratio γ/N, obtained from fits to the measured spectra. The qubit frequency at half-flux bias increases approximately linearly with γ/N, despite fabrication-induced scatter. The relative anharmonicity A/f_{01} collapses onto a single curve following a power-law dependence, yielding $A/f_{01} \approx 0.31$ at $\gamma/N = 1$, in agreement with the expected behavior of quarton qubits [4]. These results demonstrate that stacked-junction inductors enable predictable and reproducible tuning of the inductive energy using only the stack footprint and array length. Typical qubit frequencies of the stacked junction quarton qubits are between 3 and 5 GHz, and the anharmonicities between 0.5 and 1.5 GHz.

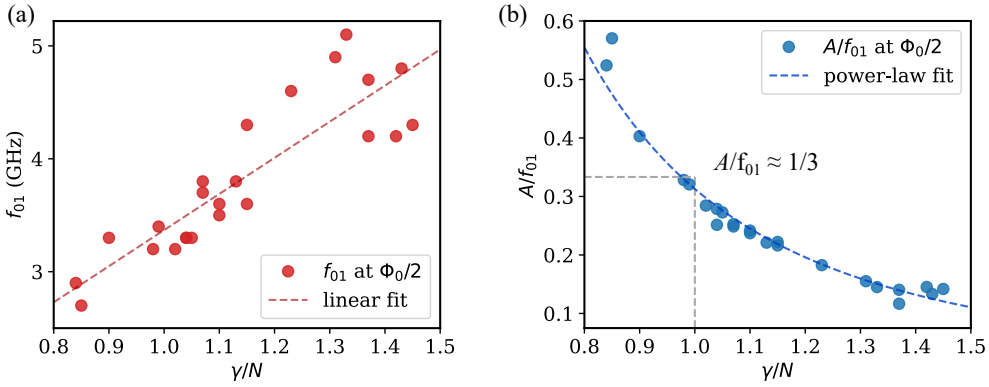

Figure 6.5: Qubit frequency and relative anharmonicity versus the inductive energy ratio. The ratio $\gamma/N = E_L/E_J$ is extracted from spectral fits for each device. (a) Qubit frequency f_{01} at half-flux bias versus γ/N. Despite fabrication-induced scatter, f_{01} follows an approximately linear trend (dashed line). (b) Relative anharmonicity A/f_{01} at half-flux bias versus γ/N. The dashed curve shows a power-law fit, $A/f_{01} = a(\gamma/N)^b$, yielding $A/f_{01} \approx 0.31$ at $\gamma/N = 1$, consistent with the expected scaling (Sec. 3.4.4). Data points correspond to the devices listed in Table 6.2.

Table 6.2: Spectroscopy and time-domain measurement results of quarton qubits. The table lists the array design parameter (stack footprint A_{stack} and number of junctions N), the circuit parameter extracted from fits to the spectra (γ/N, small-junction critical current I_c, array inductance L_{JA}, and circuit capacitance C_Σ), as well as the transition frequency f_{01}, anharmonicity $A = f_{12} - f_{01}$, and coherence times measured at half-flux bias. The coherence times T_1, T_2^*, and $T_{2\,\text{Echo}}$ are included for reference and discussed in detail in Sec. 6.4. Midrules separate devices fabricated on different wafers, which differ in design and process parameters summarized in Table 6.1.

device	A_{stack} (μm^2)	N	γ/N	I_c (nA)	L_{JA} (nH)	C_Σ (fF)	f_{01} (GHz)	$\mathcal{A}$ (GHz)	T_1 (μs)	T_2^* (μs)	$T_{2\,\text{Echo}}$ (μs)	comment
S-A1	0.8	32	1.02	9	38	24	3.2	0.91	17.6±2.0	4.9±0.6	10.6±1.3	v9C34-q1
S-A2	0.8	32	1.04	8	38	23	3.3	0.83	17.3±3.1	4.1±0.3	10.7±1.1	v9C34-q2
S-A3	0.8	32	1.10	8	33	24	3.6	0.87	15.2±1.6	1.2±0.1	5.1±0.4	v9C34-q3
S-B1	0.8	32	1.45	8	30	24	4.3	0.61	7.8±2.0	0.6±0.2	0.6±1.0	v9C15-q3
S-B2	0.8	32	1.42	8	29	25	4.2	0.61	9.6±1.2	1.3±0.1	3.9±1.2	v9C15-q4
S-C1	0.8	32	1.15	9	33	24	3.6	0.80	11.1±1.3	5.6	11.0±1.6	v9C17-q1
S-C2	0.8	32	1.10	9	34	25	3.5	0.83	15.5±1.3	3.2±0.5	13.2±0.4	v9C17-q2
S-D1	0.8	16	1.23	15	18	27	4.6	0.84	13.6±2.0	1.3±0.2	1.5±0.1	v9C42-q1
S-D2	0.8	16	1.31	16	16	28	4.9	0.76	8.3±0.5	3.7±1.0	10.2±1.0	v9C42-q2
S-D3	0.8	16	1.33	17	15	28	5.1	0.74	6.3±0.5	0.4±0.02	1.1±0.1	v9C42-q3
S-E1	0.8	16	1.15	14	20	25	4.3	0.93	2.0±0.3	0.7±0.1	1.5±0.4	v9C15-q2
L-A1	4.0	48	1.07	14	21	28	3.8	0.96	2.0±0.2	–	–	v7C17-q1
L-A2	4.0	48	1.37	14	17	29	4.7	0.66	0.8±0.1	0.4±0.1	1.2±0.2	v7C17-q2
L-A3	4.0	48	0.84	19	21	28	2.9	1.52	1.4±0.3	0.7±0.3	1.1±0.7	v7C17-q3
L-A4	4.0	48	0.90	18	20	28	3.3	1.33	0.8±0.1	0.7±0.1	1.4±0.1	v7C17-q4
L-B1	4.0	32	0.99	20	16	33	3.4	1.09	1.4±0.2	1.0±0.1	1.3±0.1	v7C31-q1
L-B2	4.0	32	1.07	18	17	33	3.7	0.92	1.1±0.2	0.3±0.1	0.4±0.1	v7C31-q2
L-B3	4.0	32	1.13	17	15	33	3.8	0.84	1.1±0.1	0.6±0.1	1.0±0.03	v7C31-q3
L-B4	4.0	32	0.98	19	18	34	3.2	1.05	3.8±0.2	–	0.1	v7C31-q4
L-C1	4.0	32	1.05	11	28	30	3.3	0.90	2.2±0.4	0.6	0.6	v8C24-q1
L-C2	4.0	32	1.04	11	28	29	3.3	0.92	3.1±0.5	1.7±0.2	2.6±0.4	v8C24-q3
L-C3	4.0	32	1.43	11	21	26	3.2	0.64	0.9±0.1	0.7±0.1	1.5±0.3	v8C24-q4
L-D1	4.0	16	1.37	22	11	38	4.2	0.49	2.2±0.1	1.7±0.1	2.9±0.2	v6C10-q1
L-E1	4.0	16	0.85	29	13	36	2.7	1.54	2.4	0.6	–	v8C10-q2

6.4 Decoherence versus stack footprint

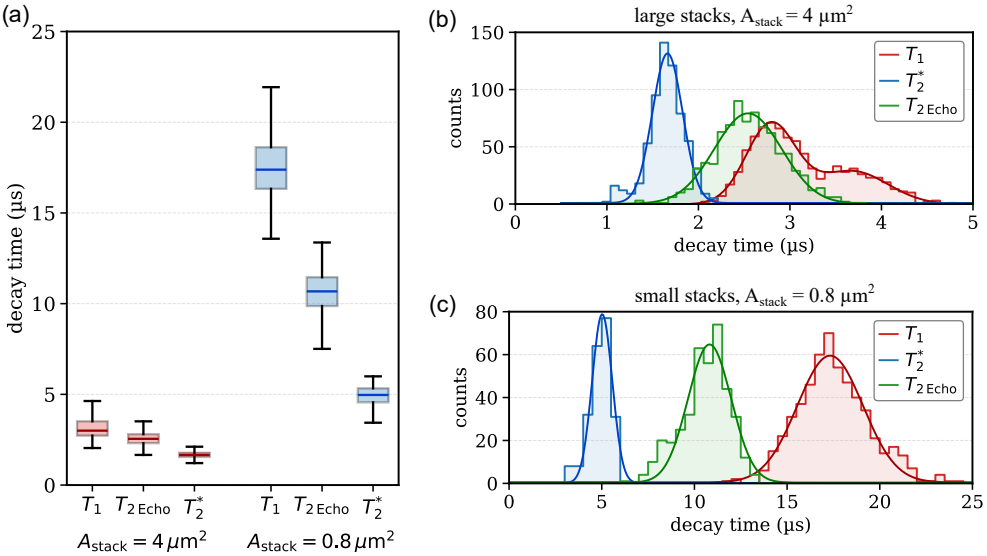

Figure 6.6: Coherence times of quarton qubits with small and large stack footprints. (a) Boxplots and (b,c) histograms show the distributions of relaxation and dephasing times for two qubits, *S-A1* ($A_{\mathrm{stack}} = 0.8\,\mu\mathrm{m}^2$) and *L-C2* ($A_{\mathrm{stack}} = 4.0\,\mu\mathrm{m}^2$), measured in the same cooldown under similar conditions and sharing an identical array length $N = 32$ (Table 6.2). The small-stack qubit shows typical T_1 around 18 µs and up to ≈ 24 µs at best, whereas the large-stack qubit is limited in T_1 to about 3 µs, with an upper bound near 5 µs.

To assess the influence of the stacked-junction inductor on qubit coherence, we performed time-domain experiments on devices with different stack footprints A_{stack} and array lengths N. The experimental pulse sequences and analysis procedures for extracting the coherence times T_1, T_2^*, and $T_{2\,\mathrm{Echo}}$ follow the methodology introduced in Sec. 3.2.3. Representative single measurements for one device are shown in Fig. 3.4. The measurement setup is described in Secs. 4.1 and 4.2.

To illustrate the characteristic dependence of coherence on the stack footprint, Fig. 6.6 compares two devices that are nearly identical in qubit properties and circuit parameters ($N = 32$, $\gamma/N \approx 1$, $f_{01} \approx 3.2$–$3.3\,\mathrm{GHz}$, $\mathcal{A} \approx 0.9\,\mathrm{GHz}$), but differ in the stack footprint. Device *S-A1* employs small stacks with $A_{\mathrm{stack}} = 0.8\,\mu\mathrm{m}^2$, whereas device *L-C2* features large stacks with $A_{\mathrm{stack}} = 4.0\,\mu\mathrm{m}^2$. The difference in the size of the coherence times is pronounced: the small-stack device reaches T_1 values around 18 µs, whereas the large-stack device is limited to about 3 µs. The Ramsey and spin-echo dephasing times scale similarly with T_1 for both devices.

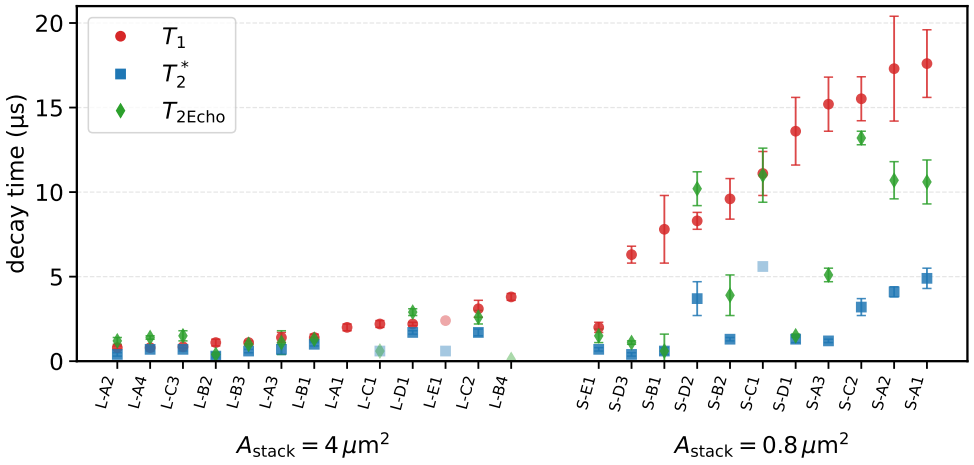

Figure 6.7: Coherence times versus stack footprint. Mean and standard deviation (error bars) of T_1 (circles), T_2^* (squares), and $T_{2\,\mathrm{Echo}}$ (diamonds) for all devices in Table 6.2, grouped by footprint A_{stack} (4 µm^2 vs. 0.8 µm^2) and sorted by T_1 within each group. The small-stack group reaches mean $T_1 \sim 10$ µs with best cases ~ 20 µs, whereas large stacks are limited to ~ 2 µs.

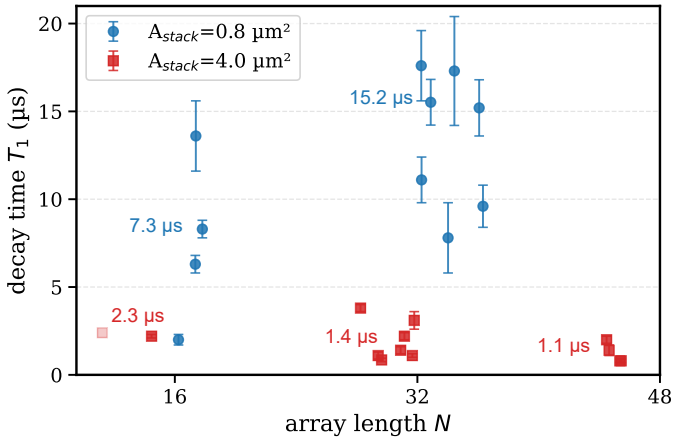

Figure 6.8: Relaxation time versus array length. Data points and error bars denote the mean and standard deviation of T_1 for each device and are jittered around $N = 16$, 32, and 48. The numbers indicate the median T_1 for each group.

Figure 6.7 compares the coherence times (dephasing and T_1) of all devices, grouped by footprint and sorted by T_1, while Fig. 6.8 shows the T_1 values grouped by stack footprint and array length. Across all small-stack qubits ($A_{\mathrm{stack}} = 0.8\,\mu\mathrm{m}^2$), typical T_1 values are around 10 µs, with mean T_1 values reaching up to $\sim$ 20 µs,

consistent with previously reported quarton qubits.[2] Within the small-stack devices, increasing the array length from $N = 16$ to $N = 32$ leads to a shift of the median T_1 from approximately 7 µs to about 15 µs, as shown in Fig. 6.8. In contrast, large-stack devices ($A_{\text{stack}} = 4.0\,\mu\text{m}^2$) exhibit substantially shorter relaxation times, with typical $T_1 \approx 2\,\mu\text{s}$ and best-case values near 5 µs, independent of array length. For both stack footprints, several devices show $T_{2\,\text{Echo}}$ values approaching T_1 (e.g., *S-C2* and *L-D1*), yet remaining below the $T_{2\,\text{Echo}} = 2\,T_1$ limit (compare with Eq. (3.17)).

Additional correlations with the inductive energy ratio are presented in Appendix B. Figure B.1 shows T_1 and $T_{2\,\text{Echo}}/T_1$ versus γ/N, confirming the absence of a systematic dependence on γ/N.

6.5 Investigation of external flux noise using a persistent-current bias

The results of the previous section raise the question of which mechanisms limit the coherence of the quarton qubits investigated in this work. A prominent decoherence channel in flux qubits is external flux noise. In this section, we therefore study the sensitivity of the quarton qubits to flux noise using a persistent-current bias scheme. First, the operating principle of the persistent-current bias is introduced. Second, the bias-setting precision and long-term stability are experimentally benchmarked. Finally, the impact of external flux noise on the qubit coherence is assessed.
The results presented in this section are part of a manuscript in preparation [179].

6.5.1 Operating principle and trapping sequence

Flux qubits must be operated at certain magnetic flux bias points to reveal their characteristic properties. In quarton qubits, the longest coherence times are typically obtained at the half-flux bias point, where the qubit frequency is first-order insensitive to flux noise. Maintaining this operating point with high precision and long-term stability is therefore essential for coherent qubit operation, as even small bias fluctuations lead to dephasing and frequency instability (see Sec. 3.3.2).

In conventional experimental setups, the flux bias is applied by driving a DC current through a bias coil that is inductively coupled to the qubit loop. This

[2] The measured coherence times fall within the broader range observed for superconducting qubits operating in the *quarton regime*, such as the devices in Ref. [4, 178].

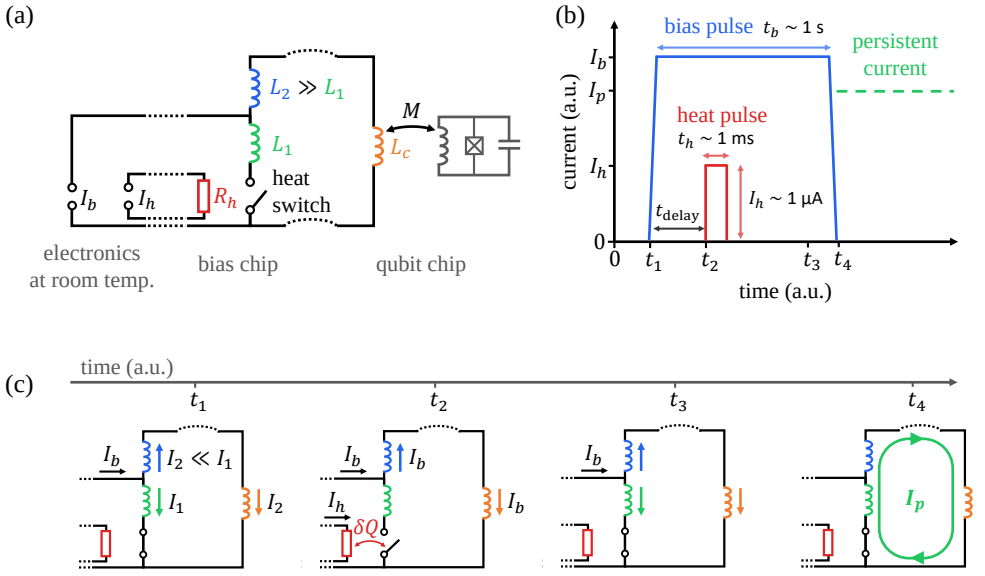

Figure 6.9: Circuit and pulse sequence used to trap a persistent current. (a) Circuit diagram of the superconducting circuit formed by L_1, L_2, and the qubit bias coil L_c, including a local heat switch. Dashed lines indicate wire bonds connecting the bias chip to the qubit chip and to the DC wiring leading to room-temperature electronics, highlighting that the circuit is distributed across multiple physical components. (b) Pulse sequence to trap a persistent current I_p (not to scale). (c) Four-step trapping mechanism and current partitioning before and after closing the loop. After the loop is reclosed, flux quantization constrains the magnetic flux linked to the inductive network to remain constant, leading to the expression for I_p in Eq. (6.4).

current is typically supplied by a current source or digital-to-analog converter (DAC) located at room temperature. As a representative example, the DAC output used in this work exhibits noise levels of 50–100 $\text{nV}/\sqrt{\text{Hz}}$ at 1 Hz [180], resulting in a flux-noise amplitude of $S_\Phi^{1/2} \sim 5 \times 10^{-8}\, \Phi_0/\sqrt{\text{Hz}}$. This value is within one order of magnitude of the intrinsic $1/f$ flux-noise levels reported for superconducting circuits [38, 39, 125, 126]. More generally, any wiring to room-temperature bias electronics provides a direct pathway for current fluctuations to couple into the qubit. Any fluctuation on this line—including thermal noise, low-frequency $1/f$ noise, electromagnetic pickup, or slow drifts of the voltage reference—is directly converted into flux noise in the qubit through the mutual inductance [38, 125, 181–185]. Even in carefully filtered lines, these noise sources introduce residual bias instability, which limits coherence in flux-type qubits [186, 187].

A conceptually different approach to continuous current biasing that avoids a permanent connection to room-temperature electronics is based on *persistent currents* stored in closed superconducting loops. As discussed in Sec. 2.1.3, flux quantiza-

tion constrains the magnetic flux enclosed by a superconducting loop to integer multiples of Φ_0, allowing a circulating supercurrent to persist for long times. Persistent-mode operation is widely used in precision magnet technology [188] and in low-noise sensor systems employing persistent-current switches [189, 190].

In the context of superconducting qubits, several on-chip implementations of persistent-current biasing have been demonstrated, including flux trapping in unshunted rf-SQUID loops [186], persistent-current shunts with local heaters [187], and gradiometric locking to flux-insensitive operating points [191]. While differing in implementation, these approaches share the common principle of storing the flux bias in a superconducting loop.

In this work, persistent-current biasing is realized by connecting an auxiliary superconducting bias circuit to the local flux-bias coil of the qubit through wire-bonds. Together, they form a closed superconducting circuit that allows controlled initialization and re-trapping of a flux bias at millikelvin temperatures without modifying the qubit layout. This circuit is depicted in Fig. 6.9 (a) and consists of two inductors, L_1 and L_2, and a local heat-based switch, while the on-chip bias coil of inductance L_c resides on the qubit chip (bond-wire inductances are neglected).

Initialization of the persistent current follows the pulse sequence shown in Fig. 6.9(b,c). A bias current I_b is applied, after which a short heat pulse drives the switch normal and temporarily opens the loop at the branch of L_1. During this phase, the bias current flows only through the remaining superconducting branch. After the heater is turned off, the L_1 branch becomes superconducting again and the loop closes while the bias current is still applied. Flux quantization in the closed superconducting loop constrains the system to retain the flux state established during the open configuration. At this stage (t_3), the loop therefore carries a flux $\Phi_{t_3} = (L_2 + L_\mathrm{c})I_\mathrm{b}$. When the external bias current is subsequently turned off, this flux is preserved and is carried by a circulating persistent current I_p in the closed loop, $\Phi_{t_4} = (L_1 + L_2 + L_\mathrm{c})I_\mathrm{p} = \Phi_{t_3}$. This yields

$$I_\mathrm{p} = \frac{L_2 + L_\mathrm{c}}{L_1 + L_2 + L_\mathrm{c}} I_\mathrm{b}. \tag{6.4}$$

The qubit experiences a stable and low-noise flux bias via the mutual inductance M between the local bias coil and the qubit loop.

Before trapping, low-frequency current fluctuations in I_b partition between the parallel inductive branches. As a result, only a fraction

$$I_2 = \frac{L_1}{L_1 + L_2 + L_\mathrm{c}} I_\mathrm{b} \quad \xrightarrow{L_2 \gg L_1, L_\mathrm{c}} \quad I_2 \approx \frac{L_1}{L_2} I_\mathrm{b} \tag{6.5}$$

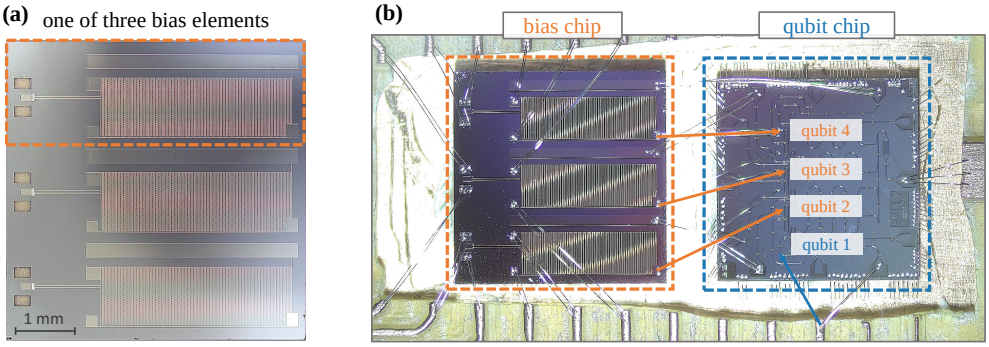

Figure 6.10: Experimental implementation of the bias circuit. (a) Optical micrograph of the bias chip ($5 \times 5\,\mathrm{mm}^2$) containing three identical bias circuits. (b) Photograph of the two-chip assembly (bias chip and qubit chip) connected by superconducting wire bonds.

flows through the branch at the qubit. If required, a small DC bias can still be superimposed on I_p, benefiting from the same current divider. After trapping, the current source may be fully disconnected, eliminating current-source noise.

6.5.2 Experimental implementation

Figure 6.10 shows the experimental implementation of the auxiliary bias circuit used for persistent-current trapping. A separate chip hosting three identical bias circuits on silicon substrate is mounted next to the qubit chip on a sample holder and connected via superconducting Al wire bonds (diameter 25 µm, typically two in parallel per pad, length of a few millimeters). Together with the on-chip bias coil L_c on the qubit chip, two wire-bond connections per bias circuit form the superconducting loop (L_1, L_2, L_c) described in Sec. 6.5.1. In the experiment, three of the four quarton qubits (*qubits 2–4*) are connected to auxiliary bias circuits. The remaining device, *qubit 1*, is directly biased via a DC source at room temperature and serves as a benchmark reference. All four devices are quarton qubits with small-stack junction arrays ($A_\mathrm{stack} = 0.8\,\mu\mathrm{m}^2$).

The bias circuit is designed with a strong inductance asymmetry. The small inductor L_1 has a design inductance of approximately 11 nH, while the large inductor L_2 provides about 120 nH, corresponding to a design ratio $L_2/L_1 \approx 11$.

The bias current I_b enters through a bond-wire at the junction of the two inductive branches and splits between the L_2 branch (towards the qubit chip) and the L_1 branch (towards the heat-switch region). A second pair of pads addresses the on-chip heater.

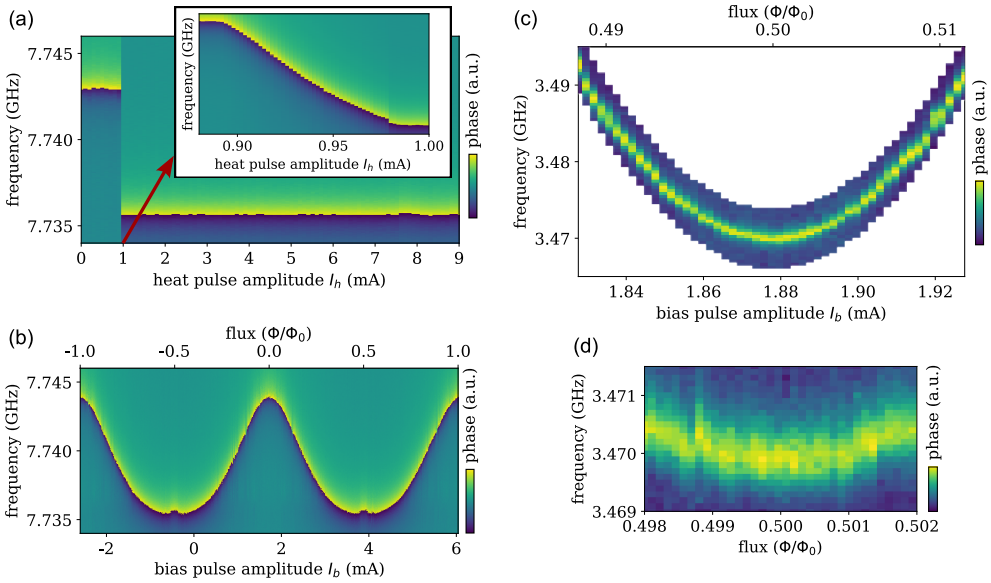

Figure 6.11: Readout resonator and qubit spectroscopy with trapped flux at *qubit 2*. (a) Heat pulse calibration. The resonator frequency shifts with increasing heat pulse amplitude I_h until the L_1 branch becomes fully normal conducting and the trapped flux saturates. The inset shows a magnified view of the transition region. (b) Resonator response versus bias pulse amplitude I_b (top axis: flux bias Φ/Φ_0 induced in the qubit loop). The smooth periodic modulation over several flux quanta demonstrates precise control of the persistent current. Small periodic deviations near half-flux bias originate from qubit–resonator interactions and are not artifacts of the trapping protocol. (c),(d) Qubit spectroscopy versus trapped flux, shown over a wide flux range and as a high-resolution zoom around half-flux bias. The qubit transition frequency f_{01} follows a smooth and continuous dispersion and no back-action of applied heat pulses on the qubit is observed.

6.5.3 Bias-setting precision

The aim of this subsection is to quantify how precisely a desired flux bias can be set. The pulse sequence, illustrated in Fig. 6.9, is characterized by five parameters: the heat pulse amplitude and duration $(I_\mathrm{h}, t_\mathrm{h})$, the bias amplitude and duration $(I_\mathrm{b}, t_\mathrm{b})$, and a relative delay t_delay between the two pulses. Short, high-amplitude heat pulses are preferred, as they help to confine dissipation and reduce heating of the surrounding chip volume [68, 192]. Accordingly, the heat pulse duration is fixed to $t_\mathrm{h} \approx 2$–$3\,\mathrm{ms}$ and only the amplitude I_h is varied during calibration. The remaining timing parameters are chosen conservatively to ensure reliable operation. We use a fixed delay of $t_\mathrm{delay} \approx 0.5\,\mathrm{s}$, such that the bias pulse has reached its full amplitude before the heater is activated, and a bias duration of $t_\mathrm{b} = 3\,\mathrm{s}$, which guarantees that the L_1 branch has fully recovered its superconducting state before the bias pulse ends.

Via dispersive qubit–resonator coupling, changes in the qubit flux with a persistent-current bias — and thus in its transition frequency — are directly mapped onto shifts of the resonator frequency. We therefore calibrate the heat pulse by applying the pulse scheme with fixed (I_b, t_b, t_h) and varying I_h, using the resonator frequency as a proxy for the trapped flux. Figure 6.11 (a) shows the resonator frequency as a function of I_h. For small heater amplitudes, no frequency shift is observed, indicating that the L_1 branch remains superconducting. Above a well-defined threshold, the resonator frequency abruptly saturates at a new value, signaling complete trapping of the flux associated with I_b. A narrow transition region separates these two regimes, where the trapped current increases continuously with I_h. This behavior is attributed to incomplete switching of the L_1 branch, either due to marginal heating above T_c or insufficient opening time. All experiments are therefore performed in the saturated plateau regime, where flux trapping is complete and robust against small drifts in heater amplitude. The calibrated pulse parameters are summarized in Table 6.3. All bias circuits operate at similar heater thresholds, with sub-microjoule dissipation per pulse that is small compared to the micro-watt cooling power of the dilution refrigerator at millikelvin temperatures (Sec. 4.1).

Table 6.3: Pulse parameter. Listed are the calibrated heat pulse amplitude I_h and duration t_h, the effective mutual inductance I_b/Φ extracted as, e.g., from Fig. 6.11 (b), and the estimated heat dissipated per pulse $\Delta Q \approx R_h I_h^2 t_h$.

bias element (qubit)	I_h (mA)	t_h (ms)	I_b/Φ (mA/Φ_0)	ΔQ (µJ)
qubit 2	0.99	2.50	4.37	0.2
qubit 3	1.28	2.75	4.28	0.3
qubit 4	1.60	2.75	3.66	0.5

Using the calibrated pulse parameters, we sweep the bias amplitude I_b and record the resonator frequency as a function of the trapped flux, shown in Fig. 6.11 (b). The resulting periodic modulation extends over several flux quanta and remains smooth and reproducible, demonstrating precise and reliable control of the persistent current. The extracted effective mutual inductances I_b/Φ are listed in Table 6.3. The measurements were performed using approximately 1600 consecutive trapping sequences within about 30 min. Despite repeatedly introducing heat close to the qubit, no distortions, hysteresis, or drifts are observed in the resonator response, and no increase in temperature was detected. This demonstrates that the trapping protocol allows frequent and rapid bias re-setting without measurable thermal back-action on the qubit.

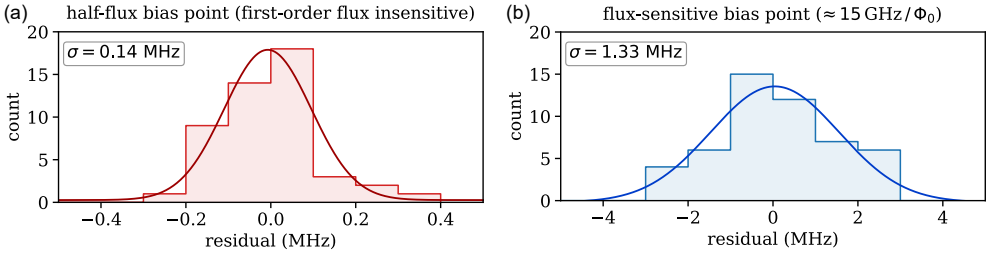

Figure 6.12: Flux-bias-setting uncertainty under repeated trapping cycles. Histograms of residual deviations of the measured qubit transition frequency f_{01} from the median value, obtained from 50 repeated trapping cycles: (a) at half-flux bias, where the qubit frequency is first-order flux-insensitive, the distribution is below the intrinsic transition linewidth, and (b) at $\Phi \approx 0.41\,\Phi_0$, where the qubit frequency is strongly flux-sensitive, yielding a Gaussian width of $\sigma \gtrsim 1\,\mathrm{MHz}$.

As a more sensitive probe, we perform high-resolution two-tone spectroscopy of *qubit 2* as a function of trapped flux. The qubit transition frequency f_{01} follows a smooth and artifact-free dispersion shown in Fig. 6.11 (c)–(d), indistinguishable from spectra obtained using a conventional DC current source. No jumps, discontinuities, or anomalous features were observed, confirming that precise flux biasing via persistent-current trapping does not introduce detectable heat-induced perturbations to the qubit.

Precise flux biasing requires that repeated trapping cycles reproducibly establish the same persistent current. To quantify the bias-setting uncertainty, we repeatedly execute the trapping sequence at fixed bias amplitude I_b and fixed pulse parameters $(I_\mathrm{h}, t_\mathrm{h}, t_\mathrm{b})$, and measure the resulting qubit transition frequency f_{01}. Each cycle consists of trapping the persistent current, performing two-tone spectroscopy to extract f_{01}, and resetting the bias to remove any previously stored flux.

From the extracted transition frequencies, we compute residuals with respect to the median value, $r_i = f_{01}^{(i)} - \mathrm{median}(f_{01})$, and construct histograms of these deviations. A Gaussian fit yields the standard deviation σ, which we use as a quantitative measure of flux-bias-setting precision (Fig. 6.12). Measurements are performed at two representative bias points of *qubit 2*: at half-flux bias and bias point ($\Phi \approx 0.41\,\Phi_0$), where the qubit frequency is strongly flux-sensitive with $\mathrm{d}f_{01}/\mathrm{d}\Phi \approx 15\,\mathrm{GHz}/\Phi_0$.

At half-flux bias, the distribution is narrow, with $\sigma \approx 0.1\,\mathrm{MHz}$, well below the intrinsic transition linewidth of approximately 1 MHz. We therefore attribute this value to the finite resolution of the spectroscopy rather than to fluctuations of the trapped bias. At the flux-sensitive point, the spread increases to $\sigma \gtrsim 1\,\mathrm{MHz}$. Using the measured slope $\mathrm{d}f_{01}/\mathrm{d}\Phi$, this corresponds to a flux uncertainty of

$\delta\Phi \approx 9 \times 10^{-5}\,\Phi_0$, which translates—via the effective mutual inductances listed in Table 6.3—to a bias-current uncertainty of approximately 0.4 µA.

6.5.4 Long-term stability

A persistent-current bias is only useful if the trapped flux remains stable over extended periods of time without inducing frequency drift or degrading qubit coherence. We therefore investigate the long-term stability of a trapped half-flux bias over a period of one week.

After trapping *qubit 2* at $\Phi_0/2$, the DC source was disconnected so that the device was biased exclusively by the persistent current. At three time points—immediately after trapping ($t = 0$ h), after 61 h, and after 162 h ($\approx$ one week)—we measured the qubit transition frequency f_{01} as well as the coherence times T_1, T_2^*, and $T_{2\,\mathrm{Echo}}$. The transition frequency was extracted from a Rabi–detuning measurement (Sec. 3.2.2). All results are summarized in Table 6.4.

Within the full measurement interval, neither the qubit frequency nor the coherence times show any systematic drift. The observed variations are consistent with statistical scatter and do not indicate a change in the underlying flux bias. This conclusion is supported by the strong flux sensitivity of the qubit away from the half-flux bias. Already at $\Phi = 0.496\,\Phi_0$, where $\mathrm{d}f_{01}/\mathrm{d}\Phi \approx 1\,\mathrm{GHz}/\Phi_0$, control measurements show strongly reduced coherence times ($T_1 \approx 6.3$ µs, $T_2^* \approx 0.6$ µs, $T_{2\,\mathrm{Echo}} \approx 3.5$ µs). The absence of any comparable degradation in Table 6.4, together with the observed spread of f_{01} of ~ 1.3 MHz, implies that the trapped flux remained within $\lesssim 10^{-3}\,\Phi_0$ of the half-flux bias point over the entire week.

After one week, the persistent current was intentionally released using a reset pulse, confirming that the loop had remained in the trapped state throughout the experiment. Overall, these results demonstrate that the trapped flux bias is stable for at least one week without degrading qubit coherence.

Table 6.4: Long-term stability of the persistent-current bias. Qubit frequency f_{01}, and mean and standard deviation of T_1, T_2^*, $T_{2\,\mathrm{Echo}}$ of *qubit 2* at three times after trapping. Each coherence time is obtained from 50–100 repeated measurements.

Time (h)	f_{01} (GHz)	T_1 (µs)	T_2^* (µs)	$T_{2\,\mathrm{Echo}}$ (µs)
0	3.3855	14.4 ± 1.3	2.20 ± 0.08	10.5 ± 0.8
61	3.3857	15.6 ± 0.9	2.42 ± 0.06	13.2 ± 0.5
162	3.3842	14.8 ± 0.9	2.35 ± 0.04	9.9 ± 1.0

6.5.5 Impact on qubit coherence

After benchmarking the precision and long-term stability of the persistent-current bias method, we return to the central question of this chapter: what ultimately limits the coherence of quarton qubits. In particular, we investigate whether biasing quarton qubits with a persistent current leads to improved coherence.

To address this question, we directly compare the coherence properties of two nominally identical quarton qubits located on the same chip and measured consecutively in the same cooldown. The two devices correspond to *qubit 1* (*S-C1*), which is biased through a conventional room-temperature DC line connected to its local flux coil L_c, and *qubit 2* (*S-C2*), which is biased exclusively via a trapped persistent current. Both qubits share the same design parameters ($A_{\text{stack}} = 0.8\,\mu\text{m}^2$, $N = 32$) and exhibit very similar qubit frequencies, anharmonicity, and inductive ratios ($\gamma/N \approx 1.1$) at half-flux bias (see Table 6.2).

The measured qubit frequencies and coherence times at half-flux bias are summarized in Table 6.5. The qubit biased via a trapped persistent current exhibits coherence times that are comparable to, and in T_1 as well as $T_{2\,\text{Echo}}$ slightly higher than, those obtained with conventional DC biasing. However, the observed coherence times are consistent with those of other devices sharing the same junction stack footprint and array length (Table 6.2), which rules out external flux noise as the dominant limitation of coherence in the quarton qubits.

In the following section, we therefore turn to the qubit spectra and coherence behavior to identify alternative decoherence mechanisms.

6.6 TLS-induced decoherence in junction stacks

Section 6.4 revealed a pronounced dependence of qubit coherence on the junction stack footprint A_{stack}, with larger stacks exhibiting systematically shorter T_1 times.

Table 6.5: Comparison of DC-biased and trapped-flux-biased quarton qubits. Qubit frequencies and coherence times measured at half-flux bias for two identical devices measured consecutively in the same cooldown.

device	f_{01} (GHz)	T_1 (µs)	T_2^* (µs)	$T_{2\,\text{Echo}}$ (µs)
qubit 1 (DAC bias)	3.62	11.1 ± 1.3	≈ 5.6	11.0 ± 1.6
qubit 2 (persistent current)	3.46	15.5 ± 1.3	3.2 ± 0.5	13.2 ± 0.4

This behavior points toward coupling to microscopic two-level systems (TLS) in the tunnel barriers. To elucidate this mechanism, we analyze high-resolution qubit spectra for signatures of TLS coupling in the form of avoided level crossings. By comparing devices with different stack footprints, we extract TLS densities from splitting size distributions and use these densities to estimate the resulting coherence limitations of stacked-junction quarton qubits.
The results in this section are based on the manuscript in preparation [193].

6.6.1 Avoided level crossings in the spectrum

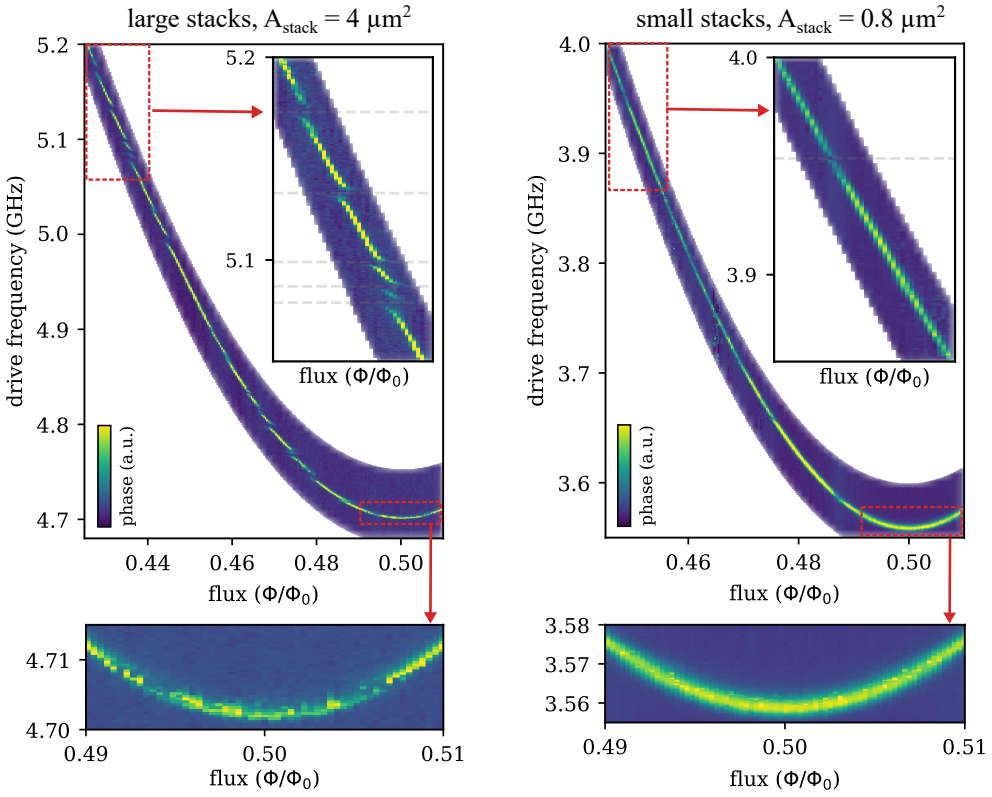

Figure 6.13: TLS-qubit avoided level crossings in quarton qubit spectra. High-resolution two-tone spectroscopy around half-flux bias for two quarton qubits: (left) device with large stacks ($A_{\text{stack}} = 4.0\,\mu\text{m}^2$) versus (right) device with small stacks ($A_{\text{stack}} = 0.8\,\mu\text{m}^2$). The large-stack device exhibits a dense pattern of small avoided level crossings of the qubit transition f_{01}, indicative of resonant coupling to TLS in the junction barriers. In contrast, the small-stack device shows a much cleaner spectrum with only a few weak splittings.

Figure 6.13 compares high-resolution two-tone spectroscopy of two devices with identical array length $N = 32$ but different stack footprints, recorded around half-flux bias. For the large-stack device (*L-C3*, $A_{\mathrm{stack}} = 4.0\,\mu\mathrm{m}^2$), the smooth flux dispersion of f_{01} is densely punctuated by small avoided level crossings, giving the spectrum a visibly fragmented appearance. In contrast, the small-stack device (*S-A3*, $A_{\mathrm{stack}} = 0.8\,\mu\mathrm{m}^2$) exhibits only a few isolated splittings, and the qubit transition remains essentially smooth over a wide flux range.

These avoided level crossings constitute the characteristic spectral signature of coherent coupling between the qubit and microscopic TLS in amorphous oxides, as discussed in Sec. 3.3.1. At a TLS resonance, the bare qubit and TLS levels hybridize, resulting in two frequency branches separated by a splitting S. This splitting is related to the qubit–TLS coupling strength g (in angular frequency units) via $2g = 2\pi S$, see Eq. (3.24). The observed splittings correspond to typical coupling strengths on the order of $g/2\pi \sim 1\,\mathrm{MHz}$, consistent with TLS located in the amorphous oxide of Josephson junction tunnel barriers [27, 28, 110].

The pronounced difference between large and small stacks already indicates that the increased junction area in large stacks hosts a substantially higher density of TLS, thereby opening additional relaxation channels. This observation is qualitatively consistent with the reduced T_1 times reported in Fig. 6.7.

6.6.2 TLS statistics in stacked junctions

To quantify how many TLS couple to the qubit for a given array size, we apply the cumulative approach introduced by Martinis *et al.* [28], which is directly motivated by a microscopic TLS model based on the standard tunneling model [114–116]. In this model, TLS are described as electric dipoles with random spatial positions and orientations within the amorphous tunnel barriers. The coupling strength between a TLS and the qubit scales as $S \propto pE\cos\theta$, where p is the TLS dipole moment, E the local electric field across the junction, and θ the relative angle between dipole and field (Sec. 3.3.1). Averaging over random dipole orientations and tunneling asymmetries yields a broad distribution of splitting sizes with $\mathrm{d}N/\mathrm{d}S \propto 1/S$ up to a largest observable coupling set by rare, strongly coupled defects. As a consequence, the integrated number of splittings up to a threshold S_0 increases logarithmically with S_0.

For each device, all resolvable avoided level crossings within a frequency bandwidth of the qubit spectrum are collected and analyzed. We plot the cumulative number of splitting sizes per GHz as a function of the threshold splitting S_0. The cumulative number $N_{\mathrm{TLS}}(S \leq S_0)/\mathrm{GHz}$ thus counts how many TLS exhibit splittings with a

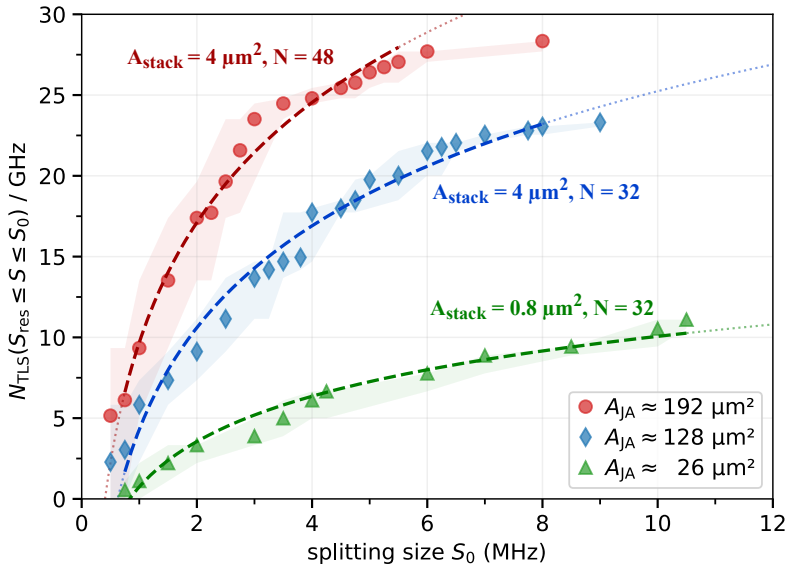

Figure 6.14: Cumulative TLS statistics grouped by the total stacked junction area. Cumulative number of TLS-induced avoided level crossings per GHz as a function of the splitting threshold S_0, grouped by the total junction area of the array $A_{JA} = N\,A_{stack}$. The dashed lines correspond to fits using Eq. (6.6) with a fixed resolution cutoff $S_{res} \approx 0.5\,\text{MHz}$; thin dotted lines indicate extrapolations beyond the fitted range. Shaded bands indicate the uncertainty of the cumulative counts, estimated by assuming a finite spectroscopic resolution of the extracted splitting sizes of $\approx 0.5\,\text{MHz}$, comparable to the typical linewidth of the qubit transition in the measured spectra. The uncertainty increases in regions with a high density of splittings in the cumulative statistics. The statistics are derived from approximately 200 avoided level crossings observed in 14 qubit spectra.

size smaller than a chosen threshold S_0. Figure 6.14 shows the resulting cumulative distributions grouped by the total stacked junction area, $A_{JA} = N\,A_{stack}$. A clear trend emerges: the cumulative curves shift systematically upward as A_{JA} increases.

For a single curve, splitting sizes below a small threshold $S_{res} \approx 0.5\,\text{MHz}$ fall below the spectroscopy resolution, while at large S_0 an apparent cutoff S_{max} emerges, reflecting the largest observed couplings. The cumulative statistics follow the logarithmic form derived in Sec. 3.3.1, Eq. (3.34), with the cumulative number given by

$$N_{TLS}(S_{res} \leq S \leq S_0) = \rho_{TLS}\,\ln\left(\frac{S_0}{S_{res}}\right)\,, \tag{6.6}$$

where ρ_{TLS} is the spectral TLS density (number of TLS per GHz associated with the stacked junction array) and the constant offset accounts for the limited spectroscopy

resolution at small splitting sizes [28, 194]. Here, S_{res} denotes the minimum resolvable splitting set by the finite spectroscopic resolution, where TLS with smaller splittings are not detected and therefore do not contribute to the cumulative count. The cumulative distributions in Fig. 6.14 are fitted using Eq. (6.6) (dashed lines), excluding the low-S regime affected by the resolution limit and the high-S region near saturation, where statistics are low. The results are summarized in Table 6.6.

The extracted spectral TLS density increases markedly with A_{JA}, demonstrating across many measured devices that the number of TLS per GHz grows with the total tunnel-barrier area of the stacked junctions. Normalizing ρ_{TLS} by A_{JA} yields areal TLS densities between 0.3 and 0.9 TLS $/(\mathrm{GHz}{\cdot}\mu\mathrm{m}^2)$, in good agreement with literature values for $\mathrm{Al/AlO}_x\mathrm{/Al}$ tunnel barriers [27, 28, 194–197].[3] This confirms that the TLS population responsible for the observed avoided level crossings resides in the stacked junction arrays.

Comparing the values of $\rho_{\mathrm{TLS}}/A_{\mathrm{JA}}$ in Table 6.6, we note a decrease with increasing A_{JA}, whereas a constant areal density would be expected for a uniform TLS distribution in $\mathrm{Al/AlO}_x\mathrm{/Al}$ tunnel barriers [114, 196, 198]. We attribute this trend to the reduced qubit–TLS coupling strength at larger N due to capacitive voltage division across the array, which shifts an increasing fraction of splitting sizes below the spectroscopy resolution. Consequently, the extracted TLS densities should be regarded as a lower bound on the true defect density in the tunnel barriers.

Table 6.6: TLS densities extracted from cumulative TLS statistics. The spectral TLS density ρ_{TLS} is obtained from fits to the data in Fig. 6.14 using Eq. (6.6). Quoted uncertainties are regression errors. Normalizing by the total stacked junction area A_{JA} yields an areal TLS density.

A_{stack}	N	A_{JA} ($\mu\mathrm{m}^2$)	ρ_{TLS} (1/GHz)	$\rho_{\mathrm{TLS}}/A_{\mathrm{JA}}$ (1/GHz·$\mu\mathrm{m}^2$)
4.0	48	192	60 ± 1	0.3
4.0	32	128	48 ± 1	0.4
0.8	32	26	22 ± 1	0.9

[3] For completeness, attributing all observed splittings to the small-junction (area $A_{\mathrm{J}} \sim 0.04\,\mu\mathrm{m}^2$) would imply unrealistically large areal TLS densities.

6.6.3 Dependence of energy relaxation on the array geometry

The results obtained in the previous section establish a relation between the stacked junction sizes and the TLS density in their tunnel barriers. Finally, we connect these findings to the observed relaxation times using a Fermi's golden rule description of qubit decay in the presence of TLS, as introduced in Sec. 3.3.1.

When a qubit interacts with many weakly coupled TLS, each defect in the vicinity of the qubit transition frequency opens an additional relaxation channel. Experimentally, this results in Lorentzian dips in $T_1(f)$ (Sec. 3.3.1) [27, 199]. Instead of resolving individual line shapes, a coarse-grained argument is used: averaging the Golden-rule relaxation rate of the qubit in Eq. (3.28) over a bath of TLS with spectral density ρ_{TLS} leads to the scaling [28, 199]

$$\langle \Gamma_1 \rangle \propto \rho_{\mathrm{TLS}} \langle g^2 \rangle , \tag{6.7}$$

where $\langle g^2 \rangle$ is the mean squared qubit–TLS coupling.

In an ideal homogeneous array of N identical junctions (neglecting the small parasitic ground capacitances discussed in Sec. 5.3), the phase drop across the array is approximately uniformly distributed among the junctions, such that the array voltage divides equally across the series junctions. Consequently, the mean coupling of a TLS in one array junction is reduced by a factor $1/N$. Equation (6.7) reduces to $\langle \Gamma_1 \rangle \propto \rho_{\mathrm{TLS}}/N^2$. Since ρ_{TLS} is proportional to the total tunnel-barrier area, $N\,A_{\mathrm{stack}}$, we obtain

$$\langle \Gamma_1 \rangle \propto \frac{A_{\mathrm{stack}}}{N} \quad \Rightarrow \quad \langle T_1 \rangle \propto \frac{N}{A_{\mathrm{stack}}} . \tag{6.8}$$

These simplified scaling relations, together with the extracted TLS densities, provide a qualitative explanation for the T_1 behavior observed at the quarton qubits with stacked junctions (Sec. 6.4). Devices with $A_{\mathrm{stack}} = 4\,\mu\mathrm{m}^2$ exhibit substantially more TLS in a stacked junction than those with $A_{\mathrm{stack}} = 0.8\,\mu\mathrm{m}^2$ and thus shorter relaxation times. For small stacks, a trend toward longer T_1 at $N = 32$ compared to $N = 16$ is observed, in agreement with the reduced mean coupling at larger N for otherwise identical junction footprints. For large stacks, increasing N from 16 to 48, we do not note a clear trend in the coherence times.

Overall, the combined spectroscopic signatures, cumulative statistics, and Fermi's golden rule analysis provide compelling evidence that microscopic TLS in the stacked junction arrays constitute the dominant decoherence channel limiting T_1 in the quarton qubits.

7 Conclusion

Superconducting quantum circuits require compact, low-loss inductive elements, strongly anharmonic potential landscapes, and stable flux biasing. The goal of this thesis was to investigate how these requirements can be experimentally realized and understood using stacked Josephson junctions, flux qubits operated in the quarton regime, and a persistent-current biasing approach.

The first part of this thesis established vertically stacked Josephson junctions as compact linear inductors. Their three-dimensional geometry lifts the superconducting electrodes from the substrate and stacks multiple junctions within a small footprint, while exposing only narrow sidewalls to the substrate, thereby reducing the capacitance to ground. Using a stack-pair model and electrostatic simulations, stray and ground capacitances were quantified, capacitance matrices for realistic geometries were derived, and eigenmodes of extended arrays were calculated. The results show that stacked junction arrays exhibit a much smaller capacitance to ground than their junction capacitance, long Coulomb screening lengths, and resonant frequencies well above those relevant for quantum-circuit operation. This enables the realization of large inductances or impedances in compact arrays. A subtractive fabrication process with layer-by-layer oxidation allows compensation of junction-area variations and enables uniform tunnel barriers. Cryogenic transport measurements confirmed strongly underdamped $\mathrm{Al/AlO}_x\mathrm{/Al}$ junctions with high subgap resistance and McCumber parameters on the order of 10^5.

Building on these inductors, the second part of the thesis investigated flux qubits operated in the quarton regime. In these devices, stacked-junction arrays provide the linear inductance, while small Manhattan-style junctions introduce strong anharmonicity. By varying stack footprint and array length, the circuit inductance was systematically tuned while maintaining the quarton condition across many devices. At the qubit operating point, qubit frequencies between $3-5\,\mathrm{GHz}$ and positive anharmonicities of $0.5-1.5\,\mathrm{GHz}$ were measured, consistent with a quartic potential landscape. Time-domain measurements revealed that coherence is strongly influenced by the stack footprint: qubits with large stacks exhibited typical T_1 times of about $2\,\mu\mathrm{s}$, whereas qubits with small stacks reached T_1 values around $10\,\mu\mathrm{s}$

and up to 20 µs. For small stacks, longer arrays showed a trend toward increased median T_1 times.

Decoherence from external flux noise was investigated using a persistent-current bias, which provides a stable and low-noise flux bias for quarton qubits. To trap and store a persistent current in a local bias coil, the experimental setup was extended by an auxiliary circuit and short heat pulses employed to trap a desired current value during operation at millikelvin temperatures. Spectroscopy and time-domain measurements demonstrated that the persistent-current bias can be set with high precision and remains stable over time scales of up to one week. A direct comparison of two nominally identical quarton qubits—one biased conventionally and one biased via a trapped persistent current—ruled out external flux noise as the dominant coherence-limiting mechanism.

High-resolution spectroscopy revealed dense avoided level crossings in devices with large stacks and significantly fewer in devices with small stacks, identifying two-level systems (TLS) in the amorphous tunnel-barrier oxides of stacked junctions as the dominant relaxation channel. Cumulative splitting statistics extracted from more than a dozen qubit spectra show that the spectral TLS density scales with the total tunnel-barrier oxide volume of the arrays, set by the stack footprint, while the array length determines the average qubit-TLS coupling strength through voltage division. These observations are consistent with a Fermi's golden rule description of qubit decay in the presence of many weakly coupled TLS and provide a qualitative explanation for the observed dependence of T_1 on array geometry. The results motivate further improvements in coherence by reducing the stack footprint or increasing the number of junctions in the array.

Future work may further explore the microscopic origin of coherence limitations in stacked-junction circuits. Controlled spectroscopy of individual and collective TLS, for example by tuning their energies using strain or local electric fields, could distinguish TLS located in tunnel barriers from surface-related defects. Such experiments may clarify how TLS density and coupling strength vary within a stack and how the three-dimensional geometry of stacked arrays influences them. The persistent-current bias provides a complementary opportunity to investigate flux-noise-related decoherence in a well-isolated setting, allowing external flux noise to be largely suppressed and intrinsic flux-noise mechanisms to be probed.

Bibliography

[1] J. E. Mooij, T. P. Orlando, L. Levitov, L. Tian, C. H. van der Wal, and S. Lloyd: *Josephson Persistent-Current Qubit*. Science **285** (1999), 1036–1039. DOI: 10.1126/science.285.5430.1036 (cit. on pp. 1, 48).

[2] V. E. Manucharyan, J. Koch, L. I. Glazman, and M. H. Devoret: *Fluxonium: Single Cooper-Pair Circuit Free of Charge Offsets*. Science **326** (2009), 113–116. DOI: 10.1126/science.1175552 (cit. on pp. 1, 11, 22, 27, 42–45, 48, 50, 71, 73).

[3] L. B. Nguyen, Y.-H. Lin, A. Somoroff, R. Mencia, N. Grabon, and V. E. Manucharyan: *High-Coherence Fluxonium Qubit*. Physical Review X **9** (2019). DOI: 10.1103/physrevx.9.041041 (cit. on pp. 1, 11, 45, 50, 71).

[4] F. Yan, Y. Sung, P. Krantz, A. Kamal, D. K. Kim, J. L. Yoder, T. P. Orlando, S. Gustavsson, and W. D. Oliver: *Engineering Framework for Optimizing Superconducting Qubit Designs* (2020). DOI: 10.48550/ARXIV.2006.04130 (cit. on pp. 1, 2, 27, 42, 45, 48, 50, 52, 53, 71, 95, 101, 103, 107).

[5] N. A. Masluk, I. M. Pop, A. Kamal, Z. K. Minev, and M. H. Devoret: *Microwave Characterization of Josephson Junction Arrays: Implementing a Low Loss Superinductance*. Phys. Rev. Lett. **109** (2012). DOI: 10.1103/physrevlett.109.137002 (cit. on pp. 1, 11, 12, 50, 71–74).

[6] A. Ranni, H. Havir, S. Haldar, and V. F. Maisi: *High impedance Josephson junction resonators in the transmission line geometry*. Applied Physics Letters **123** (2023). DOI: 10.1063/5.0164323 (cit. on pp. 1, 2).

[7] L. Grünhaupt, M. Spiecker, D. Gusenkova, N. Maleeva, S. T. Skacel, I. Takmakov, F. Valenti, P. Winkel, H. Rotzinger, W. Wernsdorfer, A. V. Ustinov, and I. M. Pop: *Granular aluminium as a superconducting material for high-impedance quantum circuits*. Nature Materials **18** (2019), 816–819. DOI: 10.1038/s41563-019-0350-3 (cit. on pp. 1, 2, 12).

[8] W. Zhang, K. Kalashnikov, W.-S. Lu, P. Kamenov, T. DiNapoli, and M. Gershenson: *Microresonators Fabricated from High-Kinetic-Inductance Aluminum Films*. Physical Review Applied **11** (2019). DOI: 10.1103/physrevapplied.11.011003 (cit. on p. 1).

[9] J. Basset, D. Watfa, G. Aiello, M. Féchant, A. Morvan, J. Estève, J. Gabelli, M. Aprili, R. Weil, A. Kasumov, H. Bouchiat, and R. Deblock: *High kinetic inductance microwave resonators made by He-Beam assisted deposition of tungsten nanowires*. Applied Physics Letters **114** (2019). DOI: 10.1063/1.5080925 (cit. on p. 1).

[10] S. Frasca, I. Arabadzhiev, S. B. de Puechredon, F. Oppliger, V. Jouanny, R. Musio, M. Scigliuzzo, F. Minganti, P. Scarlino, and E. Charbon: *NbN films with high kinetic inductance for high-quality compact superconducting resonators*. Physical Review Applied **20** (2023). DOI: 10.1103/physrevapplied.20.044021 (cit. on p. 1).

[11] M. Yang, X. He, W. Gao, J. Chen, Y. Wu, X. Wang, G. Mu, W. Peng, and Z. Lin: *Kinetic inductance compact resonator with NbTiN micronwires*. AIP Advances **14** (2024). DOI: 10.1063/5.0220296 (cit. on p. 1).

[12] I. M. Pop, K. Geerlings, G. Catelani, R. J. Schoelkopf, L. I. Glazman, and M. H. Devoret: *Coherent suppression of electromagnetic dissipation due to superconducting quasiparticles*. Nature **508** (2014), 369–372. DOI: 10.1038/nature13017 (cit. on pp. 1, 74).

[13] Y. Chen et al.: *Qubit Architecture with High Coherence and Fast Tunable Coupling*. Physical Review Letters **113** (2014). DOI: 10.1103/physrevlett.113.220502 (cit. on p. 1).

[14] F. Yan, P. Krantz, Y. Sung, M. Kjaergaard, D. L. Campbell, T. P. Orlando, S. Gustavsson, and W. D. Oliver: *Tunable Coupling Scheme for Implementing High-Fidelity Two-Qubit Gates*. Physical Review Applied **10** (2018). DOI: 10.1103/physrevapplied.10.054062 (cit. on pp. 1, 2, 101).

[15] M. Peruzzo, A. Trioni, F. Hassani, M. Zemlicka, and J. M. Fink: *Surpassing the Resistance Quantum with a Geometric Superinductor*. Physical Review Applied **14** (2020). DOI: 10.1103/physrevapplied.14.044055 (cit. on p. 1).

[16] F. Yan, S. Gustavsson, A. Kamal, J. Birenbaum, A. P. Sears, D. Hover, T. J. Gudmundsen, D. Rosenberg, G. Samach, S. Weber, J. L. Yoder, T. P. Orlando, J. Clarke, A. J. Kerman, and W. D. Oliver: *The flux qubit revisited to enhance coherence and reproducibility*. Nature Communications **7** (2016). DOI: 10.1038/ncomms12964 (cit. on pp. 1, 45, 48).

[17] M. T. Randeria, T. M. Hazard, A. Di Paolo, K. Azar, M. Hays, L. Ding, J. An, M. Gingras, B. M. Niedzielski, H. Stickler, J. A. Grover, J. L. Yoder, M. E. Schwartz, W. D. Oliver, and K. Serniak: *Dephasing in Fluxonium Qubits from Coherent Quantum Phase Slips*. PRX Quantum **5** (2024). DOI: 10.1103/prxquantum.5.030341 (cit. on p. 1).

[18] H. Rotzinger, S. T. Skacel, M. Pfirrmann, J. N. Voss, J. Münzberg, S. Probst, P. Bushev, M. P. Weides, A. V. Ustinov, and J. E. Mooij: *Aluminium-oxide wires for superconducting high kinetic inductance circuits*. Superconductor Science and Technology **30** (2016), 025002. DOI: 10.1088/0953-2048/30/2/025002 (cit. on pp. 1, 12).

[19] D. Niepce, J. Burnett, and J. Bylander: *High Kinetic Inductance NbN Nanowire Superinductors*. Phys. Rev. Applied **11** (2019). DOI: 10.1103/physrevapplied.11.044014 (cit. on pp. 1, 2, 12).

[20] A. Shearrow, G. Koolstra, S. J. Whiteley, N. Earnest, P. S. Barry, F. J. Heremans, D. D. Awschalom, E. Shirokoff, and D. I. Schuster: *Atomic layer deposition of titanium nitride for quantum circuits*. Applied Physics Letters **113** (2018). DOI: 10.1063/1.5053461 (cit. on pp. 1, 12, 71).

[21] J. T. Peltonen, P. C. J. J. Coumou, Z. H. Peng, T. M. Klapwijk, J. S. Tsai, and O. V. Astafiev: *Hybrid rf SQUID qubit based on high kinetic inductance*. Scientific Reports **8** (2018). DOI: 10.1038/s41598-018-27154-1 (cit. on p. 1).

[22] N. Maleeva, L. Grünhaupt, T. Klein, F. Levy-Bertrand, O. Dupre, M. Calvo, F. Valenti, P. Winkel, F. Friedrich, W. Wernsdorfer, A. V. Ustinov, H. Rotzinger, A. Monfardini, M. V. Fistul, and I. M. Pop: *Circuit quantum electrodynamics of granular aluminum resonators*. Nature Communications **9** (2018). DOI: 10.1038/s41467-018-06386-9 (cit. on pp. 1, 71).

[23] N. Kirsh, E. Svetitsky, S. Goldstein, G. Pardo, O. Hachmo, and N. Katz: *Linear and Nonlinear Properties of a Compact High-Kinetic-Inductance WSi Multimode Resonator*. Physical Review Applied **16** (2021). DOI: 10.1103/physrevapplied.16.044017 (cit. on p. 1).

[24] M. Kristen, J. N. Voss, M. Wildermuth, H. Rotzinger, and A. V. Ustinov: *Random telegraph fluctuations in granular microwave resonators*. Applied Physics Letters **122** (2023). DOI: 10.1063/5.0147430 (cit. on pp. 1, 12, 61).

[25] M. Peruzzo, F. Hassani, G. Szep, A. Trioni, E. Redchenko, M. Žemlička, and J. M. Fink: *Geometric Superinductance Qubits: Controlling Phase Delocalization across a Single Josephson Junction*. PRX Quantum **2** (2021). DOI: 10.1103/prxquantum.2.040341 (cit. on p. 1).

[26] M. Kristen, J. Voss, M. Wildermuth, A. Bilmes, J. Lisenfeld, H. Rotzinger, and A. Ustinov: *Giant Two-Level Systems in a Granular Superconductor*. Physical Review Letters **132** (2024). DOI: 10.1103/physrevlett.132.217002 (cit. on pp. 1, 12, 61).

[27] J. Lisenfeld, A. Bilmes, A. Megrant, R. Barends, J. Kelly, P. Klimov, G. Weiss, J. M. Martinis, and A. V. Ustinov: *Electric field spectroscopy of material defects in transmon qubits*. npj Quantum Information **5** (2019). DOI: 10.1038/s41534-019-0224-1 (cit. on pp. 1, 36–40, 117, 119, 120).

[28] J. M. Martinis, K. B. Cooper, R. McDermott, M. Steffen, M. Ansmann, K. D. Osborn, K. Cicak, S. Oh, D. P. Pappas, R. W. Simmonds, and C. C. Yu: *Decoherence of a Superconducting Qubit Due to Dielectric Loss*. Phys. Rev. Lett. **95** (2005), 210503. DOI: 10.1103/PhysRevLett.95.210503 (cit. on pp. 1, 36–40, 117, 119, 120).

[29] R. Kuzmin, R. Mencia, N. Grabon, N. Mehta, Y.-H. Lin, and V. E. Manucharyan: *Quantum electrodynamics of a superconductor–insulator phase transition*. Nature Physics **15** (2019), 930–934. DOI: 10.1038/s41567-019-0553-1 (cit. on p. 1).

[30] J. Wenner et al.: *Surface loss simulations of superconducting coplanar waveguide resonators*. Applied Physics Letters **99** (2011). DOI: 10.1063/1.3637047 (cit. on p. 2).

[31] M. V. P. Altoé et al.: *Localization and Mitigation of Loss in Niobium Superconducting Circuits*. PRX Quantum **3** (2022). DOI: 10.1103/prxquantum.3.020312 (cit. on p. 2).

[32] A. Kreuzer, T. Krumrey, H. Tohamy, A. Ionita, H. Rotzinger, and A. V. Ustinov: *Stacked Josephson junctions for quantum circuit applications*. Phys. Rev. Applied (2025). arXiv: 2503.11437 [cond-mat.supr-con]. accepted for publication; to appear (cit. on pp. 2, 71).

[33] P. Manset, J. Palomo, A. Schmitt, K. Gerashchenko, R. Rousseau, H. Patange, P. Abgrall, E. Flurin, S. Deléglise, T. Jacqmin, and L. Balembois: *Hyperinductance based on stacked Josephson junctions*. 2025. DOI: 10.48550/ARXIV.2505.02764 (cit. on pp. 2, 73, 74).

[34] Y. Ye, K. Peng, M. Naghiloo, G. Cunningham, and K. P. O'Brien: *Engineering Purely Nonlinear Coupling between Superconducting Qubits Using a Quarton*. Physical Review Letters **127** (2021). DOI: 10.1103/physrevlett.127.050502 (cit. on pp. 2, 43, 45, 52, 53).

[35] L. Chirolli, M. Carrega, and F. Giazotto: *The quartic Blochnium: an anharmonic quasicharge superconducting qubit*. Quantum **7** (2023), 1193. DOI: 10.22331/q-2023-12-04-1193 (cit. on pp. 2, 52, 53).

[36] Y. Ye, J. B. Kline, S. Chen, A. Yen, and K. P. O'Brien: *Ultrafast superconducting qubit readout with the quarton coupler*. Science Advances **10** (2024). DOI: 10.1126/sciadv.ado9094 (cit. on pp. 2, 52, 53).

[37] Y. Ye, J. B. Kline, A. Yen, G. Cunningham, M. Tan, A. Zang, M. Gingras, B. M. Niedzielski, H. Stickler, K. Serniak, M. E. Schwartz, and K. P. O'Brien: *Near-ultrastrong nonlinear light-matter coupling in superconducting circuits*. Nature Communications **16** (2025). DOI: 10.1038/s41467-025-59152-z (cit. on pp. 2, 52, 53).

[38] F. Yoshihara, K. Harrabi, A. O. Niskanen, Y. Nakamura, and J. S. Tsai: *Decoherence of Flux Qubits due to 1/f Flux Noise*. Phys. Rev. Lett. **97** (2006), 167001. DOI: 10.1103/PhysRevLett.97.167001 (cit. on pp. 2, 34, 42, 108).

[39] J. Bylander, S. Gustavsson, F. Yan, F. Yoshihara, K. Harrabi, G. Fitch, D. G. Cory, Y. Nakamura, J.-S. Tsai, and W. D. Oliver: *Noise spectroscopy through dynamical decoupling with a superconducting flux qubit*. Nature Physics **7** (2011), 565–570. DOI: 10.1038/nphys1994 (cit. on pp. 2, 34, 35, 42, 43, 45, 108).

[40] P. Krantz, M. Kjaergaard, F. Yan, T. P. Orlando, S. Gustavsson, and W. D. Oliver: *A quantum engineer's guide to superconducting qubits*. Applied Physics Reviews **6** (2019). DOI: 10.1063/1.5089550 (cit. on pp. 2, 25–27, 32, 36, 42–44, 53, 59).

[41] D. G. Ferguson, A. A. Houck, and J. Koch: *Symmetries and Collective Excitations in Large Superconducting Circuits*. Phys. Rev. X **3** (2013). DOI: 10.1103/physrevx.3.011003 (cit. on pp. 2, 47, 48, 51, 52).

[42] W. Meissner and R. Ochsenfeld: *Ein neuer Effekt bei Eintritt der Supraleitfhigkeit*. Die Naturwissenschaften **21** (1933), 787–788. DOI: 10.1007/bf01504252 (cit. on p. 5).

[43] H. Kamerlingh Onnes: *The resistance of pure mercury at helium temperatures*. Communications from the Physical Laboratory of the University of Leiden **12** (1911), 120 (cit. on p. 5).

[44] F. London and H. London: *The Electromagnetic Equations of the Supraconductor*. Proc. R. Soc. Lond. A **149** (1935), 71–88. DOI: 10.1098/rspa.1935.0048 (cit. on p. 5).

[45] F. Behroozi and M. Garfunkel: *Penetration depth in superconducting aluminum as a function of magnetic field and temperature*. Physica **55** (1971), 649–655. DOI: 10.1016/0031-8914(71)90315-6 (cit. on p. 6).

[46] D. López-Núñez, A. Torras-Coloma, Q. Portell-Montserrat, E. Bertoldo, L. Cozzolino, G. A. Ummarino, A. Zaccone, G. Rius, M. Martínez, and P. Forn-Díaz: *Superconducting penetration depth of aluminum thin films*. Superconductor Science and Technology **38** (2025), 095004. DOI: 10.1088/1361-6668/adf360 (cit. on p. 6).

[47] M. Tinkham: *Introduction to Superconductivity*. 2nd ed. Mineola, New York: Dover Publications, 2004 (cit. on pp. 6, 7, 12–15, 20–23, 80, 85).

[48] V. L. Ginzburg and L. D. Landau: *On the Theory of Superconductivity*. Zh. Eksp. Teor. Fiz. **20** (1950), 1064–1082. DOI: 10.1007/978-3-540-68008-6_4 (cit. on p. 7).

[49] B. D. Josephson: *Possible new effects in superconductive tunnelling*. Phys. Lett. **1** (1962), 251–253. DOI: 10.1016/0031-9163(62)91369-0 (cit. on p. 9).

[50] P. W. Anderson and J. M. Rowell: *Probable Observation of the Josephson Superconducting Tunneling Effect*. Phys. Rev. Lett. **10** (1963), 230–232. DOI: 10.1103/physrevlett.10.230 (cit. on pp. 9, 14).

[51] J. M. Rowell: *Magnetic Field Dependence of the Josephson Tunnel Current*. Phys. Rev. Lett. **11** (1963), 200–202. DOI: 10.1103/physrevlett.11.200 (cit. on pp. 9, 14, 16, 17).

[52] The Royal Swedish Academy of Sciences: *Scientific Background to the Nobel Prize in Physics 2025: For the Discovery of Macroscopic Quantum Mechanical Tunnelling and Energy Quantisation in an Electric Circuit*. 2025. URL: https://www.nobelprize.org/uploads/2025/10/advanced-physicsprize2025.pdf (cit. on p. 10).

[53] J. M. Martinis, M. H. Devoret, and J. Clarke: *Energy-Level Quantization in the Zero-Voltage State of a Current-Biased Josephson Junction*. Physical Review Letters **55** (1985), 1543–1546. DOI: 10.1103/physrevlett.55.1543 (cit. on p. 10).

[54] M. H. Devoret, J. M. Martinis, and J. Clarke: *Measurements of Macroscopic Quantum Tunneling out of the Zero-Voltage State of a Current-Biased Josephson Junction*. Physical Review Letters **55** (1985), 1908–1911. DOI: 10.1103/physrevlett.55.1908 (cit. on pp. 10, 20).

[55] J. Clarke, A. N. Cleland, M. H. Devoret, D. Esteve, and J. M. Martinis: *Quantum Mechanics of a Macroscopic Variable: The Phase Difference of a Josephson Junction*. Science **239** (1988), 992–997. DOI: 10.1126/science.239.4843.992 (cit. on p. 10).

[56] K. Likharev: *Dynamics of Josephson junctions and circuits*. Gordon and Breach Science Publishers, 1986 (cit. on pp. 11, 12, 16).

[57] Y. Nakamura, Y. A. Pashkin, and J. S. Tsai: *Coherent control of macroscopic quantum states in a single-Cooper-pair box*. Nature **398** (1999), 786–788. DOI: 10.1038/19718 (cit. on pp. 11, 44, 45).

[58] B. Yurke, L. R. Corruccini, P. G. Kaminsky, L. W. Rupp, A. D. Smith, A. H. Silver, R. W. Simon, and E. A. Whittaker: *Observation of parametric amplification and deamplification in a Josephson parametric amplifier*. Physical Review A **39** (1989), 2519–2533. DOI: 10.1103/physreva.39.2519 (cit. on p. 11).

[59] R. Meservey and P. M. Tedrow: *Measurements of the Kinetic Inductance of Superconducting Linear Structures*. Journal of Applied Physics **40** (1969), 2028–2034. DOI: 10.1063/1.1657905 (cit. on p. 12).

[60] P. V. Christiansen, E. B. Hansen, and C. J. Sjöström: *Negative selfinductance in superconducting thin wires and weak links*. Journal of Low Temperature Physics **4** (1971), 349–389. DOI: 10.1007/bf00628738 (cit. on p. 12).

[61] J. Bardeen, L. N. Cooper, and J. R. Schrieffer: *Theory of Superconductivity*. Phys. Rev. **108** (1957), 1175–1204. DOI: 10.1103/physrev.108.1175 (cit. on p. 13).

[62] I. Giaever: *Energy Gap in Superconductors Measured by Electron Tunneling*. Phys. Rev. Lett. **5** (1960), 147–148. DOI: 10.1103/physrevlett.5.147 (cit. on pp. 13, 14, 16, 90, 91).

[63] B. Mühlschlegel: *Die thermodynamischen Funktionen des Supraleiters*. Z. Physik **155** (1959), 313–327. DOI: 10.1007/bf01332932 (cit. on p. 14).

[64] M. Octavio, M. Tinkham, G. E. Blonder, and T. M. Klapwijk: *Subharmonic energy-gap structure in superconducting constrictions*. Physical Review B **27** (1983), 6739–6746. DOI: 10.1103/physrevb.27.6739 (cit. on p. 15).

[65] R. C. Dynes, V. Narayanamurti, and J. P. Garno: *Direct Measurement of Quasiparticle-Lifetime Broadening in a Strong-Coupled Superconductor*. Physical Review Letters **41** (1978), 1509–1512. DOI: 10.1103/physrevlett.41.1509 (cit. on p. 15).

[66] S. B. Kaplan, C. C. Chi, D. N. Langenberg, J. J. Chang, S. Jafarey, and D. J. Scalapino: *Quasiparticle and phonon lifetimes in superconductors*. Physical Review B **14** (1976), 4854–4873. DOI: 10.1103/physrevb.14.4854 (cit. on p. 15).

[67] A. Barone and G. Paternò: *Physics and Applications of the Josephson Effect*. Wiley, 1982. DOI: 10.1002/352760278x (cit. on pp. 15, 21).

[68] F. C. Wellstood, C. Urbina, and J. Clarke: *Hot-electron effects in metals*. Physical Review B **49** (1994), 5942–5955. DOI: 10.1103/physrevb.49.5942 (cit. on pp. 15, 20, 21, 111).

[69] K. Serniak, M. Hays, G. de Lange, S. Diamond, S. Shankar, L. D. Burkhart, L. Frunzio, M. Houzet, and M. Devoret: *Hot Nonequilibrium Quasiparticles in Transmon Qubits*. Physical Review Letters **121** (2018). DOI: 10.1103/physrevlett.121.157701 (cit. on p. 15).

[70] V. Ambegaokar and A. Baratoff: *Tunneling Between Superconductors*. Phys. Rev. Lett. **10** (1963), 486–489. DOI: 10.1103/physrevlett.10.486 (cit. on p. 16).

[71] J. F. Cochran and D. E. Mapother: *Superconducting Transition in Aluminum*. Physical Review **111** (1958), 132–142. DOI: 10.1103/PhysRev.111.132 (cit. on pp. 16, 65, 90, 91).

[72] K. K. Likharev: *Superconducting weak links*. Reviews of Modern Physics **51** (1979), 101–159. DOI: 10.1103/revmodphys.51.101 (cit. on pp. 16, 18, 20, 22, 92).

[73] R. Gross and A. Marx: *Applied Superconductivity: Josephson Effect and Superconducting Electronics*. Garching, Germany: Walther-Meißner-Institut, TU München, 2005. URL: https://www.wmi.badw.de/teaching/applied_superconductivity/ (cit. on p. 16).

[74] A. Kleinsasser, R. Miller, and W. Mallison: *Dependence of critical current density on oxygen exposure in Nb-AlO/sub x/-Nb tunnel junctions*. IEEE Transactions on Appiled Superconductivity **5** (1995), 26–30. DOI: 10.1109/77.384565 (cit. on pp. 16, 89).

[75] S. K. Tolpygo, V. Bolkhovsky, S. Zarr, T. J. Weir, A. Wynn, A. L. Day, L. M. Johnson, and M. A. Gouker: *Properties of Unshunted and Resistively Shunted Nb/AlO$_x$–Al/Nb Josephson Junctions With Critical Current Densities From 0.1 to 1 mA/μm^2*. IEEE Transactions on Applied Superconductivity **27** (2017), 1–15. DOI: 10.1109/tasc.2017.2667403 (cit. on p. 16).

[76] W. C. Stewart: *Current–voltage characteristics of Josephson junctions*. Applied Physics Letters **12** (1968), 277–280. DOI: 10.1063/1.1651991 (cit. on p. 17).

[77] D. E. McCumber: *Effect of ac impedance on dc voltage–current characteristics of Josephson junctions*. Journal of Applied Physics **39** (1968), 3113–3118. DOI: 10.1063/1.1656743 (cit. on p. 17).

[78] K. Likharev and V. Semenov: *RSFQ logic/memory family: a new Josephson-junction technology for sub-terahertz-clock-frequency digital systems*. IEEE Transactions on Applied Superconductivity **1** (1991), 3–28. DOI: 10.1109/77.80745 (cit. on p. 20).

[79] J. R. Tucker and M. J. Feldman: *Quantum detection at millimeter wavelengths*. Reviews of Modern Physics **57** (1985), 1055–1113. DOI: 10.1103/revmodphys.57.1055 (cit. on p. 20).

[80] R. L. Kautz and J. M. Martinis: *Noise-affectedI-Vcurves in small hysteretic Josephson junctions*. Physical Review B **42** (1990), 9903–9937. DOI: 10.1103/physrevb.42.9903 (cit. on pp. 20, 21).

[81] J. M. Martinis, M. H. Devoret, and J. Clarke: *Experimental tests for the quantum behavior of a macroscopic degree of freedom: The phase difference across a Josephson junction*. Physical Review B **35** (1987), 4682–4698. DOI: 10.1103/physrevb.35.4682 (cit. on p. 20).

[82] J. Koch, T. M. Yu, J. Gambetta, A. A. Houck, D. I. Schuster, J. Majer, A. Blais, M. H. Devoret, S. M. Girvin, and R. J. Schoelkopf: *Charge-insensitive qubit design derived from the Cooper pair box*. Physical Review A **76** (2007). DOI: 10.1103/physreva.76.042319 (cit. on pp. 20, 26, 44, 45, 48, 98).

[83] M. H. Devoret and R. J. Schoelkopf: *Superconducting Circuits for Quantum Information: An Outlook*. Science **339** (2013), 1169–1174. DOI: 10.1126/science.1231930 (cit. on pp. 20, 71).

[84] A. Blais, A. L. Grimsmo, S. M. Girvin, and A. Wallraff: *Circuit quantum electrodynamics*. Reviews of Modern Physics **93** (2021). DOI: 10.1103/revmodphys.93.025005 (cit. on pp. 20, 25–27, 29, 30, 32, 33, 43, 53–55).

[85] H. A. Kramers: *Brownian motion in a field of force and the diffusion model of chemical reactions*. Physica **7** (1940), 284–304. DOI: 10.1016/S0031-8914(40)90098-2 (cit. on p. 20).

[86] H. Grabert and U. Weiss: *Crossover from Thermal Hopping to Quantum Tunneling*. Physical Review Letters **53** (1984), 1787–1790. DOI: 10.1103/physrevlett.53.1787 (cit. on p. 21).

[87] T. A. Fulton and L. N. Dunkleberger: *Lifetime of the zero-voltage state in Josephson tunnel junctions*. Physical Review B **9** (1974), 4760–4768. DOI: 10.1103/physrevb.9.4760 (cit. on p. 21).

[88] A. V. Timofeev, C. P. García, N. B. Kopnin, A. M. Savin, M. Meschke, F. Giazotto, and J. P. Pekola: *Recombination-Limited Energy Relaxation in a Bardeen-Cooper-Schrieffer Superconductor*. Physical Review Letters **102** (2009). DOI: 10.1103/physrevlett.102.017003 (cit. on p. 21).

[89] G.-L. Ingold and Y. V. Nazarov: "Charge Tunneling Rates in Ultrasmall Junctions". *Single Charge Tunneling*. Springer US, 1992, pp. 21–107. DOI: 10.1007/978-1-4757-2166-9_2 (cit. on p. 22).

[90] H. Grabert and M. H. Devoret: "Single Charge Tunneling: Coulomb Blockade Phenomena in Nanostructures". *Single Charge Tunneling*. Vol. 294. NATO ASI Series B: Physics. New York: Plenum Press, 1992, pp. 1–20. DOI: 10.1007/978-1-4899-2463-3 (cit. on p. 22).

[91] K. A. Matveev, A. I. Larkin, and L. I. Glazman: *Persistent Current in Superconducting Nanorings*. Phys. Rev. Lett. **89** (2002), 096802. DOI: 10.1103/PhysRevLett.89.096802 (cit. on p. 22).

[92] J. E. Mooij and Y. V. Nazarov: *Superconducting nanowires as quantum phase-slip junctions*. Nature Physics **2** (2006), 169–172. DOI: 10.1038/nphys234 (cit. on p. 22).

[93] I. M. Pop, I. Protopopov, F. Lecocq, Z. Peng, B. Pannetier, O. Buisson, and W. Guichard: *Measurement of the effect of quantum phase slips in a Josephson junction chain*. Nature Physics **6** (2010), 589–592. DOI: 10.1038/nphys1697 (cit. on pp. 22, 23).

[94] I. M. Pop, B. Douçot, L. Ioffe, I. Protopopov, F. Lecocq, I. Matei, O. Buisson, and W. Guichard: *Experimental demonstration of Aharonov-Casher interference in a Josephson junction circuit*. Physical Review B **85** (2012). DOI: 10.1103/physrevb.85.094503 (cit. on pp. 22, 71–74).

[95] O. V. Astafiev, L. B. Ioffe, S. Kafanov, Y. A. Pashkin, K. Y. Arutyunov, D. Shahar, O. Cohen, and J. S. Tsai: *Coherent quantum phase slip*. Nature **484** (2012), 355–358. DOI: 10.1038/nature10930 (cit. on pp. 22, 23).

[96] D. V. Averin and K. K. Likharev: *Coulomb blockade of single-electron tunneling, and coherent oscillations in small tunnel junctions*. Journal of Low Temperature Physics **62** (1986), 345–373. DOI: 10.1007/bf00683469 (cit. on p. 23).

[97] M. Watanabe and D. B. Haviland: *Coulomb Blockade and Coherent Single-Cooper-Pair Tunneling in Single Josephson Junctions*. Physical Review Letters **86** (2001), 5120–5123. DOI: 10.1103/physrevlett.86.5120 (cit. on p. 23).

[98] M. Kjaergaard, M. E. Schwartz, J. Braumüller, P. Krantz, J. I.-J. Wang, S. Gustavsson, and W. D. Oliver: *Superconducting Qubits: Current State of Play*. Annual Review of Condensed Matter Physics **11** (2020), 369–395. DOI: 10.1146/annurev-conmatphys-031119-050605 (cit. on pp. 25–27, 32, 33, 43).

[99] P. A. M. Dirac: *The Principles of Quantum Mechanics*. 1st. Oxford: Oxford University Press, 1930. DOI: 10.1007/978-3-476-05728-0_10148-1 (cit. on p. 28).

[100] M. A. Nielsen and I. L. Chuang: *Quantum Computation and Quantum Information*. 10th Anniversary Edition. Cambridge: Cambridge University Press, 2010 (cit. on p. 28).

[101] M. O. Scully and M. S. Zubairy: *Quantum Optics*. Cambridge University Press, 1997. DOI: 10.1017/cbo9780511813993 (cit. on pp. 29, 30, 32, 33).

[102] C. Cohen-Tannoudji, J. Dupont-Roc, and G. Grynberg: *Atom—Photon Interactions: Basic Process and Appilcations*. Wiley, 1998. DOI: 10.1002/9783527617197 (cit. on pp. 29, 30, 32, 33).

[103] I. I. Rabi: *Space Quantization in a Gyrating Magnetic Field*. Physical Review **51** (1937), 652–654. DOI: 10.1103/PhysRev.51.652 (cit. on p. 30).

[104] A. Blais, R.-S. Huang, A. Wallraff, S. M. Girvin, and R. J. Schoelkopf: *Cavity quantum electrodynamics for superconducting electrical circuits: An architecture for quantum computation*. Physical Review A **69** (2004). DOI: 10.1103/physreva.69.062320 (cit. on pp. 32, 53, 98).

[105] G. Ithier, E. Collin, P. Joyez, P. J. Meeson, D. Vion, D. Esteve, F. Chiarello, A. Shnirman, Y. Makhlin, J. Schriefl, and G. Schön: *Decoherence in a superconducting quantum bit circuit*. Physical Review B **72** (2005). DOI: 10.1103/physrevb.72.134519 (cit. on pp. 34–36, 43, 44).

[106] S. M. Anton, C. Müller, J. S. Birenbaum, S. R. O'Kelley, A. D. Fefferman, D. S. Golubev, G. C. Hilton, H.-M. Cho, K. D. Irwin, F. C. Wellstood, G. Schön, A. Shnirman, and J. Clarke: *Pure dephasing in flux qubits due to flux noise with spectral density scaling as<mml:math xmlns:mml="http://www.w3.org/1998/Math/MathML" display="inline"><mml:mrow><mml:mn>1</mml:mn><mml:mo>/</mml:mo><mml:msup>*
Physical Review B **85** (2012). DOI: 10.1103/physrevb.85.224505 (cit. on pp. 34, 35).

[107] U. Vool and M. Devoret: *Introduction to quantum electromagnetic circuits*. International Journal of Circuit Theory and Applications **45** (2017), 897–934. DOI: 10.1002/cta.2359 (cit. on p. 34).

[108] H. Paik, D. I. Schuster, L. S. Bishop, G. Kirchmair, G. Catelani, A. P. Sears, B. R. Johnson, M. J. Reagor, L. Frunzio, L. I. Glazman, S. M. Girvin, M. H. Devoret, and R. J. Schoelkopf: *Observation of High Coherence in Josephson Junction Qubits Measured in a Three-Dimensional Circuit QED Architecture*. Physical Review Letters **107** (2011). DOI: 10.1103/physrevlett.107.240501 (cit. on p. 36).

[109] J. Gao, M. Daal, A. Vayonakis, S. Kumar, J. Zmuidzinas, B. Sadoulet, B. A. Mazin, P. K. Day, and H. G. Leduc: *Experimental evidence for a surface distribution of two-level systems in superconducting lithographed microwave resonators*. Applied Physics Letters **92** (2008). DOI: 10.1063/1.2906373 (cit. on pp. 36–40).

[110] R. Simmonds, K. Lang, D. Hite, S. Nam, D. Pappas, and J. Martinis: *Decoherence in Josephson Phase Qubits from Junction Resonators*. Physical Review Letters **93** (2004). DOI: 10.1103/physrevlett.93.077003 (cit. on pp. 36, 117).

[111] R. Barends, N. Vercruyssen, A. Endo, P. J. de Visser, T. Zijlstra, T. M. Klapwijk, and J. J. A. Baselmans: *Reduced frequency noise in superconducting resonators*. Applied Physics Letters **97** (2010). DOI: 10.1063/1.3467052 (cit. on p. 36).

[112] Y. Shalibo, Y. Rofe, D. Shwa, F. Zeides, M. Neeley, J. M. Martinis, and N. Katz: *Lifetime and Coherence of Two-Level Defects in a Josephson Junction*. Physical Review Letters **105** (2010). DOI: 10.1103/physrevlett.105.177001 (cit. on p. 36).

[113] S. E. de Graaf, L. Faoro, L. B. Ioffe, S. Mahashabde, J. J. Burnett, T. Lindström, S. E. Kubatkin, A. V. Danilov, and A. Y. Tzalenchuk: *Two-level systems in superconducting quantum devices due to trapped quasiparticles*. Science Advances **6** (2020). DOI: 10.1126/sciadv.abc5055 (cit. on pp. 37, 40).

[114] C. Müller, J. H. Cole, and J. Lisenfeld: *Towards understanding two-level-systems in amorphous solids: insights from quantum circuits*. Reports on Progress in Physics **82** (2019), 124501. DOI: 10.1088/1361-6633/ab3a7e (cit. on pp. 37, 40, 61, 117, 119).

[115] P. w. Anderson, B. I. Halperin, and c. M. Varma: *Anomalous low-temperature thermal properties of glasses and spin glasses*. Philosophical Magazine **25** (1972), 1–9. DOI: 10.1080/14786437208229210 (cit. on pp. 38, 117).

[116] W. A. Phillips: *Tunneling states in amorphous solids*. Journal of Low Temperature Physics **7** (1972), 351–360. DOI: 10.1007/bf00660072 (cit. on pp. 38, 117).

[117] G. J. Grabovskij, T. Peichl, J. Lisenfeld, G. Weiss, and A. V. Ustinov: *Strain Tuning of Individual Atomic Tunneling Systems Detected by a Superconducting Qubit*. Science **338** (2012), 232–234. DOI: 10.1126/science.1226487 (cit. on p. 38).

[118] Z. Kim, V. Zaretskey, Y. Yoon, J. F. Schneiderman, M. D. Shaw, P. M. Echternach, F. C. Wellstood, and B. S. Palmer: *Anomalous avoided level crossings in a Cooper-pair box spectrum*. Physical Review B **78** (2008). DOI: 10.1103/physrevb.78.144506 (cit. on p. 38).

[119] M. S. Khalil, F. C. Wellstood, and K. D. Osborn: *Loss Dependence on Geometry and Applied Power in Superconducting Coplanar Resonators*. IEEE Transactions on Applied Superconductivity **21** (2011), 879–882. DOI: 10.1109/tasc.2010.2090330 (cit. on p. 38).

[120] B. Sarabi, A. Ramanayaka, A. Burin, F. Wellstood, and K. Osborn: *Projected Dipole Moments of Individual Two-Level Defects Extracted Using Circuit Quantum Electrodynamics*. Physical Review Letters **116** (2016). DOI: 10.1103/physrevlett.116.167002 (cit. on p. 38).

[121] J. Lisenfeld, G. J. Grabovskij, C. Müller, J. H. Cole, G. Weiss, and A. V. Ustinov: *Observation of directly interacting coherent two-level systems in an amorphous material*. Nature Communications **6** (2015). DOI: 10.1038/ncomms7182 (cit. on p. 38).

[122] S. Schlör, J. Lisenfeld, C. Müller, A. Bilmes, A. Schneider, D. P. Pappas, A. V. Ustinov, and M. Weides: *Correlating Decoherence in Transmon Qubits: Low Frequency Noise by Single Fluctuators*. Physical Review Letters **123** (2019). DOI: 10.1103/physrevlett.123.190502 (cit. on p. 38).

[123] L. Faoro and L. B. Ioffe: *Interacting tunneling model for two-level systems in amorphous materials and its predictions for their dephasing and noise in superconducting microresonators*. Physical Review B **91** (2015). DOI: 10.1103/physrevb.91.014201 (cit. on p. 40).

[124] P. Klimov et al.: *Fluctuations of Energy-Relaxation Times in Superconducting Qubits*. Physical Review Letters **121** (2018). DOI: 10.1103/physrevlett.121.090502 (cit. on p. 40).

[125] S. Sendelbach, D. Hover, A. Kittel, M. Mück, J. M. Martinis, and R. McDermott: *Magnetism in SQUIDs at Millikelvin Temperatures*. Physical Review Letters **100** (2008). DOI: 10.1103/physrevlett.100.227006 (cit. on pp. 42, 108).

[126] S. E. de Graaf, A. A. Adamyan, T. Lindström, D. Erts, S. E. Kubatkin, A. Y. Tzalenchuk, and A. V. Danilov: *Direct identification of dilute surface spins on Al_2O_3: Origin of flux noise in quantum circuits*. Physical Review Letters **118** (2017). DOI: 10.1103/physrevlett.118.057703 (cit. on pp. 42, 108).

[127] Y. Makhlin, G. Schön, and A. Shnirman: *Quantum-state engineering with Josephson-junction devices*. Reviews of Modern Physics **73** (2001), 357–400. DOI: 10.1103/revmodphys.73.357 (cit. on p. 44).

[128] J. A. Schreier, A. A. Houck, J. Koch, D. I. Schuster, B. R. Johnson, J. M. Chow, J. M. Gambetta, J. Majer, L. Frunzio, M. H. Devoret, S. M. Girvin, and R. J. Schoelkopf: *Suppressing charge noise decoherence in superconducting charge qubits*. Physical Review B **77** (2008). DOI: 10.1103/physrevb.77.180502 (cit. on p. 44).

[129] D. J. Van Harlingen, T. L. Robertson, B. L. T. Plourde, P. A. Reichardt, T. A. Crane, and J. Clarke: *Decoherence in Josephson-junction qubits due to critical-current fluctuations*. Physical Review B **70** (2004). DOI: 10.1103/physrevb.70.064517 (cit. on p. 44).

[130] F. C. Wellstood, C. Urbina, and J. Clarke: *Low-frequency noise in dc superconducting quantum interference devices below 1 K*. Applied Physics Letters **50** (1987), 772–774. DOI: 10.1063/1.98041 (cit. on p. 44).

[131] J. M. Martinis, M. Ansmann, and J. Aumentado: *Energy Decay in Superconducting Josephson-Junction Qubits from Nonequilibrium Quasiparticle Excitations*. Physical Review Letters **103** (2009). DOI: 10.1103/physrevlett.103.097002 (cit. on p. 44).

[132] G. Catelani, J. Koch, L. Frunzio, R. J. Schoelkopf, M. H. Devoret, and L. I. Glazman: *Quasiparticle Relaxation of Superconducting Qubits in the Presence of Flux*. Physical Review Letters **106** (2011). DOI: 10.1103/physrevlett.106.077002 (cit. on pp. 44, 46, 47, 61).

[133] D. I. Schuster, A. Wallraff, A. Blais, L. Frunzio, R.-S. Huang, J. Majer, S. M. Girvin, and R. J. Schoelkopf: *ac Stark Shift and Dephasing of a Superconducting Qubit Strongly Coupled to a Cavity Field*. Physical Review Letters **94** (2005). DOI: 10.1103/physrevlett.94.123602 (cit. on p. 44).

[134] J. Gambetta, A. Blais, D. I. Schuster, A. Wallraff, L. Frunzio, J. Majer, M. H. Devoret, S. M. Girvin, and R. J. Schoelkopf: *Qubit-photon interactions in a cavity: Measurement-induced dephasing and number splitting*. Physical Review A **74** (2006). DOI: 10.1103/physreva.74.042318 (cit. on p. 44).

[135] T. P. Orlando, J. E. Mooij, L. Tian, C. H. van der Wal, L. S. Levitov, S. Lloyd, and J. E. Mazo: *Superconducting persistent-current qubit*. Physical Review B **60** (1999), 15398–15413. DOI: 10.1103/PhysRevB.60.15398 (cit. on pp. 45, 48).

[136] G. Viola and G. Catelani: *Collective modes in the fluxonium qubit*. Physical Review B **92** (2015). DOI: 10.1103/physrevb.92.224511 (cit. on pp. 47, 48, 51, 52).

[137] E. A. Sete, J. M. Martinis, and A. N. Korotkov: *Quantum theory of a bandpass Purcell filter for qubit readout*. Physical Review A **92** (2015). DOI: 10.1103/physreva.92.012325 (cit. on pp. 54, 55, 62).

[138] D. M. Pozar: *Microwave Engineering*. 4th ed. Hoboken, NJ: Wiley, 2012 (cit. on pp. 56–60, 63, 68).

[139] R. E. Collin: *Foundations for Microwave Engineering*. 2nd ed. New York: IEEE Press, 1992 (cit. on pp. 56–58).

[140] S. Probst, F. B. Song, P. A. Bushev, A. V. Ustinov, and M. Weides: *Efficient and robust analysis of complex scattering data under noise in microwave resonators*. Review of Scientific Instruments **86** (2015). DOI: 10.1063/1.4907935 (cit. on p. 62).

[141] P. G. Baity, C. Maclean, V. Seferai, J. Bronstein, Y. Shu, T. Hemakumara, and M. Weides: *Circle fit optimization for resonator quality factor measurements: Point redistribution for maximal accuracy*. Physical Review Research **6** (2024). DOI: 10.1103/physrevresearch.6.013329 (cit. on p. 62).

[142] M. D. Reed, L. DiCarlo, S. E. Nigg, L. Sun, L. Frunzio, S. M. Girvin, and R. J. Schoelkopf: *Realization of three-qubit quantum error correction with superconducting circuits*. Nature **482** (2012), 382–385. DOI: 10.1038/nature10786 (cit. on p. 62).

[143] E. Jeffrey et al.: *Fast Accurate State Measurement with Superconducting Qubits*. Physical Review Letters **112** (2014). DOI: 10.1103/physrevlett.112.190504 (cit. on pp. 62, 63).

[144] D. I. Schuster: *Circuit Quantum Electrodynamics*. PhD thesis. Yale University, 2007. URL: https://schusterlab.stanford.edu/static/pdfs/Schuster_thesis.pdf (cit. on p. 62).

[145] J. Heinsoo, C. K. Andersen, A. Remm, S. Krinner, T. Walter, Y. Salathé, S. Gasparinetti, J.-C. Besse, A. Potočnik, A. Wallraff, and C. Eichler: *Rapid High-fidelity Multiplexed Readout of Superconducting Qubits*. Physical Review Applied **10** (2018). DOI: 10.1103/physrevapplied.10.034040 (cit. on p. 62).

[146] A. D. Stehli: *Analog quantum simulator of the multistate Landau-Zener model*. PhD thesis. Karlsruhe, Germany: Karlsruhe Institute of Technology (KIT), 2021. URL: https://https://publikationen.bibliothek.kit.edu/1000132804 (cit. on p. 63).

[147] R. Barends et al.: *Minimizing quasiparticle generation from stray infrared light in superconducting quantum circuits*. Applied Physics Letters **99** (2011). DOI: 10.1063/1.3638063 (cit. on p. 65).

[148] C. Wang, Y. Y. Gao, I. M. Pop, U. Vool, C. Axline, T. Brecht, R. W. Heeres, L. Frunzio, M. H. Devoret, G. Catelani, L. I. Glazman, and R. J. Schoelkopf: *Measurement and control of quasiparticle dynamics in a superconducting qubit*. Nature Communications **5** (2014). DOI: 10.1038/ncomms6836 (cit. on p. 65).

[149] S. Krinner, S. Storz, P. Kurpiers, P. Magnard, J. Heinsoo, R. Keller, J. Lütolf, C. Eichler, and A. Wallraff: *Engineering cryogenic setups for 100-qubit scale superconducting circuit systems*. EPJ Quantum Technology **6** (2019). DOI: 10.1140/epjqt/s40507-019-0072-0 (cit. on pp. 65, 66).

[150] E. T. Mannila, P. Samuelsson, S. Simbierowicz, J. T. Peltonen, V. Vesterinen, L. Grönberg, J. Hassel, V. F. Maisi, and J. P. Pekola: *A superconductor free of quasiparticles for seconds*. Nature Physics **18** (2021), 145–148. DOI: 10.1038/s41567-021-01433-7 (cit. on p. 65).

[151] S. Krinner, S. Lazar, A. Remm, C. Andersen, N. Lacroix, G. Norris, C. Hellings, M. Gabureac, C. Eichler, and A. Wallraff: *Benchmarking Coherent Errors in Controlled-Phase Gates due to Spectator Qubits*. Physical Review Applied **14** (2020). DOI: 10.1103/physrevapplied.14.024042 (cit. on p. 66).

[152] B. Patra, R. M. Incandela, J. P. G. van Dijk, H. A. R. Homulle, L. Song, M. Shahmohammadi, R. B. Staszewski, A. Vladimirescu, M. Babaie, F. Sebastiano, and E. Charbon: *Cryo-CMOS Circuits and Systems for Quantum Computing Applications*. IEEE Journal of Solid-State Circuits **53** (2018), 309–321. DOI: 10.1109/jssc.2017.2737549 (cit. on p. 66).

[153] *Quantum Computing: Progress and Prospects* (2019). Ed. by E. Grumbling and M. Horowitz. DOI: 10.17226/25196 (cit. on p. 66).

[154] C. Enss and S. Hunklinger: *Low-Temperature Physics*. Springer, 2005 (cit. on p. 68).

[155] F. Pobell: *Matter and Methods at Low Temperatures*. 3rd ed. Berlin, Heidelberg: Springer, 2007 (cit. on p. 68).

[156] B. Oy: *LD250 Dilution Refrigerator System Specifications*. 2023. URL: https://bluefors.com/products/ld/ (cit. on p. 68).

[157] M. T. Bell, I. A. Sadovskyy, L. B. Ioffe, A. Y. Kitaev, and M. E. Gershenson: *Quantum Superinductor with Tunable Nonlinearity*. Physical Review Letters **109** (2012). DOI: 10.1103/physrevlett.109.137003 (cit. on pp. 71, 72, 74).

[158] T. Hazard, A. Gyenis, A. Di Paolo, A. Asfaw, S. Lyon, A. Blais, and A. Houck: *Nanowire Superinductance Fluxonium Qubit*. Physical Review Letters **122** (2019). DOI: 10.1103/physrevlett.122.010504 (cit. on pp. 71, 72).

[159] A. Kitaev: *Protected qubit based on a superconducting current mirror* (2006). DOI: 10.48550/ARXIV.COND-MAT/0609441 (cit. on p. 71).

[160] S. Gladchenko, D. Olaya, E. Dupont-Ferrier, B. Douçot, L. B. Ioffe, and M. E. Gershenson: *Superconducting nanocircuits for topologically protected qubits*. Nature Physics **5** (2008), 48–53. DOI: 10.1038/nphys1151 (cit. on p. 71).

[161] H. G. Leduc, B. Bumble, P. K. Day, B. H. Eom, J. Gao, S. Golwala, B. A. Mazin, S. McHugh, A. Merrill, D. C. Moore, O. Noroozian, A. D. Turner, and J. Zmuidzinas: *Titanium nitride films for ultrasensitive microresonator detectors*. Applied Physics Letters **97** (2010). DOI: 10.1063/1.3480420 (cit. on p. 71).

[162] L. Grünhaupt, N. Maleeva, S. T. Skacel, M. Calvo, F. Levy-Bertrand, A. V. Ustinov, H. Rotzinger, A. Monfardini, G. Catelani, and I. M. Pop: *Loss Mechanisms and Quasiparticle Dynamics in Superconducting Microwave Resonators Made of Thin-Film Granular Aluminum*. Physical Review Letters **121** (2018). DOI: 10.1103/physrevlett.121.117001 (cit. on p. 71).

[163] I. V. Pechenezhskiy, R. A. Mencia, L. B. Nguyen, Y.-H. Lin, and V. E. Manucharyan: *The superconducting quasicharge qubit*. Nature **585** (2020), 368–371. DOI: 10.1038/s41586-020-2687-9 (cit. on pp. 71, 72, 76).

[164] M. H. Devoret: "Quantum Fluctuations in Electrical Circuits". *Quantum Fluctuations*. Ed. by S. Reynaud, E. Giacobino, and J. Zinn-Justin. Les Houches Session LXIII. Amsterdam: Elsevier, 1997, pp. 351–386 (cit. on pp. 73, 74, 80).

[165] N. A. Masluk, I. M. Pop, A. Kamal, Z. K. Minev, and M. H. Devoret: *Supplemental Material for "Microwave characterization of Josephson junction arrays: implementing a low-loss superinductance"*. Yale University, Department of Applied Physics. 2012. URL: https://doi.org/10.1103/PhysRevLett.109.137002 (cit. on p. 75).

[166] T. Weißl, B. Küng, E. Dumur, A. K. Feofanov, I. Matei, C. Naud, O. Buisson, F. W. J. Hekking, and W. Guichard: *Kerr coefficients of plasma resonances in Josephson junction chains*. Physical Review B **92** (2015). DOI: 10.1103/physrevb.92.104508 (cit. on p. 75).

[167] C. Jünger, T. Chistolini, L. B. Nguyen, H. Kim, L. Chen, T. Ersevim, W. Livingston, G. Koolstra, D. I. Santiago, and I. Siddiqi: *Implementation of scalable suspended superinductors*. Applied Physics Letters **126** (2025). DOI: 10.1063/5.0250341 (cit. on p. 76).

[168] A. Inc.: *Ansys Maxwell*. Version 2023. 2023. URL: https://www.ansys.com/products/electronics/ansys-maxwell (cit. on pp. 79, 82).

[169] G. Burkard, R. H. Koch, and D. P. DiVincenzo: *Multilevel quantum description of decoherence in superconducting qubits*. Physical Review B **69** (2004). DOI: 10.1103/physrevb.69.064503 (cit. on p. 80).

[170] D. B. Haviland, K. Andersson, and P. Ågren: *Superconducting and Insulating Behavior in One-Dimensional Josephson Junction Arrays*. J. Low Temp. Phys. **118** (2000), 733–749. DOI: 10.1023/a:1004603814529 (cit. on p. 81).

[171] S. Ó Peatáin, T. Dixon, P. J. Meeson, J. M. Williams, S. Kafanov, and Y. A. Pashkin: *Simulating the effects of fabrication tolerance on the performance of Josephson travelling wave parametric amplifiers*. Supercond. Sci. Technol. **36** (2023), 045017. DOI: 10.1088/1361-6668/acba4e (cit. on p. 81).

[172] D. M. Basko and F. W. J. Hekking: *Disordered Josephson junction chains: Anderson localization of normal modes and impedance fluctuations*. Phys. Rev. B **88** (2013). DOI: 10.1103/physrevb.88.094507 (cit. on pp. 85, 92).

[173] D. V. Nguyen and D. M. Basko: *Inhomogeneous Josephson junction chains: a superconducting meta-material for superinductance optimization*. The European Physical Journal Special Topics **226** (2017), 1499–1514. DOI: 10.1140/epjst/e2016-60278-4 (cit. on pp. 85, 92).

[174] S. V. Lotkhov, E. M. Tolkacheva, D. V. Balashov, M. I. Khabipov, F.-I. Buchholz, and A. B. Zorin: *Low hysteretic behavior of Al/AlOx/Al Josephson junctions*. Appl. Phys. Lett. **89** (2006). DOI: 10.1063/1.2357915 (cit. on p. 92).

[175] S. Kono, J. Pan, M. Chegnizadeh, X. Wang, A. Youssefi, M. Scigliuzzo, and T. J. Kippenberg: *Mechanically induced correlated errors on superconducting qubits with relaxation times exceeding 0.4 ms*. Nature Communications **15** (2024). DOI: 10.1038/s41467-024-48230-3 (cit. on p. 99).

[176] P. Groszkowski and J. Koch: *Scqubits: a Python package for superconducting qubits*. Quantum **5** (2021), 583. DOI: 10.22331/q-2021-11-17-583 (cit. on p. 101).

[177] A. Kringhøj, L. Casparis, M. Hell, T. W. Larsen, F. Kuemmeth, M. Leijnse, K. Flensberg, P. Krogstrup, J. Nygård, K. D. Petersson, and C. M. Marcus: *Anharmonicity of a superconducting qubit with a few-mode Josephson junction*. Physical Review B **97** (2018). DOI: 10.1103/physrevb.97.060508 (cit. on p. 101).

[178] E. Hyyppä et al.: *Unimon qubit*. Nat. Commun. **13** (2022). DOI: 10.1038/s41467-022-34614-w (cit. on p. 107).

[179] A. Kreuzer, B. Liaw, D. Neubauer, H. Tohamy, T. Krumrey, H. Rotzinger, and A. V. Ustinov: "Persistent-current flux biasing of superconducting quarton qubits". 2026. in preparation (cit. on p. 107).

[180] *QDAC II: Multi-Channel Precision DC Source — Specification Sheet*. Quantum Machines. Tel Aviv, Israel, 2025. URL: https://www.quantum-machines.co/products/qdac/ (cit. on p. 108).

[181] J. B. Johnson: *Thermal Agitation of Electricity in Conductors*. Physical Review **32** (1928), 97–109. DOI: 10.1103/PhysRev.32.97 (cit. on p. 108).

[182] H. Nyquist: *Thermal Agitation of Electric Charge in Conductors*. Physical Review **32** (1928), 110–113. DOI: 10.1103/PhysRev.32.110 (cit. on p. 108).

[183] S. Kogan: *Electronic Noise and Fluctuations in Solids*. Cambridge University Press, 1996. DOI: 10.1017/cbo9780511551666 (cit. on p. 108).

[184] G. Scandurra, C. Ciofi, J. Smulko, and H. Wen: *A review of design approaches for the implementation of low-frequency noise measurement systems*. Review of Scientific Instruments **93** (2022). DOI: 10.1063/5.0116589 (cit. on p. 108).

[185] E. Milotti: *1/f noise: a pedagogical review*. 2002. DOI: 10.48550/ARXIV.PHYSICS/0204033 (cit. on p. 108).

[186] M. G. Castellano, F. Chiarello, G. Torrioli, and P. Carelli: *Static flux bias of a flux qubit using persistent current trapping*. Superconductor Science and Technology **19** (2006), 1158–1163. DOI: 10.1088/0953-2048/19/11/011 (cit. on pp. 108, 109).

[187] L. Longobardi, S. Pottorf, V. Patel, and J. Lukens: *Development and Testing of a Persistent Flux Bias for Qubits*. IEEE Transactions on Applied Superconductivity **17** (2007), 88–89. DOI: 10.1109/tasc.2007.897413 (cit. on pp. 108, 109).

[188] L. Rossi and L. Bottura: *Superconducting Magnets for Particle Accelerators*. Reviews of Accelerator Science and Technology **05** (2012), 51–89. DOI: 10.1142/s1793626812300034 (cit. on p. 109).

[189] C. Li, J. Geng, B. Shen, X. Li, J. Gawith, J. Ma, J. Yang, and T. A. Coombs: *Persistent Current Switch for HTS Superconducting Magnets: Design, Control Strategy, and Test Results*. IEEE Transactions on Applied Superconductivity **29** (2019), 1–4. DOI: 10.1109/tasc.2018.2889463 (cit. on p. 109).

[190] A. Burck, S. Kempf, S. Schäfer, H. Rotzinger, M. Rodrigues, T. Wolf, L. Gastaldo, A. Fleischmann, and C. Enss: *Microstructured Magnetic Calorimeter with Meander-Shaped Pickup Coil*. Journal of Low Temperature Physics **151** (2008), 337–344. DOI: 10.1007/s10909-007-9659-4 (cit. on p. 109).

[191] D. Bénâtre, M. Féchant, N. Zapata, N. Gosling, P. Paluch, T. Reisinger, and I. M. Pop: *Simultaneous sweet-spot locking of gradiometric fluxonium qubits*. Physical Review Applied **24** (2025). DOI: 10.1103/gjks-ctvm (cit. on p. 109).

[192] J. Clarke and A. I. Braginski, eds.: *The SQUID Handbook, Vol. I: Fundamentals and Technology of SQUIDs and SQUID Systems*. Weinheim: Wiley-VCH, 2004 (cit. on p. 111).

[193] A. Kreuzer, H. Tohamy, T. Krumrey, A. Ionita, J. Lisenfeld, H. Rotzinger, and A. V. Ustinov: "Stacked Josephson junctions for reduced TLS surface participation in qubits". 2026. in preparation (cit. on p. 116).

[194] J. S. Kline, H. Wang, S. Oh, J. M. Martinis, and D. P. Pappas: *Josephson phase qubit circuit for the evaluation of advanced tunnel barrier materials*. Superconductor Science and Technology **22** (2008), 015004. DOI: 10.1088/0953-2048/22/1/015004 (cit. on p. 119).

[195] J. Lisenfeld, C. Müller, J. H. Cole, P. Bushev, A. Lukashenko, A. Shnirman, and A. V. Ustinov: *Measuring the Temperature Dependence of Individual Two-Level Systems by Direct Coherent Control*. Physical Review Letters **105** (2010). DOI: 10.1103/physrevlett.105.230504 (cit. on p. 119).

[196] A. Bilmes, S. Volosheniuk, A. V. Ustinov, and J. Lisenfeld: *Probing defect densities at the edges and inside Josephson junctions of superconducting qubits*. npj Quantum Inf. **8** (2022). DOI: 10.1038/s41534-022-00532-4 (cit. on p. 119).

[197] A. Osman, J. Fernández-Pendás, C. Warren, S. Kosen, M. Scigliuzzo, A. Frisk Kockum, G. Tancredi, A. Fadavi Roudsari, and J. Bylander: *Mitigation of frequency collisions in superconducting quantum processors*. Phys. Rev. Research **5** (2023). DOI: 10.1103/physrevresearch.5.043001 (cit. on p. 119).

[198] J. Burnett, L. Faoro, I. Wisby, V. L. Gurtovoi, A. V. Chernykh, G. M. Mikhailov, V. A. Tulin, R. Shaikhaidarov, V. Antonov, P. J. Meeson, A. Y. Tzalenchuk, and T. Lindström: *Evidence for interacting two-level systems from the 1/f noise of a superconducting resonator*. Nature Communications **5** (2014). DOI: 10.1038/ncomms5119 (cit. on p. 119).

[199] R. Barends et al.: *Coherent Josephson Qubit Suitable for Scalable Quantum Integrated Circuits*. Phys. Rev. Lett. **111** (2013). DOI: 10.1103/physrevlett.111.080502 (cit. on p. 120).

List of Publications

[1] A. Kreuzer, T. Krumrey, H. Tohamy, A. Ionita, H. Rotzinger, and A. V. Ustinov: *Stacked Josephson junctions for quantum circuit applications*. Phys. Rev. Applied (2025). arXiv: 2503.11437 [cond-mat.supr-con]. accepted for publication; to appear.

[2] A. Kreuzer, H. Tohamy, T. Krumrey, A. Ionita, J. Lisenfeld, H. Rotzinger, and A. V. Ustinov: "Stacked Josephson junctions for reduced TLS surface participation in qubits". 2026. in preparation.

[3] A. Kreuzer, B. Liaw, D. Neubauer, H. Tohamy, T. Krumrey, H. Rotzinger, and A. V. Ustinov: "Persistent-current flux biasing of superconducting quarton qubits". 2026. in preparation.

Appendix

A Exact integration of the cumulative TLS-count model

Integrating Eq. (3.30) over coupling can be carried out in closed form. With the substitution $x = g/g_{\max}$ one obtains

$$\int \frac{\sqrt{1 - g^2/g_{\max}^2}}{2g}\,\mathrm{d}g \;=\; \frac{1}{2}\left[\sqrt{1-x^2} + \ln\!\left(\frac{x}{1+\sqrt{1-x^2}}\right)\right] + \text{const.} \tag{A.1}$$

Evaluating Eq. (A.1) between a lower cutoff g_{res} (set by the finite experimental resolution) and an upper counting threshold g_0 yields the cumulative number of splittings in a given energy window ΔE,

$$N_{\mathrm{TLS}}(g_{\mathrm{res}} \le g \le g_0; \Delta E) = \Delta E\,\sigma A\left[F\!\left(\frac{g_0}{g_{\max}}\right) - F\!\left(\frac{g_{\mathrm{res}}}{g_{\max}}\right)\right], \tag{A.2}$$

$$F(x) \equiv \frac{1}{2}\left[\sqrt{1-x^2} + \ln\!\left(\frac{x}{1+\sqrt{1-x^2}}\right)\right]. \tag{A.3}$$

In the experimentally relevant regime $g \ll g_{\max}$, where $g_{\max}$ is the maximal coupling strength set by the largest effective dipole moment and maximal field participation (see Eq. (3.24)), equivalently $x \ll 1$ and thus $\sqrt{1-x^2} \approx 1$, such that

$$F(x) \;\approx\; \frac{1}{2}\left[1 + \ln\!\left(\frac{x}{2}\right)\right], \tag{A.4}$$

so that constants cancel in the difference and the cumulative count reduces to the logarithmic form used in Eq. (3.32),

$$N_{\mathrm{TLS}}(g \le g_0; \Delta E) \;\approx\; \Delta E\,\sigma A\,\frac{1}{2}\ln\!\left(\frac{g_0}{g_{\mathrm{res}}}\right) \;=\; \Delta E\,\sigma A\,\frac{1}{2}\ln\!\left(\frac{S_0}{S_{\mathrm{res}}}\right), \qquad S = 2g. \tag{A.5}$$

B Decoherence versus inductance ratio γ/N

To complement the analysis in Sec. 6.4, this section shows the measured coherence times as a function of the inductive energy ratio $\gamma/N = E_L/E_J$ defined in Eq. 3.47 in Sec. 3.4.2, which parametrizes the balance between the Josephson energy of the small-junction and the inductive energy of the junction array. In particular, T_1 and the ratio $T_{2,\mathrm{Echo}}/T_1$ versus γ/N are plotted in Fig. B.1. Despite a small trend for larger $T_{2\,\mathrm{Echo}}$ close to $\gamma/N = 1$ for the small stack footprint data set, no clear trend of the data on γ/N is noted.

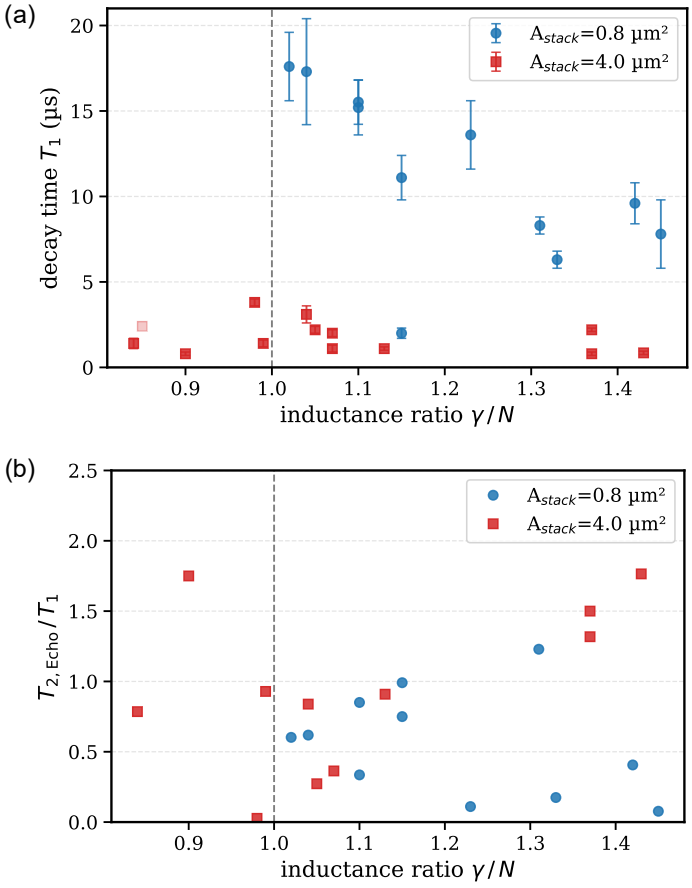

Figure B.1: Coherence times versus inductance ratio γ/N. (a) Relaxation time T_1 versus γ/N. (b) Spin-Echo time normalized by the relaxation time versus γ/N. Each marker represents one qubit device, with color and symbol distinguishing the stack footprint. The vertical dashed lines mark the ratio $\gamma/N = 1$.

Acknowledgements

I would like to express my deep gratitude to Prof. Dr. Alexey Ustinov for giving me the unique opportunity to pursue experimental research in physics. I am sincerely thankful for the exceptional trust he placed in my independent work and scientific judgment over many years. I especially appreciated the freedom and extensive resources he provided for my experimental activities.

This freedom shaped my doctoral research in a way that was particularly meaningful to me: rather than narrowing my focus to a single topic or technique, my PhD became a highly practice-oriented, technically broad, and exceptionally diverse experience. It ranged from theory work, calculations and design of experiments to modern nanofabrication methods, microwave engineering, measurement electronics, and cryogenic systems, as well as the analysis, interpretation, and presentation of experimental data. This breadth made each day of my doctoral work different and genuinely exciting. I am particularly grateful for the many opportunities to attend international conferences, which allowed me to become an active member of the scientific community.

I would like to thank Prof. Dr. Alexander Shnirman for taking the time to serve as the second examiner of this dissertation.

A very special and heartfelt thanks goes to Dr. Hannes Rotzinger, who has accompanied me as a mentor since my Master's thesis in this group. I am deeply grateful for the countless discussions, his continuous engagement, and his dedication, which made many of the experiences described above possible in the first place. I find it truly remarkable that, despite his many responsibilities and commitments, he always took the time to support and encourage me, and stood firmly behind my work.

I would also like to thank Dr. Jürgen Lisenfeld for his valuable discussions, constructive feedback, and insightful impulses, which provided important guidance throughout my doctoral research.

I am grateful to all colleagues in the group for their support over the years—whether through collaboration in the cleanroom and laboratory or through many stimu-

lating discussions (not only) about physics that enriched both my work and my understanding.

Finally, I would like to express my sincere thanks to Lucas Radtke, Dr. Aina Quintilla, and Dr. Silvia Diewald. Their help, expertise, and extraordinary dedication in the cleanroom were indispensable for carrying out the experiments and ultimately made this dissertation possible.

Karlsruhe, 06.02.2026 M. Sc. Alex S. Kreuzer